PU/NE-06-12

STEAM-AIR MIXTURE CONDENSATION IN A SUBCOOLED WATER POOL

FINAL REPORT

by

T. L. Norman, S. T. Revankar, M. Ishii, PU

and

J. M. Kelly, U.S. NRC

Prepared for
U.S. Nuclear Regulatory Commission

PURDUE

DECEMBER 2006

PURDUE UNIVERSITY
SCHOOL OF NUCLEAR ENGINEERING

PURDUE UNIVERSITY
SCHOOL OF NUCLEAR ENGINEERING

PU/NE-06-12

Steam-Air Mixture Condensation in a Subcooled Water Pool

FINAL REPORT

by

T. L. Norman, S. T. Revankar, M. Ishii, PU

and

J. M. Kelly, U.S. NRC

December 2006

Prepared for

U.S. Nuclear Regulatory Commission
Washington, DC 20555

Purdue University, School of Nuclear Engineering, 400 Central Drive
West Lafayette, IN 47907, USA

ACKNOWLEDGEMENTS

This research endeavor is a project of the Institute of Thermal Hydraulics at Purdue University. This was made possible through the financial support of the U. S. NRC (Nuclear Regulatory Commission) under contract number NRC-04-03-048 T.O. #5. We wish to express our sincerest thanks to Dr. J. Han of the U.S. NRC for all his support and interest throughout this project. Special thanks are extended to Dr. H. –S. Park of the Korea Atomic Energy Research Institute who assisted with some experiments and data analysis during his stay at Purdue University.

ABSTRACT

The overall goal of this research is to study the phenomena associated with jet-plume condensation of steam-noncondensable mixtures in a large subcooled pool of water. For this purpose a model suppression pool, scaled down 4.5 by height and 400 by volume, was designed and built to simulate a prototype reactor pool geometry. The design and test conditions were based on the hierarchical scaling principle that preserves the transfer of mass, momentum, energy and condensation phenomena. Distributed thermocouples within the pool provided a means to quantify the pool 3-D thermal response. 2-D temperature maps from interpolated thermocouple data measured at discrete points in the vertical plane were developed to describe the regions of the pool that were thermally stratified or mixed in the vertical plane.

The first series of experiments consisted of scoping and feasibility tests to quantify the pool capability and to test the range of conditions prescribed by the control volume and boundary flow scaling. Data reported include tests with horizontal venting of pure steam and steam-air mixtures through the top vent and venting of pure steam through the top two vents. A total of 8 tests were performed and 3 of them are discussed in detail and compared. The size of the vent pipe used for these tests was 2 inches in diameter. Two cases, named 1 and 2, are compared for similar steam injection fluxes of 37.2 and 34.6 g/s respectively. In case 1, a single horizontal vent is considered and in case 2 the vent-to-vent communication phenomenon is observed when top and middle vents are simultaneously opened. The pool initial temperatures were 20.4 and 24.3 °C respectively for cases 1 and 2. A third test, reported herein as case 6, shows the pool response when a steam and air mixture is discharged to the pool. In the remaining cases (3, 4, 5, 7, and 8) the pool was mixed and mild stratification was observed. Thermal stratification was observed in case 1 whereas it was not observed in cases 2 and 6. High frame-rate images of condensation acquired for 20 g/s and 50 g/s steam flow rate cases are compared where the behavior of an inertia-dominated jet-plume was observed for the 50 g/s case, whereas with less inertia (in the 20 g/s case) the buoyancy force was

predominant. These first series of tests captured the major phenomena associated with direct contact condensation in a subcooled pool with non-condensable gas.

In the second series of tests performed, a data base of pool thermal response for defined injection boundary conditions using steam and steam-air mixtures was acquired, assessed, and discussed for two injection vent sizes of 2-inch and 3-inch diameters. Using this database, regime maps that depict the transition from mixed to thermally stratified conditions were drawn in terms of the steam injection flux and the pool subcooling for the pure steam injection cases. This revealed a well defined boundary region where a thermally mixed pool is changed to a stratified pool. In the case of steam-air mixture injection, transitional behavior was also quantified in terms of the air mass fraction. The mixing to stratification boundary was distinguishable when plotted in terms of the steam flux versus air mass flow rate and pool temperature versus air mass flow rate. Flow visualization from high speed images were obtained and a pure steam mass flow rate case of 17.8 g/s was compared to a steam-air case with the same steam mass flow rate but with 0.5 % air mass fraction. The presence of air showed a definite change in the structure of the discharged effluent and its trajectory inside the pool. With air mass flow rates below 0.1 g/s and pool temperatures above 40 °C, the pool attained thermal stratification.

A toroidal cell around the effluent was observed in both the steam and steam-air mixture cases. However, in the pure steam case the toroidal cell consisted of vapor in the upper half with condensed and entrained liquid in the lower half. In the steam-air mixture case, the toroidal cell was more symmetric consisting of vapor with a liquid inner core. In the latter case the jet-plume path was projected upwards due to more buoyancy provided by air. The database accumulated here was used to assess the prediction capabilities of TRACE code which indicated that the code could not identify the thermal stratification criterion. A simplified model was then developed to predict the trajectory and spread of a two-phase jet-plume which was benchmarked against experimental results and CFD simulations using the drift-flux and two-fluid formulations with appropriate turbulence models. The simple model proved to be quite reasonable in predicting the jet-plume path and spread.

TABLE OF CONTENTS

ACKNOWLEDGEMENTS i

ABSTRACT ii

TABLE OF CONTENTS iv

LIST OF FIGURES vii

LIST OF TABLES xviii

NOMENCLATURE xx

1. INTRODUCTION 1-1

2. OBJECTIVES AND TECHNICAL APPROACH 2-1

2.1. Objectives and Milestones 2-1
2.2. Technical Approach 2-2
2.3. References 2-4

3. LITERATURE SURVEY 3-1

3.1. Introduction 3-1
3.2. Pool Stratification and Mixing 3-2
3.2.1. Approaches to Evaluating Stratification Characteristics in Systems 3-3
3.2.2. Gas Injection and Absorption in Liquid 3-5
3.3. Plume Characterization and Modeling 3-7
3.3.1. Vapor Plume and Jet Plume Characterization 3-7
3.3.2. Integral Plumes and Lumped-Parameter Models 3-12
3.3.3. Dimensionless Characterization of Buoyant Jets for Scaling .. 3-14
3.3.4. Mechanistic Approaches to Plume Modeling 3-18
3.4. Condensation Heat Transfer and Regime Maps 3-20
3.4.1. Steam Bubble Condensation with Non-Condensables in Subcooled Water 3-20
3.4.2. Flow Regime Classification with Condensation 3-22
3.4.3. Heat Transfer Correlations Developed for High Steam Mass Fluxes 3-27
3.5. Summary 3-30
3.6. References 3-36

4. EXPERIMENTAL FACILITY DESIGN AND TEST CONDITIONS 4-1

4.1. Scaling Philosophy 4-1

4.2. Design Basis 4-3
4.2.1. Prototype Containment 4-3
4.2.2. Scientific Design of a Scaled Suppression Pool for the ESBWR 4-4
4.3. Hardware Design 4-6
4.3.1. Pool Engineering Design 4-6
4.3.2. Piping for Routing Steam from PUMA RPV 4-7
4.4. Defining a Test Matrix 4-9
4.4.1. Preserving Pool Condensation Potential in Scaled Facility 4-9
4.4.2. Steam-Air Mixture Injection 4-11
4.4.3. Preserving Injection Fluxes in Scaled Facility 4-17
4.4.4. Preserving Time Scales of Phenomena 4-19
4.4.5. Separate-Effects Test Conditions 4-20
4.5. References 4-35

5. INSTRUMENTATION AND EXPERIMENTAL PROCEDURES 5-1

5.1. Instrumentation 5-1
5.2. Data Acquisition System 5-4
5.3. Test Procedures 5-6
5.4. References 5-10

6. FACILITY CHARACTERIZATION AND PRELIMINARY DATA 6-1

6.1. Pool Structural Heat Losses 6-1
6.2. Scoping and Feasibility Tests 6-2
6.2.1. Pure Steam Injection Cases 6-4
6.2.2. Steam-Air Mixture Injection Cases 6-7
6.2.3. Flow Visualization 6-7
6.3. Reference 6-29

7. EXPERIMENTAL RESULTS AND DISCUSSION 7-1

7.1. 2-Inch Vent Diameter Data 7-1
7.2. 3-Inch Vent Diameter Data 7-3
7.2.1. Pure Steam Injection 7-3
7.2.2. Steam-Air Mixture Injection 7-6
7.2.3. Double Venting of Steam and Steam-Air Mixtures 7-7
7.2.4. Regime Transition Maps 7-8
7.2.5. Flow Visualization 7-9
7.3. Thermal-Hydraulic Calculations at Vent Exit 7-10
7.4. References 7-96

8. TRACE CODE EVALUATION AND BENCHMARKING 8-1

8.1. TRACE Code Overview 8-1

8.2. Discretization of Governing Equations in TRACE 8-1
8.2.1. Conservation of Mass Equation 8-2
8.2.2. Conservation of Momentum Equation 8-4
8.2.3. Conservation of Energy Equation 8-4
8.2.4. Phase Change and Interfacial Jump Relations 8-5
8.2.5. TRACE Correlations and Heat-Transfer Coefficient Models .. 8-6
8.3. Input Deck for Scaled Suppression Pool 8-8
8.3.1. Pool Nodalization for the TRACE Code 8-9
8.4. TRACE Code Results 8-10
8.4.1. Thermal Stratification Case 8-11
8.4.2. Mixed Case 8-12
8.5. Sources of Errors in User Input 8-12
8.6. References 8-21

9. CFD SIMULATIONS OF A TWO-PHASE JET-PLUME 9-1

9.1. Introduction 9-1
9.2. Simulation Objectives 9-2
9.3. Mixture Model Equations 9-3
9.3.1. The k-ε mixture turbulence model 9-5
9.3.2. The Large Eddy Simulation Turbulence Model 9-6
9.4. The Two-Fluid Model 9-8
9.4.1. Turbulence Model for Each Phase 9-11
9.5. Tasks, Geometry and Mesh 9-12
9.6. Results and Discussion 9-13
9.6.1. Case 1 9-13
9.6.2. Case 2 9-14
9.6.3. Case 3 9-14
9.6.4. Case 4 9-15
9.7. References 9-22

10. A SIMPLIFIED TWO-PHASE JET-PLUME MODEL 10-1

10.1. Introduction 10-2
10.2. Underlying Assumptions 10-4
10.2.1. Bubble Rise Velocity 10-5
10.2.2. Entrainment of Ambient Fluid 10-7
10.2.3. Phase Change Kinetics 10-9
10.2.4. The Jet-Plume Trajectory and Spread 10-10
10.2.5. Factor of Momentum Amplification 10-11
10.3. Governing Equations of Horizontally Injected Axisymmetric Plume .. 10-12
10.3.1. Continuity Equation 10-12
10.3.2. Momentum Conservation Equations 10-14
10.3.3. Gas and Liquid Energy 10-15
10.4. Solution Method 10-15
10.5. Results and Discussion of Simplified Model 10-17

10.6. References 10-27

11. SUMMARY AND CLOSURE 11-1

APPENDIX A. THERMOCOUPLE COORDINATES AND TAG NAMES A-1

APPENDIX B. DETAILS OF HARDWARE AND INSTRUMENTATION B-1

APPENDIX C. VISUALIZATION TAKEN USING A DIGITAL CAMCORDER C-1

APPENDIX D. INPUT DECK FOR CONDITIONS IN T3-26 EXPERIMENTAL CASE D-1

APPENDIX E. STEAM-WATER THERMODYNAMIC PROPERTIES E-1

APPENDIX F. DEVELOPMENT OF MODEL EQUATIONS F-1

APPENDIX G. ARCHIVED DATA G-1

G.1. Guide to Finding Data and Test Conditions G-1
G.2. Master List of 3-inch Vent Diameter Test Data G-1
G.3. Master List of 2-inch Vent Diameter Test Data G-3

LIST OF FIGURES

Figure 1.1 Schematic showing RPV and SP components and piping in ESBWR containment 1-8

Figure 3.1 Steam condensation regime map for vertical orientation and atmospheric pressure conditions 3-35

Figure 4.1 ESBWR geometry of RPV and SP showing 1/10 th 'pie' shape 4-27

Figure 4.2 Horizontal vent module between the DW and the WW 4-28

Figure 4.3 Front, sides and back layouts of model pool with window numbering and respective photographs..... 4-29

Figure 4.4 Schematic of 1/10th SP model facility showing the levels at which thermocouples are placed 4-30

Figure 4.5 Vent and window arrangements of model pool resting on support base 4-31

Figure 4.6 Isometric drawing of steam, air and water lines routed from PUMA ... 4-32

Figure 4.7 Pressure, flow rate and NC mass fraction obtained from RELAP5 simulations of a BDLB scenario over 25 minute duration 4-33

Figure 4.8 Modified top vent for inserting orifice between flanges 4-34

Figure 5.1 Thermocouple cage frame showing a few wires suspended on the sliding bars 5-8

Figure 5.2 Thermocouple locations along pool center plane 5-9

Figure 6.1 Real-time temperature data at the water surface for Case 1 6-9

Figure 6.2 Vertical temperature distributions along the vent side centerlines for Case 1 6-10

Figure 6.3 Vertical temperature distributions along the pool side centerlines for Case 1 6-11

Figure 6.4 Temperature profile development along pool vertical center plane for Case 1 6-12

Figure 6.5 Temperature profile development along pool surface for Case 1 6-13

Figure 6.6 Real-time temperature data at the water surface for Case 2 6-14

Figure 6.7 Vertical temperature distributions along the vent side centerlines for Case 2 6-15

Figure 6.8 Vertical temperature distributions along the pool side centerlines for Case 2 6-16

Figure 6.9 Temperature profile development along the pool vertical center plane for Case 2 6-17

Figure 6.10 Temperature profile development along the pool surface for Case 2 ... 6-18

Figure 6.11 Real-time temperature data at the water surface for Case 6 6-19

Figure 6.12 Vertical temperature distributions along the vent side centerlines for Case 6 6-20

Figure 6.13 Vertical temperature distributions along the pool side centerlines for Case 6 6-21

Figure 6.14 Temperature profile development along the pool vertical center plane for Case 6 6-22

Figure 6.15 Temperature profile development along the pool surface for Case 6 ... 6-23

Figure 6.16 High speed photography sequences at the steam flow rate of 50 g/s with 125 fps and view port 12 (1) 6-24

Figure 6.17 High speed photography sequences at the steam flow rate of 50 g/s with 125 fps and view port 12 (2) 6-25

Figure 6.18 High speed photography sequences at the steam flow rate of 20 g/s with 60 fps and view port 8 6-26

Figure 6.19 High speed photography sequences at the steam flow rate of 50 g/s with 60 fps and view port 8 6-27

Figure 6.20 Vertical buoyant jet in cross-flow 6-28

Figure 7.1 Real-time temperature data at the water surface for case T2-18 7-16

Figure 7.2 Vertical temperature distribution along the vent side centerline for case T2-18 7-17

Figure 7.3 Vertical temperature distribution along the pool side centerline for

case T2-18 7-18

Figure 7.4 Temperature profile development along the pool vertical center plane for case T2-18 7-19

Figure 7.5 Temperature profile development along the pool surface for case T2-18 7-20

Figure 7.6 Real-time temperature data at the water surface for case T2-23 7-21

Figure 7.7 Vertical temperature distribution along the vent side centerline for case T2-23 7-22

Figure 7.8 Vertical temperature distribution along the pool side centerline for case T2-23 7-23

Figure 7.9 Temperature profile development along the pool vertical center plane for case T2-23 7-24

Figure 7.10 Temperature profile development along the pool surface for case T2-23 7-25

Figure 7.11 Real-time temperature data at the water surface for case T3-23 7-26

Figure 7.12 Vertical temperature distribution along the vent side centerline for case T3-23 7-27

Figure 7.13 Vertical temperature distribution along the pool side centerline for case T3-23 7-28

Figure 7.14 Temperature profile development along the pool vertical center plane for case T3-23 7-29

Figure 7.15 Temperature profile development along the pool surface for case T3-23 7-30

Figure 7.16 Real-time temperature data at the water surface for case T3-24 7-31

Figure 7.17 Vertical temperature distribution along the vent side centerline for case T3-24 7-32

Figure 7.18 Vertical temperature distribution along the pool side centerline for case T3-24 7-33

Figure 7.19 Temperature profile development along the pool vertical center plane for case T3-24 7-34

Figure 7.20 Temperature profile development along the pool surface for case T3-24 7-35

Figure 7.21 Real-time temperature data at the water surface for case T3-42 7-36

Figure 7.22 Vertical temperature distribution along the vent side centerline for case T3-42 7-37

Figure 7.23 Vertical temperature distribution along the pool side centerline for case T3-42 7-38

Figure 7.24 Temperature profile development along the pool vertical center plane for case T3-42 7-39

Figure 7.25 Temperature profile development along the pool surface for case T3-42 7-40

Figure 7.26 Real-time temperature data at the water surface for case T3-27 7-41

Figure 7.27 Vertical temperature distribution along the vent side centerline for case T3-27 7-42

Figure 7.28 Vertical temperature distribution along the pool side centerline for case T3-27 7-43

Figure 7.29 Temperature profile development along the pool vertical center plane for case T3-27 7-44

Figure 7.30 Temperature profile development along the pool surface for case T3-27 7-45

Figure 7.31 Real-time temperature data at the water surface for case T3-43 7-46

Figure 7.32 Vertical temperature distribution along the vent side centerline for case T3-43 7-47

Figure 7.33 Vertical temperature distribution along the pool side centerline for case T3-43 7-48

Figure 7.34 Temperature profile development along the pool vertical center plane for case T3-43 7-49

Figure 7.35 Temperature profile development along the pool surface for case T3-43 7-50

Figure 7.36 Real-time temperature data at the water surface for case T3-47 7-51

Figure 7.37 Vertical temperature distribution along the vent side centerline for case T3-47 7-52

Figure 7.38 Vertical temperature distribution along the pool side centerline for case T3-47 7-53

Figure 7.39 Temperature profile development along the pool vertical center plane for case T3-47 7-54

Figure 7.40 Temperature profile development along the pool surface for case T3-47 7-55

Figure 7.41 Real-time temperature data at the water surface for case T3-50 7-56

Figure 7.42 Vertical temperature distribution along the vent side centerline for case T3-50 7-57

Figure 7.43 Vertical temperature distribution along the pool side centerline for case T3-50 7-58

Figure 7.44 Temperature profile development along the pool vertical center plane for case T3-50 7-59

Figure 7.45 Temperature profile development along the pool surface for case T3-50 7-60

Figure 7.46 Real-time temperature data at the water surface for case T3-30 7-61

Figure 7.47 Vertical temperature distribution along the vent side centerline for case T3-30 3-62

Figure 7.48 Vertical temperature distribution along the pool side centerline for case T3-30 7-63

Figure 7.49 Temperature profile development along the pool vertical center plane for case T3-30 7-64

Figure 7.50 Temperature profile development along the pool surface for case T3-30 7-65

Figure 7.51 Real-time temperature data at the water surface for case T3-51 7-66

Figure 7.52 Vertical temperature distribution along the vent side centerline for case T3-51 7-67

Figure 7.53 Vertical temperature distribution along the pool side centerline for case T3-51 7-68

Figure 7.54 Temperature profile development along the pool vertical center plane for case T3-51 7-69

Figure 7.55 Temperature profile development along the pool surface for case T3-51 7-70

Figure 7.56 Real-time temperature data at the water surface for case T3-26 7-71

Figure 7.57 Vertical temperature distribution along the vent side centerline for case T3-26 7-72

Figure 7.58 Vertical temperature distribution along the pool side centerline for case T3-26 7-73

Figure 7.59 Temperature profile development along the pool vertical center plane for case T3-26 7-74

Figure 7.60 Temperature profile development along the pool surface for case T3-26 7-75

Figure 7.61 Real-time temperature data at the water surface for case T3-38 7-76

Figure 7.62 Vertical temperature distribution along the vent side centerline for case T3-38 7-77

Figure 7.63 Vertical temperature distribution along the pool side centerline for case T3-38 7-78

Figure 7.64 Temperature profile development along the pool vertical center plane for case T3-38 7-79

Figure 7.65 Temperature profile development along the pool surface for case T3-38 7-80

Figure 7.66 Real-time temperature data at the water surface for case T3-53 7-81

Figure 7.67 Vertical temperature distribution along the vent side centerline for case T3-53 7-82

Figure 7.68 Vertical temperature distribution along the pool side centerline for case T3-53 7-83

Figure 7.69 Temperature profile development along the pool vertical center plane for case T3-53 7-84

Figure 7.70 Temperature profile development along the pool surface for case T3-53 7-85

Figure 7.71 Real-time temperature data at the water surface for case T3-55 7-86

Figure 7.72 Vertical temperature distribution along the vent side centerline for case T3-55 7-87

Figure 7.73 Vertical temperature distribution along the pool side centerline for case T3-55 7-88

Figure 7.74 Temperature profile development along the pool vertical center plane for case T3-55 7-89

Figure 7.75 Temperature profile development along the pool surface for case T3-55 7-90

Figure 7.76 The transition from the mixed to stratified conditions for pure steam injection cases (a) steam mass flux versus inlet pool temperature (b) Subcooling versus Froude number 7-91

Figure 7.77 The transition from the mixed to stratified conditions for steam-air injection cases (steam mass flux versus air mass flow rate) 7-92

Figure 7.78 The transition from the mixed to stratified conditions for steam-air injection cases (pool water temperature versus air mass flow rate) 7-93

Figure 7.79 Venting images of steam mass flow rate of 17.8 g/s with no air. 0.033 seconds between frames 7-94

Figure 7.80 Steam mass flow rate is 17.8 g/s with 0.5 % air. 0.033 seconds between frames 7-95

Figure 8.1 Nodalization schematic using the vessel component in TRACE 8-13

Figure 8.2 A representative mesh cell for TRACE 8-14

Figure 8.3 Azimuthal and radial cell numbering used for the vessel component in modeling the pool in TRACE 8-15

Figure 8.4 Axial cell numbering of levels, L1 to L11 8-16

Figure 8.5 Experimental case T3-26 compared to code prediction at ring 2 8-17

Figure 8.6 Experimental case T3-26 compared to code prediction at ring 5 8-18

Figure 8.7 Experimental case T3-30 compared to code prediction at ring 2 8-19

Figure 8.8 Experimental case T3-30 compared to code prediction at ring 5 8-20

Figure 9.1 CFD Fluent results of Case 1 9-16

Figure 9.2 CFD Fluent results of Case 2 9-17

Figure 9.3 Comparison of x and z velocities at z = 0.81915 m along horizontal for Fluent cases 1 and 2 9-18

Figure 9.4 Case 3; comparison of mixture model solution using LES with available data (top view) 9-19

Figure 9.5 Case 3, comparison of mixture model solution using LES with available data (vertical center-plane) 9-20

Figure 9.6 Case 4, comparison of mixture model solution with LES and interphase mass transfer with available data 9-21

Figure 10.1 Schematic of horizontally injected jet-plume showing velocity and void profiles along the s-axis defined by angle theta 10-18

Figure 10.2 Bubble sphericity described through dimensionless numbers 10-19

Figure 10.3 Functional relationship for entrainment in terms of local Froude number proposed by Milgram (1983) 10-20

Figure 10.4 Functional relationship for momentum amplification factor and phase distribution parameter proposed by Milgram (1983) 10-21

Figure 10.5 Model results of plume path and temperature along the path in comparison to the temperature profile in the vertical center plane for case T3-23 10-22

Figure 10.6 Model results of plume width along the plume path for case T3-23 10-23

Figure 10.7 Model results of plume velocity along the path, for case T3-23 10-23

Figure 10.8 Comparison of model results of the plume path with the experimental results of the temperature profile development along the pool vertical center plane for case T3-43 at time 1000 sec 10-24

Figure 10.9 Model results of plume temperature along the plume path for case T3-43 10-25

Figure 10.10 Model results of plume velocity along the path for case T3-43 10-25

Figure 10.11 Temperature profile development along the pool vertical center plane for case T3-23 at time 800 seconds (refer to Figures 9.4 and 9.5) 10-26

Figure B.1 Arrangement of air supply lines and preheater B-1

Figure B.2 Details of viewing ports B-2

Figure B.3 Details of steam line with vortex flow meter B-3

Figure B.4 Details of steam and air lines B-4

Figure B.5 Details of steam/air line in x-y plane connecting to water line from CRL line from PUMA B-5

Figure B.6 Injection assembly for 2-inch and 3-inch cases B-6

Figure B.7 Thermocouples shown on the instrumentation cage at elevation 16.9 cm (1st vent from bottom) B-7

Figure B.8 Thermocouples shown on the instrumentation cage at elevation 47.3 cm (2nd vent from bottom) B-8

Figure B.9 Thermocouples shown on the instrumentation cage at elevation 77.7 cm (3rd vent from bottom) B-9

Figure B.10 Thermocouples shown on the instrumentation cage at elevation 100.4 cm (4th vent from bottom) B-10

Figure B.11 Thermocouples shown on the instrumentation cage at elevation 121.1 cm (initial water level) B-11

Figure B.12 Thermocouples shown on the instrumentation cage at elevation 128.43 cm B-12

Figure B.13 Thermocouple locations along pool center plane B-13

Figure C.1 Steam flow rate is 5g/s and pool initial temperature is 53 °C. Titanium tracer particles follow the bulk liquid motion. Taken at window 12 .... C-1

Figure C.2 Steam flow rate is 10 g/s and air flow rate is 0.1 g/s. Taken at window 8 with camcorder pointing downward to the vent C-2

Figure C.3 Another sequence with steam flow rate at 10 g/s and air flow rate at 0.1 g/s. Taken at window 8 with camcorder pointing downward to the vent C-3

Figure C.4 Camcorder images of pure air being injected. A mushroom type structure is observed C-4

LIST OF TABLES

Table 3.1 Condensation regimes of steam-air injection into subcooled water ... 3-32

Table 3.2 Experimental parameters and phenomena considered by various researchers ... 3-33

Table 3.3 Comparison of models and empirical correlations proposed by various researchers ... 3-34

Table 4.1 Scaled suppression pool dimensions ... 4-5

Table 4.2 K-loss in steam-air piping system from mixing tee to vent exit ... 4-8

Table 4.3 Terms defined in equations 4.30a and 4.30b ... 4-14

Table 4.4 Water conduction, liquid conduction and binary diffusion at atmospheric conditions ... 4-15

Table 4.5 Prototypic conditions determined from RELAP5 simulation of SBWR-600 ... 4-22

Table 4.6 Mass flow rate scaled conditions ... 4-22

Table 4.7 Volumetric flow rate scaled conditions ... 4-22

Table 4.8 Calculation of model pool temperature based on temperature difference ... 4-23

Table 4.9 Calculation of model pool temperature based on subcooling number 4-23

Table 4.10 Test matrix and experimental conditions for 2 inch vent pipe injection ... 4-24

Table 4.11 Test matrix and experimental conditions for 3 inch vent pipe injection ... 4-25

Table 5.1 Range of vortex flow meter ... 5-2

Table 5.2 Air mass flow controllers ... 5-2

Table 5.3 Instrumentation ... 5-3

Table 5.4 Parameters measured and phenomena of interest ... 5-3

Table 6.1 Parameters used for calculating pool heat loss 6-1

Table 6.2 Summary of pure steam and steam-air mixture scoping tests 6-3

Table 7.1 Summary of SP tests using 2 inch injection pipe 7-12

Table 7.2 Summary of SP tests using 3 inch injection pipe 7-13

Table 8.1 Test conditions for cases T3-26 and T3-30 that are used for comparing with code prediction 8-11

Table 9.1 Coordinates of the nodes used for corners of pool geometry 9-15

Table 9.2 Fluid properties used for cases 4 and 5 9-15

Table 9.3 Wall properties 9-15

NOMENCLATURE

Roman:

a	[m^2]	Cross sectional area
a_i	[m^2]	Interfacial area between liquid and gas phases
A	[-]	Submergence aspect ratio
A	[m^2]	Area
b	[m]	Plume radius
Bo	[-]	Bond number
c	[m/s]	Speed of sound
c	[-]	Shear coefficient
C_D	[-]	Drag coefficient
c_i	[-]	Interfacial drag coefficient
c_p	[$Jkg^{-1}C^{-1}$]	Isobaric specific heat
c_v	[$Jkg^{-1}C^{-1}$]	Isochoric specific heat
d	[m]	Bubble diameter
D	[m]	Diameter
D_b	[m^2]	Bubble interfacial area
D_{sa}	[m^2/s]	Binary mass diffusion coefficient of steam through a medium of air
D_J	[m]	Jet diameter
e	[m^2/s^2]	Specific internal energy
e	[m]	Roughness parameter
E	[-]	Entrainment coefficient
E	[-]	Enclosure aspect ratio
E_g	[W] or [J/s]	Vapor latent heat energy
Eo	[-]	Eötvös number
f	[-]	Drag function
f	[-]	Friction factor
Fr	[-]	Froude number
g	[ms^{-2}]	Gravitational acceleration
G		Filter function

G	[kg/m^{2}s]	Mass flux
h	[Wm^{-2}C^{-1}]	Heat transfer coefficient {or W/m^{2}K}
h_k	[J/mol]	Sensible enthalpy for phase k.
h_{sg}	[kJ/kg]	Gas saturation enthalpy
h_{wg}	[Wm^{-2}C^{-1}]	Effective wall heat transfer coefficient to gas
h_{wf}	[Wm^{-2}C^{-1}]	Effective wall heat transfer coefficient to liquid
h'_f	[kJ/kg]	Liquid enthalpy of the bulk liquid if the liquid is vaporizing or the liquid saturation enthalpy if vapor is condensing
h'_v	[kJ/kg]	Vapor enthalpy of the bulk vapor if the vapor is condensing or the vapor saturation enthalpy if liquid is vaporizing
H	[-]	Nondimensional jet submergence
Ja	[-]	Jacob (or Jakob) number, $\rho_f c_p \Delta T/\rho_s h_{fg}$
k	[m^2/s^3]	Turbulent kinetic energy
k	[Wm^{-1}C^{-1}]	Thermal conductivity
k_d^a	[W/(m.K)]	Diffusion-equilibrium thermal conductivity of air
k_w	[W/(m.K)]	Water conductivity
l, L	[m]	Length, axial cell level numbering
Le	[-]	Lewis number
L_o	[m]	Laplace coefficient
Mo	[-]	Morton number
$\dot{m}_{in}$	[kg/m^{2}s]	Inlet mass flux
M	[kg]	Mass
M	[kg/s]	Mass flow rate
M	[kg/kmol]	Molar mass
n	[-]	Numerical quantity
N_{pch}	[-]	Phase change number
N_{sub}	[-]	Subcooling number
N_μ	[-]	Viscosity number
Nu	[-]	Nusselt number
p, P	[Pa]	Pressure

P	[-]	Pool aspect ratio
Pr	[-]	Liquid Prandtl number, $\mu c_p / \kappa$ (kinematic viscosity / thermal diffusivity)
q	[W] or [J/s]	Power
q	[W/m^3]	Heat-transfer rate per unit volume
q_{gf}	[W/m^3]	Liquid-to-gas sensible heat transfer
Q	[m^3/s]	Volumetric flow rate
$\dot{Q}_c$	[W] or [J/s]	Condensation power
R	[-]	Ratio of prototype to model quantity
R	[J/(kgK)]	Ideal gas constant {or units [J/(kmol.K)]}
Ra	[-]	Raleigh number
Re	[-]	Reynolds number
Re_f^s	[-]	Steam-liquid Reynolds number, $v_s D_j / \nu_f$ (inertial / viscous)
Ri	[-]	Richardson number
s	[m]	Plume path s-axis
S_E	[J/m^{3}s]	Volumetric heat source
S_{ij}	[s^{-1}]	Rate of strain tensor
t	[^{o}]	Azimuth or theta angle, azimuthal angular divisions
t	[s]	Time
t	[m]	Thickness
T	[^{o}C]	Temperature
u, $\vec{v}$	[m/s]	Velocity
V	[m^3]	Volume or computational cell volume
$\dot{V}$	[m^3/s]	Volumetric flow rate
We	[-]	Weber number
x	[-]	Non-condensable mass fraction

Greek:

α	[-]	Void fraction or Entrainment coefficient

α	[C^{-1}]	Thermal coefficient of expansion
α'	[M^{-1}]	Analogous solvent coefficient of expansion
α_w	[m^2/s]	Water conduction $k_w/\rho_w c_p$
χ		Phase indicator function
Δ		Incremental change
ε	[m^2/s^3]	Dissipation rate of energy
ϕ	[^{o}]	Plume azimuth angular coordinate
$\bar{\phi}$		Filtered variable
γ	[-]	Momentum-amplification factor
Γ	[kg/m^3s]	Interphase mass transfer rate
κ		von Kármán constant
κ	[m^2/s]	Thermal diffusivity
κ'	[m^2/s]	Solute diffusivity
λ	[-]	Spread ratio
$\lambda_{R\text{-}T}$	[m]	Rayleigh-Taylor instability wavelength
μ	[kg/ms]	Dynamic viscosity
μ_t	[kg/ms]	Sub-grid scale turbulent viscosity
ν	[m^2/s]	Kinematic viscosity
Π	[-]	Time ratio
θ	[^{o}]	Plume path angle w. r. t. horizontal
ρ	[kg/m^3]	Density
σ_g	[N/m]	Interfacial tension
τ	[-]	Dimensionless time or relaxation time
τ_{ij}	[s^{-1}]	Subgrid-scale stresses

Special symbols:

[ ]	Square matrix (3 X 3) of coefficients or 3 X 1 matrix
∇	Differential operator $\frac{\partial}{\partial x}+\frac{\partial}{\partial y}+\frac{\partial}{\partial z}$
∞	Ambient quantity

Subscripts:

a	Air
b or g	Bubble local condition
cond	Condensation
d	Diffusion-equilibrium
d	Generic for r,θ, or z or for i, j, or k
dr	Drift
eff	Effective
evap	Evaporation
g, s	Gas, steam or gas mixture
f, w	Liquid
i	Interfacial
in	Inlet
j, J	Jet
Je	Jet energy transport frequency
Jt	Jet residence time
k	Gas or liquid phase, or k-losses
lift	Bubble lift
liq	Liquid
m	Centerline or maximum
m	Mixture
m	Quantity related to model
o	Initial or quantity at specified origin
p	Quantity related to prototype
p	Secondary phase
q	Primary phase
R	Ratio of model to prototype
s	Slip or terminal
sat	Saturation
se	Entrainment time of surrounding fluid

st	Transport time of surrounding fluid
sub	Subcooled
v	Water vapor
vm	Virtual mass
w	Wall
ww	Wetwell or suppression pool

Superscript:

T	Turbulent component
D	Molecular diffusion component

Abbreviations:

BCO	Bubbling Condensation Oscillation
BDLB	Bottom Drain Line Break
CFD	Computational Fluid Dynamics
CO	Condensation oscillation
CJC	Cold junction compensation
1-D	One-Dimensional
2-D	Two-Dimensional
3-D	Three-Dimensional
DAS	Data Acquisition System
DCC	Direct Contact Condensation
DP	Differential Pressure
DW	Drywell
EL	Elevation
fps	Frames per second
GDCS	Gravity Driven Cooling System
HD	Hydraulic Diameter
horiz	Horizontal
ICO	Interfacial Condensation Oscillation
imp	Jet impingement

lat	Latent heat
LDA	Laser Doppler Anemometer
LES	Large Eddy Simulation
LOCA	Loss Of Coolant Accident
MSLA	Main Steam Line A
MSLB	Main Steam Line Break
NC	Non-Condensable
ODE	Ordinary Differential Equation
pch	Phase Change
sub	Subcooling
PCCS	Passive Containment Cooling System
PSS	Pressure Suppression System
PUMA	Purdue University Multi-dimensional integral test Assembly
RPV	Reactor Pressure Vessel
SBWR	Simplified Boiling Water Reactor
SC	Stable Condensation
sen	Sensible heat
SETS	Stability Enhancing Two-Step
SIMPLE	Semi-Implicit Method for Pressure-Linked Equations
SP	Suppression Pool
SRV	Safety Relief Valve
TC	Thermocouple
TC	Transition from Chugging to bubbling oscillation
TS	Thermal Stratification
vert	Vertical
vol	Hydrodynamic cell volume
WW	Wetwell or suppression pool

1. INTRODUCTION

Specific to ALWR (Advanced Light Water Reactor) safety systems, there can be various modes of condensation depending on the configuration of the participating fluids and their thermal-hydraulic conditions. Classical condensation heat transfer problems involve either film-wise or drop-wise condensation with an intervening wall separating the vapor from the coolant. In reactor safety-related systems, the primary mode of heat transfer within the containment is DCC (Direct Contact Condensation) where the participating fluids share a common interface in the absence of an intervening wall and the condensation phase change process occurs at the fluid interface. The direct contact mode of condensation encountered during postulated accident scenarios include (Delhaye et al, 1981):

1. Condensation of vapor bubbles in liquid (steam-water mixing during emergency core cooling (ECC))
2. Condensation of vapor jets in liquid (steam-water mixing in the containment)
3. Condensation of vapor on subcooled droplets (ECC top-spray)
4. Condensation between two streams (more or less parallel, in the downcomer)

The range of thermal-hydraulic conditions in such scenarios can vary, with pressures ranging from 0.1 to 7 MPa, coolant temperatures from 40°C to saturated, and vapor temperatures from saturated to superheated.

The direct contact mode of heat transfer, in which there is a common evolving interface between the subcooled water and vapor, offers a greater surface area for phase change and heat transfer with the possibility of higher heat removal rates. The phenomena related to DCC in pressure suppression systems and the associated pool thermal stratification can be difficult to model since complex flow phenomena including steam jet penetration, disintegration to bubbling regimes, turbulent mixing, natural circulation and unsteady behavior are involved. It is therefore desirable to have detailed

experimental data and mechanistic models that can resolve the spatial interactions of two-phase mixtures and the individual physical processes involved. However, when this is not possible due to modeling difficulty and computational problems, thermal-hydraulic computer codes that rely on the predictive capability of such models are instead equipped with correlations that are used to obtain the best estimate of the expected behavior of nuclear power plants within acceptable uncertainty.

Safety features that are implemented in the design of a BWR include a pressure suppression system designed to maintain containment pressure within certain bounds of acceptability in the event of an accident (Pitts, 1980). The primary design criteria for a BWR containment building is for it to act as the final barrier against any accidental release of radioactive decay products out into the atmosphere. During the design basis accidents, a large amount of steam is discharged into the containment. This steam is then blown into the suppression pool through the vertical vent pipes and horizontal vent openings. The stability of the steam jet plume, its mixing and condensing characteristics and water entrainment into the plume determine the degree of thermal stratification within the pool (Gamble et al, 2001).

Thermal stratification in a suppression pool has been identified as a determining factor for the pool surface temperature and, as a result, the steam partial pressure inside the suppression pool cover gas of the SBWR (Simplified Boiling Water Reactor). In addition to the 4 points stated earlier regarding DCC in reactor safety, and specific to the recent passively safe boiling water reactor design by General Electric (GE), called ESBWR, the PCCS (Passive Containment Cooling System) venting of non-condensables to the suppression pool at low submergence as well as drywell to suppression pool venting constitute not only a scenario for the DCC mode but also provide a situation in which the pool surface temperature is heavily influenced by these venting processes.

The passive safety system of the SBWR and ESBWR designs for decay heat removal utilizes the large heat sink of the suppression pool (SP) wetwell by the direct contact condensation of steam inside the pool volume. The steam flow into the SP

venting system is driven by the over-pressure of the drywell in relation to the SP cover gas pressure and hydrostatic head above the SP horizontal vents. This total vapor flux and the SP water temperature affect the behavior of the condensing steam from the beginning to the end of the blowdown and the long term heat removal performance of the PCCS through the containment pressure. A shallow submergence of the steam-gas injection, such as horizontal steam injection to the suppression pool wetwell, can cause a situation where the steam energy is deposited in the upper regions of the SP pool volume above the injected point due to the large buoyancy force of the steam and non-condensable gas mixture. This then gives rise to a thermally stratified case that results in the lower volume of the pool below the source remaining thermally inactive.

The study by Gamble et al. (2001) on the long-term post-accident containment pressure in a passive boiling water reactor identified the surface temperature of the suppression pool as an important factor in determining the overall long-term containment pressure. The suppression pool (SP) condensation and thermal stratification are important phenomena during the short range as well as in the long transient phase of ESBWR accident. The SP gas space pressure is controlled by the temperature of the top layer of the water in the SP and that in turn governs the SBWR containment pressure. The pool surface temperature (T_i) determines the partial pressure of steam (P_{sat}) in the SP cover gas. The SP total cover gas pressure is given by $P_{total} = P_{NC} + P_{sat.}$, where P_{NC} is the partial pressure of non-condensable gas. The drywell pressure is higher than the SP cover gas pressure by an amount equal to the hydrostatic head due to top vent submergence depth in the SP water (refer to Figure 1.1). The partial pressure of the uncondensed steam in the suppression pool gas space increases as the pool surface temperature increases, where the former parameter is dictated by the latter. Therefore the steam partial pressure is a key parameter in determining the containment pressure. The pool thermal response affects the pool surface temperature, which is dictated by the dominant flow regime of the condensing steam inside the pool interior. Therefore the SP water surface temperature in addition to the non-condensable gas determines the containment pressure. The containment pressure is one of the most important quantities from the safety point of view since containment integrity depends on it.

The condensation and stratification processes in the SP water depend on the existence and motion of non-condensable gas mixed with the steam that is vented into the SP water. In the case of pure steam, the steam bubble or jet plume collapses instantaneously after it is vented and the water around the vent area is heated and rises to the surface. This may induce flow circulation in the suppression pool water. However, if the steam is mixed with non-condensable gas, the condensation of steam is inhibited in some way by the non-condensable gas allowing some of the steam to escape into the SP gas space. The non-condensable gas is then also free to rise to the water surface. This may induce a relatively large circulation in the suppression pool. The flow is three-dimensional and a 1-D model is not sufficient to model the suppression pool stratification degradation and mixing in such cases.

Best estimate thermal-hydraulic codes such as TRACE (TRAC/RELAP Advanced Computational Engine) are used to calculate the expected behavior of nuclear power plants for a broad range of normal operating conditions and accidental scenarios. These existing system codes such as RELAP5 and TRACE cannot predict the degree of stratification with 1-D modeling. This may impede the accurate prediction of the DW pressure, therefore there can be large uncertainties associated with the prediction of the containment pressure. The codes rely on numerous models and correlations to predict a wide range of reactor physical phenomena. Many of these models are not based on first principles and are either empirical or semi-empirical correlations developed from basic or separate-effects tests data. Some of the code models do not represent the physical situation and hence the model predictions for local phenomena are very poor. Recently, Kelly (1996) and Grandt (1997) have discussed in detail the thermal-hydraulic modeling needs for passive reactors and various problems encountered by using the current codes. Kelly (1997) and Ishii (1996) have presented important views on the future of thermal-hydraulic modeling. Separate-effects and integral-effects tests have been recommended for the developmental assessment of thermal-hydraulic models and constitutive relations.

Developmental assessment of reactor safety thermal-hydraulic codes such as RELAP5 and TRACE is carried out primarily by two methods. One approach is by separate-effects testing, where the models incorporated in the code are assessed by benchmarking them with experimental data for well defined geometries and boundary conditions. The other way is by integral-effects testing, where the code's simulation capability is assessed to ensure that a broad range of normal operating conditions and complicated accident scenarios can be replicated in scaled integral test facilities (Ishii et al 1996) to predict a wide range of reactor physical phenomena with reasonable certainty. Kelly (1997) has proposed that constitutive relations be component specific since geometries and thermal and hydrodynamic flow regimes in reactor systems can be complex. Therefore, empirical and semi-empirical correlations and interaction terms, based on traditional flow regime maps which were developed from separate-effects data would be improved to include source/sink terms that represent interfacial interactions.

There are 3 main flow configurations of DCC in transient or accident conditions as described earlier. These are: (1) vapor injection into liquid, (2) liquid injection into vapor, and (3) co-current flow of condensing vapor on stratified liquid flow. The current focus is on the first case, which is applicable to drywell to suppression pool venting in the reactor containment. The system codes mentioned such as TRACE and RELAP5 incorporate flow regime maps and correlations based on data obtained from adiabatic experiments, and so uncertainties have to be dealt with when applying the code to DCC where there exists a complex system of heat transfer processes. Hence for certain physical situations like those of DCC in pool geometries, the code's predictions can be very poor, which is quite an undesirable thing where reactor safety is concerned. For this reason, DCC and pool thermal stratification are identified as highly ranked phenomena for determining the suitability of models to address these phenomena. Various PIRT (Phenomena Identification and Ranking Table) analyses such as BWR-5 ATWS PIRT (Wulff, et al., 1994), B&W SBLOCA PIRT (Ortiz & Ghan 1992), AP600 SBLOCA PIRT (Wilson, et al. 1997), and SBWR LB-LOCA PIRT (Rohatgi, et al., 1995) have identified pool thermal stratification and direct contact condensation as highly ranked

phenomena. There are no adequate models in the thermal-hydraulic codes to address direct contact condensation and thermal stratification.

In recent years the major thermal-hydraulic issues have been focused mainly on the passive safety features of the ALWRs. The reason for this is that, at low pressure and low flow conditions, typical of accident conditions for ALWRs, (e.g. ESBWR) the prediction of two-phase flow transients is much more difficult than at relatively higher pressure or at higher flow. Use of TRACE for NRC design certification efforts presents a challenge because:

- NRC design certification has never been done before with TRACE code.
- TRACE has not yet been assessed and verified to its full extent for any reactor design.
- TRACE requires extensive code testing and model development.
- TRACE requires more careful evaluation, which takes longer and extensive effort for the first application to advanced reactors such as AP1000 and ESBWR.

The remainder of this report is divided into the following sections:

- Objectives, milestones and technical approach are provided.
- Literature survey: The key phenomena involved and the need for the data base are discussed. Problems in modeling pool mixing and stratification phenomena to be used with codes are also discussed.
- The scaling philosophy for designing an experimental facility and loop based on the ESBWR suppression pool prototype are discussed.
- Experimental approach and instrumentation: The choice of experimental conditions, measurement variables and justification for the range of parameters are discussed.
- Facility characterization and preliminary results from scoping and feasibility tests.
- Test results and boundary maps.

- CFD Simulations of shallow submerged air and steam jet-plumes injected horizontally into a trapezoidal water pool.
- A simplified model and analysis of a two-phase jet-plume injected horizontally into an initially quiescent liquid ambient with benchmarking against CFD results.
- Summary, closure and suggestions for future work.

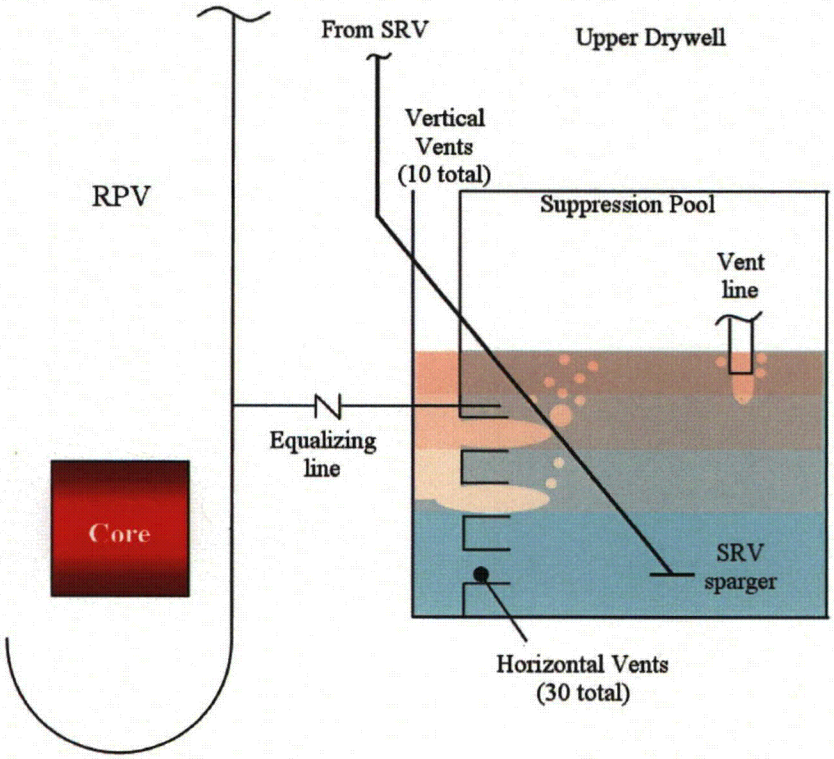

Figure 1.1 Schematic showing RPV and SP components and piping in ESBWR containment

References

Brown, W. G. (1962). Natural convection through rectangular openings in partitions – 2. *International Journal of Heat and Mass Transfer*, 5, 869-878.

Brucker G. G., & Sparrow E. M. (1977). Direct contact condensation of steam bubbles in water at high pressure," *International Journal of Heat and Mass Transfer*, 20 (4), 371-381.

Delhaye, J. M., Goit, M., & Riethmuller, M. L. (1981). Thermodynamics of Two-Phase Systems for Industrial Design and Nuclear Engineering. Washington: Hemisphere Publishing Corporation.

Gamble, R.E., Nguyen, T. T., Shiralkar, B. S., Peterson, P. F., Greif, R., & Tabata, H. (2001). Pressure suppression pool mixing in passive advanced BWR plants. [Electronic version]. *Nuclear Engineering and Design*, 204, 321-336.

Grandt, D. (March 17-20, 1997). Thermal-Hydraulic Modeling Requirements for Next Generation Reactor Safety Analysis Codes. In *The OECD/CSNI Specialist meeting on Advanced Instrumentation and Measurement Techniques*. Santa Barbara, CA.

Hunt, G. R., Cooper, P., & Linden, P. F. (2001). Thermal stratification produced by plumes and jets in enclosed spaces. [Electronic version]. *Building and Environment*, 36, 871-882.

Ishii, M. (Nov. 5-8, 1996). Views on Future of Thermal Hydraulic Modeling. In *The OECD/CSNI Workshop on Transient Thermal Hydraulic and Neutronic Codes Requirement*.

Kelly, J. M. (Nov. 5-8, 1996). Thermal Hydraulic Modeling Needs for Passive Reactors. In *The OECD/CSNI Workshop on Transient Thermal Hydraulic and Neutronic Codes Requirement*.

Kelly, J. M. (March 17-20, 1997). Constitutive Model Development Needs for Reactor Safety Thermal Hydraulic Codes. In *The OECD/CSNI Specialist meeting on Advanced Instrumentation and Measurement Techniques*. Santa Barbara, CA.

Norman, T. L., Park, H. S., Revankar, S. T., Ishii, M., Vierow, K., & Kelly, J. M. (2005). Steam-air mixture condensation in a subcooled water pool, Facility design and scoping tests. PU/NE-05-19.

Ortiz, M. G., & Ghan, L.S. (1992). Uncertainty analysis of minimum vessel liquid inventory during a small break LOCA in a B&W plant: An application of the

CSAU methodology using the RELAP5/MOD3 computer code. NUREG/CR-5818

Pitts J. H. (1980). Steam chugging in a boiling water reactor pressure-suppression system, *International Journal of Multiphase Flow*. 6 (4).

Rohatgi, U. S., Saha, P., & Chexal, B. K. (October 1985). Considerations for realistic ECCS evaluation methodology for LWRs. In *Third International Meeting on Reactor Thermal Hydraulics*. Newport, RI.

Wilson, G. E., et al. (June 1997). Phenomena identification and ranking tables for Westinghouse AP600 small break loss of coolant accident, main steam line break, and steam generator tube rupture scenarios. NUREG/CR-6541

Wulff W., et al. (March 1994). Uncertainty analysis of suppression pool heating during an ATWS in a BWR-5 plant: An application of the CSAU methodology using the BNL engineering plant analyzer. NUREG/CR-6200.

2. OBJECTIVES AND TECHNICAL APPROACH

2.1 Objectives and Milestones

The main objectives of these separate-effects jet condensation research are to:

1. Perform a detailed literature survey on the steam/noncondensable mixture jet condensation in a subcooled pool and its relevance to advanced reactor safety.
2. Obtain data on jet condensation, pool mixing and thermal stratification for different nozzle sizes, injection fluxes and pool initial conditions (namely pool subcooling) in a scaled down LWR suppression pool design.
3. Evaluate TRACE code model capabilities using the experimental data.
4. Develop boundary maps and stand-alone models on condensation, jet dynamics, pool mixing and thermal stratification that can be used in best estimate system codes such as TRACE.

Most of the milestones in the above objectives are addressed in this part of the final report. Scoping and feasibility tests as well as tests that are based on prototypic accident conditions have been performed and compiled into a comprehensive database. In the experimental program, a scaled model pool representing $1/10^{th}$ of the ESBWR suppression pool was utilized to conduct separate-effects experiments. Key measurement instruments such as thermocouples were mounted within an instrumentation frame that was inserted inside the test section for measuring quasi-steady pool thermal response. A data acquisition system was used for recording data which was plotted as surface maps, and pool thermal response based on certain boundary conditions were recast in the form of boundary maps to provide some insight into the phenomena of interest. Measurements taken in the experiments include the following:

- Temperature (thermocouples)
- Recirculation rates (high speed photography)

- Flow rates (vortex- and mass- flow meters)
- Visualization (high speed camera for jet-plume trajectory)

Test procedures and a justification for testing conditions are discussed for this scaled down, reduced pressure test facility. The ultimate objective is to utilize the information gathered from these scaled subcooled pool experiments and develop models for use in codes. The major objective is then to gather experimental data on pool mixing, thermal stratification and local condensation rates in support of model development.

The overall objectives of this research are to obtain data on the aforementioned phenomena in a separate effects test facility, develop models for pool dynamics and thermal stratification, and assess code models using the data. The following phenomena are the main focus of the present research efforts:

- Direct contact condensation with and without non-condensable gas,
- Mixing in the suppression pool by thermal plume and rising bubbles and entrainment of ambient liquid in an initially quiescent pool and
- Identifying when the global phenomenon of thermal stratification dominated the pool thermal characteristics.

2.2 Technical Approach

The direct contact condensation tests simulate the condensation of steam/noncondensable mixture ensuing from horizontal vents into the SP. A separate effects test facility has been designed such that it has horizontal discharge lines and a large pool of subcooled water that represents a scaled sector of a prototypic suppression pool and incorporates instrumentation specific to key measurement quantities such as temperature and pressure. The steam is supplied from the reactor pressure vessel (RPV) of the PUMA (Purdue University Multi-dimensional integral test Assembly) facility (Ishii, et al, 1998). The pool is operated at atmospheric pressure conditions and has visual

ports for flow visualization and photography. The test parameters include the nozzle size, noncondensable concentration, steam flow rate, SP pool water temperature, and horizontal vent elevation. Specific instrumentation for these tests include the high speed video camera (500-1000 frames per second) to capture the direct contact condensation phenomena and recirculation behavior. A distributed thermocouple system is used to study the developing temperature profile and stratification, and water recirculation. Detailed 2-D temperature profiles are obtained for the pool. Thermocouples are also located in the gas space above the pool. The pool circulation flow rates are quantified with sequential photographic images.

Data are obtained on the rate of steam condensation, vertical temperature gradients in the pool, temperature distribution, recirculation rates, gas space temperature, non-condensable gas concentration, and flow visualization. The qualitative data from flow visualization with high speed video camera is used to understand the gas-liquid interface phenomena, bubble formation and collapse and liquid circulation. The data base is used to assess the models of the rapid condensation process, thermal stratification and mixing, accumulation of hot liquid in a buffer layer due to condensation or convection, thermal front in stratified systems, and entrainment of subcooled water into a rising plume. The focus would be on the simplest effective modeling approach that can be sufficient to describe the jet extent, jet breakup, jet-plume mixing, penetration of jet-plume, condensation, thermal gradients in pool, and bulk recirculation. The initial NC concentration considered ranges from 0% to 20%. The SP initial water temperature range considered is 20°C to 60°C. Details of the test strategy, instrument implementation, and test matrix are discussed in Chapters 4 and 5.

References

Grandt, D. (March 17-20, 1997). Thermal-Hydraulic Modeling Requirements for Next Generation Reactor Safety Analysis Codes. In *The OECD/CSNI Specialist meeting on Advanced Instrumentation and Measurement Techniques*. Santa Barbara, CA.

Ishii, M. (Nov. 5-8, 1996). Views on Future of Thermal Hydraulic Modeling. In *The OECD/CSNI Workshop on Transient Thermal Hydraulic and Neutronic Codes Requirement*.

Ishii, M., Revankar, S.T., Leonardi, T., Dowlati, R., Bertodano, M. L., Babelli, I., et al. (1998). The three–level scaling approach with application to the Purdue University Multi-Dimensional Integral Test Assembly (PUMA). [Electronic version]. *Nuclear Engineering and Design*, 186, 177-211.

Ishii, M., Sun, X., Revankar, S. T., Vierow, K., Xu, Y., Kim, S., Yoon, H. J., Cheng, L., Ozar, B., Vasavada, S., Paranjape, S., Kuran, S., Situ, R., Choi, S. W., Lim, J., Norman, T., Woo, K. S., Yang, J. (2004). Second scaling and scientific design study for GE ESBWR relative to PUMA facility with volume ratio of 1/475. PU/NE-04-04 Proprietary

Kelly, J. M. (Nov. 5-8, 1996). Thermal Hydraulic Modeling Needs for Passive Reactors. In *The OECD/CSNI Workshop on Transient Thermal Hydraulic and Neutronic Codes Requirement*.

Norman, T. L., Park, H. S., Revankar, S. T., Ishii, M., Vierow, K., & Kelly, J. M. (2005). Steam-air mixture condensation in a subcooled water pool, Facility design and scoping tests. PU/NE-05-19.

3. LITERATURE SURVEY

3.1 Introduction

Thermal stratification, vapor and jet plume behavior, condensation, circulation and mixing within large enclosed volumes are regarded as important phenomena which affect the thermal response of not only nuclear reactors but various industrial systems. For instance, energy storage tanks that manage heated water from a solar collector maintain inflow of cold water at the bottom of the tank and outflow of warm water at the top, with thermoclines that characterize the temperature distribution within the pool being initially separated and interacting by gravitational effects (Al-Najem & El-Refaee, 1997). In solar-fueled power plants, direct contact condensation of steam bubbles in a pressurized water tank has been studied as a means of storing thermal energy (Brucker & Sparrow, 1977).

The redistribution of temperature strata due to localized heat sources in an enclosed building is also of considerable interest to implementing building ventilation and heating procedures (Hunt et al., 2001). Stratified temperature layers that arise in such a case may degrade as a consequence of mixing factors such as natural convection between the isotherms (Brown, 1962). Recirculating flow caused by conduction due to the containment walls in the case of solar heaters (Cruz *et al.,* 2002), or pool mixing caused by injection of two-phase vapor mixtures into a suppression pool (SP) during the blowdown phase of a boiling water reactor (BWR) accident influence the thermal response of the containment.

A detailed literature review is presented in this chapter in which the phenomena of pool thermal stratification and mixing due to submerged sources are discussed. Plume characterization and modeling efforts are also discussed along with flow regime maps and associated condensation heat transfer relations developed in various pool systems.

3.2 Pool Stratification and Mixing

The buoyant jetting regime is one characteristic type of discharge that can occur in the case of steam injection to the SP depending on the thermal-hydraulic conditions in the drywell and wetwell (Gamble et al, 2001). The general terms 'buoyant jet', 'jet plume' or 'forced plume' refer to either a pure buoyant plume or a pure momentum jet, or may refer to a combination of these two limiting cases. The term 'forced plume' refers to a source that is characterized by an internal balance of momentum, buoyancy, and turbulent friction. A 'pure plume' is therefore a source of buoyancy with ideally zero momentum, where buoyancy gives rise to the normal force at the interface, in which the gas-liquid interface can develop Rayleigh-Taylor instabilities due to the heavier liquid being above the lighter injected vapor. On the other extreme, the term 'jet' refers to a source that is characterized by a balance of momentum and turbulent friction. A 'pure jet' is therefore a source of momentum with ideally zero buoyancy, where the injection velocity gives rise to the tangential shear force at the vapor-liquid interface where Kelvin-Helmholtz instabilities can develop due to perturbations in the shear force across the interface. The Kelvin-Helmholtz instability is usually the result of the appearance and growth of vortices that result in a turbulent mixing layer. Motion due to instabilities, can act as a mechanism to increase the surface area available for heat transfer processes.

A condensing 'forced plume', which is expected to be the scenario in the SP, therefore refers to any transition between these two aforementioned extremes. In such a case there is a competing effect between buoyancy which acts to stratify the pool interior, and momentum which tends to mix the pool. So by altering the relative magnitudes of the buoyancy and momentum fluxes, as dictated by the drywell and wetwell conditions, it is possible to transit from the stratified case to the mixed case within the SP. Strong thermal stratification limits the pool heat removal performance.

3.2.1 *Approaches to Evaluating Stratification Characteristics in Systems*

Buoyancy forces can be simulated not only from density differences due to an inversion of temperature strata but also due to variations in solute concentration if the density of a stratified layer of a single-component fluid increases upwards and an unstable configuration is achieved, as is the case when fresh water is injected below a solution of salt-water. Gebhart et al (1988) studied a saline problem in which low-momentum pure-water lower-density jets were injected into a solute-stratified volume of higher-density salt-water. The resulting viscous shearing of the axisymmetric buoyant pure-water jets was found to induce a toroidal flow around the jet.

Consider first a volume of pure water (whose density decreases with increasing temperature) with a steam bubble released at a submerged location within the volume. The steam, which is initially displaced upwards, is initially warmer than the ambient liquid and upon condensing, its temperature rapidly declines to that of the surrounding fluid but remains less dense than the ambient fluid and remains in the upper region of the volume. Therefore buoyancy displaces the fluid from the lower regions to another more stable upper location.

Consider next a saline solution in which density decreases upward. If a particle of fresh water is injected from below, it increases in salt concentration; however, in this case the buoyancy force acts to restore that particle to its original position at the pool base as its density increases. A displaced particle of fluid loses any excess heat more rapidly than it would gain solute, the reason being that the diffusivity of heat is usually much greater than the diffusivity of a solute (Nield, 1967).

Peterson et al (1991) reported experiments where stable stratification with well defined sharp interfaces occurred when dyed water was injected at different submergences into salt water. Convective mixing was observed near the center but was damped as the fluid flowed away from the plume with the sharp interface being observed further from the center. The onset of convection induced by thermal and solute

concentration gradients in a horizontal layer of a viscous fluid occurs when the thermal Rayleigh and solute Rayleigh numbers respectively reach some critical value. Using the Boussinesq approximation for a quasi-incompressible fluid, one can write the governing equations for a thermo-saline problem:

$$\nabla \cdot \vec{u} = 0 \tag{3.4}$$

$$\frac{\partial \vec{u}}{\partial t} + (\vec{u}.\nabla)\vec{u} = -\frac{\rho}{\rho_0} g\hat{k} - \frac{1}{\rho_0}\nabla P + \upsilon \nabla^2 \vec{u} \tag{3.5}$$

The one-dimensional convective transport equation of temperature and concentration are

$$\frac{\partial T}{\partial t} + \vec{u} \cdot \nabla T = \kappa \nabla^2 T \tag{3.6}$$

$$\frac{\partial C}{\partial t} + \vec{u} \cdot \nabla C = \kappa' \nabla^2 C \tag{3.7}$$

$$\rho = \rho_0 \left[1 - \alpha (T - T_0) - \alpha' (C - C_0) \right] \tag{3.8}$$

The temperature and concentration at the lower and upper boundary separated by vertical distance d have relatively uniform quantities given by T_0, C_0 and T_1, C_1 respectively, where

$$\beta = \frac{(T_0 - T_1)}{d}, \ \beta' = \frac{(C_0 - C_1)}{d} \tag{3.9}$$

where the thermal Rayleigh number is given by

$$Ra_T = \frac{\alpha \beta g d^4}{\kappa \upsilon} \text{ with } \Pr = \frac{\upsilon}{\kappa} \tag{3.10}$$

and solute Rayleigh number is given by

$$Ra_C = \frac{\alpha' \beta' g d^4}{\kappa' \upsilon} \text{ with } Sc = \frac{\upsilon}{\kappa'} \tag{3.11}$$

The following are also defined as:

κ = thermal diffusivity

κ' = solute diffusivity

α = thermal coefficient of expansion

α' = analogous solvent coefficient

Due to the slower rate of stratification in a saline environment, a solute experiment would be ideal to track the movement of the density strata. Hunt et al (2001) and Chen & Cardoso (2000) show behavior of plumes and jets and their impact on two-layer density stratified systems.

3.2.2 *Gas Injection and Absorption in Liquid*

In order to have a jet exiting a vent, a critical velocity, u_{g_0}, needs to be exceeded in order for the vent to provide more volumetric flow than that which can be transferred away by buoyancy (Kolev, 2002). For the case of gas injection into a quiescent pool, the volumetric gas flow is given by equation 3.12

$$\dot{V} = A_0 u_{g_0} \tag{3.12}$$

where the vent cross-section is given by

$$A_0 = \frac{\pi D_0^2}{4} \tag{3.13}$$

If the pool surface cross-sectional area is A, the gas volume fraction immediately downstream of the vent is α_g, and the bubble velocity is u_{g_∞}, then for an approximately constant pressure:

$$\alpha_g A u_{g\infty} = A_0 u_{g0} \tag{3.14}$$

For the case of the largest bubble diameter D_{g0} in static equilibrium issuing from the vent, the buoyancy force = surface force and is given by:

$$\frac{\pi D_{g\infty}^3}{6} g\left(\rho_f - \rho_g\right) = \pi D_{g0}\sigma \tag{3.15}$$

$$D_{g\infty} = \left(\frac{6\sigma D_{g0}}{g\Delta\rho}\right)^{1/3} \tag{3.16}$$

It was observed experimentally by Kutateladze and Styrikovich (1958) (in Kolev, 2002) that the largest bubble diameter is:

$$D_{g\infty} \approx \left(\frac{4\sigma D_{g0}}{g\Delta\rho}\right)^{1/3} \tag{3.17}$$

whereas the Rayleigh-Taylor instability wavelength is given by

$$\lambda_{R-T} = \left(\frac{\sigma}{g\Delta\rho}\right)^{1/2} \tag{3.18}$$

So if $D_{g\infty}$ is of the order of D_{g0}, then for the simple momentum balance (buoyancy force = surface force) to be valid the following must hold: $D_{g\infty} < \lambda_{R-T}$. For the simple momentum balance, the effect of the gas momentum is not taken into account and this is not sufficient to describe the actual bubble size after jet fragmentation. A steady state momentum balance would be in the form: buoyancy + momentum = drag force + virtual mass force + surface force.

For a bubble released at a submerged depth, the buoyancy flux is of the order of the bubble rise velocity. The velocity with which a bubble will rise as a result of convection is given by Stoke's velocity:

$$v = \frac{1}{3}\frac{r^2 g\alpha\Delta T}{\upsilon} \tag{3.19}$$

where υ is the kinematic viscosity and α is the coefficient of thermal expansion.

Nukiama and Tanasava (1938) (in Kolev, 2002) found that bubble size distribution during condensation of bubbles follow the law:

$$P(D_1) = 4\left(\frac{D_1}{D_1'}\right)^2 \exp(-2D_1/D_1') \tag{3.20}$$

Here $P(D_1)$ is the probability a bubble has size between D_1 and $D_1 + \delta D_1$, D' is the most probable particle size or the size where the probability function is a maximum. The bubble surface heat flux can be determined once the time interval in which the distribution remains unchanged can be determined. In such a case, during this time interval, high frequency eddies contact the bubble surface so that heat transport from the bubble surface to the eddy is only possible via molecular diffusion.

In high flow steam injection at submerged depths, condensation can occur over a short distance (Jirka & Harleman, 1979) if the pool is sufficiently subcooled. This can lead to a variable balance between buoyancy and inertia along the jet-plume trajectory where it can be defined by variable transition properties consisting of a buoyant condensing vapor upstream followed by a hot liquid turbulent jet downstream. The presence of noncondensable gas mixed with steam has the effect of inhibiting condensation and can affect the condensation flow regimes (Chun et al, 1996). A summary of condensation regimes and related experimental conditions performed in various studies are shown in Table 3.1. In the case where high to pure noncondensable gas concentrations occur, a bubbly plume consisting of a buoyant inner core and outer plume entraining ambient liquid have been observed to drive the mixing in the surrounding fluid (Chen & Cardoso, 2000). In such a case, the driving mechanism for mixing is the result of turbulent shear stresses.

3.3 Plume Characterization and Modeling

3.3.1 *Vapor Plume and Jet Plume Characterization*

For a gas of density ρ_g ($\rho_f - \Delta\rho$) relative to ambient density ρ_f that is forced through a vent of cross-sectional area A_s with volumetric flow rate Q_0, a momentum flux and buoyancy flux can be defined respectively (Hunt et al, 2001) as follows:

$$M_0 = Q_0^2 A_S^{-1} \tag{3.21}$$

and

$$B_0 = g_0' Q_0 \tag{3.22}$$

where $g_0' \equiv g\Delta\rho/\rho_f$ is the reduced gravity of the input, and $\rho_{f,0}$ the initial density of the interior. The entrained water plume coupled to the buoyancy flux of the gas bubbles, gives a reduced buoyancy flux of:

$$B_0 = g\left(\frac{\rho_g - \rho_f}{\rho_f}\right)\left(Q_0 - Q_{bj}\right) \tag{3.23}$$

with Q_{bj} being the flow rate of the entrained water.

Christensen & Peterson (2001) modeled a Morton plume, which is an axisymmetric vertically injected buoyant jet generated by thermal expansion, in a 1-D stratified environment. A buoyancy flux was determined and the volumetric flow rate carried by the axisymmetric buoyant jet was assumed from the analysis of Peterson et al (1998), which carried the Taylor entrainment constant. The buoyancy flux was given by Christensen & Peterson (2001) as:

$$B = \int_0^b -\omega(r) g \frac{\rho_{jet}(r) - \rho_{amb}}{\rho_{amb}} 2\pi r.dr \tag{3.24}$$

where the radial spread of the jet at an axial z location is given by: $b = \frac{6}{5}\alpha z$ (equation 3.38), where α is the entrainment coefficient, with ω being the entrainment velocity. The buoyant jet volumetric flow rate was derived by the authors as:

$$Q_{bj} = \frac{6\pi}{5}\alpha^{4/3}\left(\frac{18}{5\pi}\right)^{1/3} B^{1/3} z^{5/3} \tag{3.25}$$

In addition, the added buoyancy flux due to a heat source is given by:

$$B_0 = \frac{g\alpha E}{\rho_g c_{p,g}} \tag{3.26}$$

with E being the energy of the heat source and α being the coefficient of thermal expansion, and the time it takes for the plume to increase the ambient fluid by 1 °C is:

$$t_{1^oC} = \frac{V \rho_g c_{p,g}}{E} \tag{3.27}$$

with V being the volume of the enclosure. As the ambient fluid is heated up by a steam plume, the supply buoyancy flux due to the heat source decreases with time (Hunt, 2001), this is given by:

$$B(t) = Q_0 g \left(\frac{T_g - T_f(t)}{T_f(0)} \right) \tag{3.28}$$

where Q_0 is the source volumetric flow rate. The rate of accumulation of buoyancy is then given by:

$$\frac{dg'}{dt} = \frac{B(t)}{V} \tag{3.29}$$

where $g'(t) = g\left(\rho_f(t) - \rho_f(0)\right)/\rho_f(0)$, this gives the following:

$$\frac{dT_f}{dt} = \frac{\left(Q_0 - Q_{bj}\right)}{V}\left(T_g - T_f(t)\right) \tag{3.30}$$

Integrating with initial condition $T(0) = T_0$ at $t = 0$ gives:

$$T_f(t) = T_g - \left(T_g - T_0\right)\exp\left(-t/t_c\right) \tag{3.31}$$

Here a time constant is defined as:

$$t_c = V/\left(Q_0 - Q_{bj}\right) \tag{3.32}$$

This changes the initial reduced gravity term of the source:

$$g'(t) = g_0'\left(1 - \exp\left(-t/t_c\right)\right) \tag{3.33}$$

This also changes the buoyancy flux term which is reduced over a finite time and the jet length therefore increases with time, indicating that momentum effects can dominate buoyancy effects over some time for a certain initial momentum and buoyancy flux.

If H is the submerged height of the exit of a vertical oriented jet-plume, in which the momentum and buoyancy fluxes act in the same direction, then the jet length L_j/H, which gives a measure of the stratifying properties of a forced plume, is given by:

$$\frac{L_j}{H} = \frac{M_0^{3/4}}{HB_0^{1/2}} \tag{3.34}$$

For a pure jet, $L_j/H \to \infty$, and the interior remains unstratified. However, stratification occurs when $L_j/H \to 0$. The ratio L_q/H gives a measure of the distance over which the initial volume flux is significant compared with that entrained by the plume, and is given by:

$$\frac{L_q}{H} = \frac{Q_0}{HM_0^{1/2}} \tag{3.35}$$

The properties of a forced plume at the source location are determined by the Archimedes number, given by:

$$Ar(0) = \left(\frac{L_q}{L_j}\right)^2 \tag{3.36}$$

Baines & Turner (1969) described the conditions for overturning motion to take place. A measure towards the tendency of overturning was given by the inertia to buoyancy ratio:

$$\frac{I}{B} = \frac{9\alpha}{10}\left(\frac{H}{R}\right)^2 \tag{3.37}$$

where large values of this ratio imply instability. α is an entrainment constant given by Morton (1969) with b being the radius at which the mean axial velocity falls exponentially as 1/e given by:

$$b = \frac{6\alpha}{5} z \tag{3.38}$$

In the case where the momentum and buoyancy fluxes act 90-degrees initially with the momentum flux being oriented horizontally, the resultant flux can be simulated as an effluent with initial density ρ_0 projected at angle θ_0 to the horizontal (Bosanquet et al, 1961). Horizontal momentum conserved at any point along any jet trajectory is given by

$$M \cos\theta = M_0 \cos\theta_0 \tag{3.39}$$

Therefore, the rate of change of vertical momentum with horizontal displacement = $d(M \sin\theta)/dx$, where

ρ_s = density of surrounding fluid,

ρ = density of jet fluid, and

$$\rho = \frac{(\rho_0 V_0 + \rho_s V_s)}{V}$$

The gravity force acting an incremental volume of jet fluid contained by planes perpendicular to the jet axis: $F = -g(\rho - \rho_s)Vdx$

Vertical force balance:

$$d(M \sin\theta)/dx = -g(\rho - \rho_s)Vdx \tag{3.40}$$

It may not be possible to derive a relation for y in terms of x. A relation of x to tan θ is given by the ratio of vertical to horizontal components of momentum flux:

$$\tan\theta = \frac{M \sin\theta}{M \cos\theta} = \frac{M \sin\theta}{M_0 \cos\theta_0} \tag{3.41}$$

$$\frac{d^2(\tan\theta)}{dx^2} = \frac{1}{M_0\cos\theta_0}\frac{d^2(M\sin\theta)}{dx^2} = \frac{-g(\rho_0-\rho_s)}{M_0\cos\theta_0}\frac{dV_0}{dx} \tag{3.42}$$

3.3.2 *Integral Plumes and Lumped-Parameter Models*

An integral plume model can be useful once a coefficient of entrainment can be determined for a steady bubble plume. The basic equations for mass and momentum of a steady bubble plume in a non-stratified ambient (Bombarbelli et al, 2001) are:

$$\frac{d\mu}{dz} = 2\alpha(\pi M)^{1/2} \tag{3.43}$$

$$\frac{dM}{dz} = \frac{(\rho_w-\rho_p)}{\rho_p} g\lambda^2 \frac{\mu^2}{M} \tag{3.44}$$

where the following quantities are defined:

$\mu = \pi b^2 w$ = volume flux of plume water

$M = \pi b^2 w^2$ = momentum flux of plume water

b = plume radius, of which a fraction λ is assumed to contain bubbles (bubbly core)

w = liquid velocity of the plume

α = entrainment coefficient

ρ_w = water density

ρ_p = plume bubble-water mixture density, $\rho_P = (1-V_g)\rho_w + V_g\rho_g$

V_g = volume fraction of gas in the mixture

ρ_g = gas density

z = vertical coordinate

N = number of (spherical) bubbles crossing a section of plume per unit time

r = bubble radius

So a height-dependent volumetric flow is given by

$$Q_g(z) = \frac{4}{3}\pi r^3 N \tag{3.45}$$

Dividing by the cross-sectional area of the bubbly plume core and by the bubble velocity gives V_g.

$$V_g = \frac{Q_g}{\left[\left(w + w_b\right)\pi\lambda^2 b^2\right]} \tag{3.46}$$

w_b = bubble slip velocity (bubble velocity relative to liquid) and $\rho_g \ll \rho_w$

Further manipulation gives the following change in volume flux and momentum flux with height:

$$\frac{d\left(\pi b^2 w\right)}{dz} = 2\alpha\pi b w \tag{3.47}$$

$$\frac{d\left(\pi b^2 w^2\right)}{dz} = \frac{Q_g(z)g}{\left(w + w_b\right)} \tag{3.48}$$

Influx variables: $$f(z) = \frac{Q_g(z)}{Q_g(0)} = \left[\frac{r(z)}{r(0)}\right]^3 \tag{3.49}$$

$$\frac{d\mu}{dz} = 2\alpha\left(\pi M\right)^{1/2} \tag{3.50}$$

$$\frac{dM}{dz} = \frac{Q_g(0)gf(z)}{\left(\frac{M}{\mu} + w_b\right)} \tag{3.51}$$

Assume $Q_g(z)$ is known and w_b, α are constant, with initial conditions: $\mu(0) = \pi b_0^2 w_0$, $M(0) = \pi b_0^2 w_0^2$ and w_b being the velocity scale, the scaling of integral plume equations can be given by the following (Bombarbelli et al, 2001):

Then length scale is $D = \frac{Q_g(0)g}{4\pi\alpha^2 w_b^3}$ which implies the non-dimensional variables:

$z = D\hat{z}$, $\mu = 2\alpha\sqrt{\frac{\pi D^3 Q_g(0)g}{w_b}}\hat{\mu}$, $M = \frac{gQ_g(0)D}{w_b}\hat{M}$. Assuming $f(z) = 1$, then

$\frac{\partial\hat{\mu}}{\partial\hat{z}} = \left(\hat{M}\right)^{1/2}$, $\frac{\partial\hat{M}}{\partial\hat{z}} = \frac{1}{1 + \frac{\hat{M}}{\hat{\mu}}}$, So $\hat{\mu}(0) = \frac{\hat{b}_0^2\hat{w}_0}{4\alpha^2}$, $\hat{M}(0) = \hat{w}_0\hat{\mu}(0)$

Initial Densimeteric Froude Number

$$Fr = \frac{w}{\left[2\lambda bg\frac{(\rho_w - \rho_b)}{\rho_w}\right]^{1/2}} = \frac{\sqrt{\lambda\hat{b}(1+\hat{w})\hat{w}}}{2\alpha\sqrt{2}} \tag{3.52}$$

Jirka & Harleman (1979) defined a buoyancy flux for vertical upward buoyant jet injection as:

$$B(z) = I_3 w_c \beta g \theta_c b \tag{3.53}$$

and

$$\frac{dB}{dz} = 0 \tag{3.54}$$

where w_c and θ_c are the centerline velocity and temperature difference $(T(x,y) - T_a)$ respectively, $\beta g \theta_c$ is a buoyant acceleration, b is the lateral spread of the jet, and I_3 is a profile-dependent coefficient given by:

$$I_3 = \int_{-\infty}^{\infty} fg \; d\eta \tag{3.55}$$

where $\eta = x/b$, and f and g represent appropriate functions that approximate the observed bell-shaped profiles.

3.3.3 *Dimensionless Characterization of Buoyant Jets for Scaling*

Peterson et al, (1991) used a densimetric Froude number to characterize the force balance within the buoyant jet defined by:

$$\mathrm{Fr_d} = \frac{\mathrm{U}}{\sqrt{\mathrm{g}\frac{\rho_a - \rho_i}{\rho_a}\mathrm{H}}} = \frac{\text{momentum flux}}{\text{buoyancy force}} \tag{3.56}$$

where U = injection velocity, ρ_i = density of injected fluid, ρ_a = density of ambient fluid, and H = pool height. Therefore, for an ideal jet, $Fr_d = \infty$. A jet plume can then be defined by a constant densimetric Froude number given by Fr_{dp}. The buoyant jet entrains liquid from the ambient pool and buoyancy acceleration which is associated with strong shear effects may result in strong turbulence. The variability of jet coefficients such as the entrainment coefficient as the jet transitions to a plume needs to be assessed by experimental information since this is a variable function and is dependent upon the densimetric Froude number (Jirka & Harleman, 1979). This variability is further complicated by the presence of non-condensable gases discharged with steam into the pool, which acts to inhibit condensation and enhance buoyancy forces. A local Richardson number defines the stratification stability along the length of the jet. This is given by:

$$\mathrm{Ri} = \frac{g(\partial\rho/\partial z)}{\rho(\partial v_r/\partial z)^2} = \frac{g((\rho_a - \rho_i)/\mathrm{D}_i)}{\rho_a(\mathrm{U}/\mathrm{D}_i)^2} = \frac{g((\rho_a - \rho_i)/\rho_a)\mathrm{D}_i}{\mathrm{U}^2} = \frac{\text{buoyancy force}}{\text{shear force}} \tag{3.57}$$

The buoyancy force spanning the length of the jet may not be constant; however, the local Richardson number gives the local gradient at one point. The Richardson number can also be utilized as a system parameter for the pool volume. This is given by:

$$\mathrm{Ri}_s = \frac{g((\rho_a - \rho_i)/\mathrm{H})}{\rho_a(\mathrm{U}/\mathrm{H})^2} = \frac{g((\rho_a - \rho_i)/\rho_a)\mathrm{H}}{\mathrm{U}^2} = \frac{1}{\mathrm{Fr}_d^2} \tag{3.58}$$

Gamble et al (2001) refer to this as the pool Richardson number that defines the case when the inertia of the jet causes stratification to degrade in the SP; this is defined as:

$$\mathrm{Ri}_{\mathrm{pool}} = \frac{g((\rho_a - \rho_{jet})/\rho_a)\mathrm{D}_i}{\mathrm{U}^2}\left(\frac{\mathrm{H}_{sf}}{\mathrm{D}_i}\right)^2 \tag{3.59}$$

Theofanous et al. (1976) examined the problem of predicting mass transfer coefficients for gas absorption by turbulent liquids. Forced submerged vertical turbulent

jet flows were considered as the primary mixing mechanism. Two approaches adopted were based on idealized eddy structures of turbulence and the concept of surface-tension-damped laminar sublayer to assess its implications for mass transfer at a free surface. The jet Reynolds number determines whether the jet will be turbulent. This is given by:

$$\mathrm{Re}_{\mathrm{jet}} = \frac{\rho_i \mathrm{UD}_i}{\mu} = \frac{\text{inertia force}}{\text{viscous force}} \qquad (3.60)$$

In the case of the SP, a high energy turbulent jet can impinge upon the far vertical wall causing it to expand radially in all directions with some degree of interaction with the pool free surface (Gamble et al, 2001) or be limited by the interactions of adjacent jets. In this instance the free-surface Froude number is given by:

$$\mathrm{Fr}_{\mathrm{surface}} = \frac{\mathrm{U}}{(g\mathrm{H})^{1/2}} \qquad (3.61)$$

Where H is the distance of the jet exit to the far wall. Gamble et al (2001) also defines a Froude number that governs the impingement interaction of the jet at the far wall in terms of the jet thickness $\delta_r(z)$ at the vertical location from the impingement stagnation point, this is given by:

$$\mathrm{Fr}_{\mathrm{imp}} = \frac{\mathrm{U}^2}{g(\delta_r/2)} \qquad (3.62)$$

The non-condensable injection period is brief, where a period of a few seconds is needed to completely purge the non-condensable gas from the DW to the SP, and which imparts negligible energy to the pool (Gamble et al, 2001). The longer steam injection period increases the energy content of the pool, however, the non-condensable gas is free to rise to the pool surface and cause surface deformation or 'pool swelling'. The dynamic thrust of an eddy at the pool surface has been evaluated by Theofanous et al, (1976) by considering both the large eddy model and the small eddy model. The relevant turbulent

properties for the large eddies are based on the turbulence intensity V and macroscale L that defines the turbulence Reynolds number given by:

$$\mathrm{Re}_{\mathrm{t}} = \frac{\mathrm{LV}}{\nu} \tag{3.63}$$

Small scale turbulent motions are more effective in transferring mass across a free surface than the large ones. The small scale dissipative motions are more controlling, and the Kolmogorov velocity and length scales v_k and l_k, and the ratio of the characteristic times (Theofanous et al, 1976) of the large-scale and small-scale motions is given by:

$$\mathrm{Re}_{\mathrm{t}}^{1/2} = \frac{\mathrm{L/V}}{l_k / v_k} \tag{3.64}$$

Following the scaling laws of Peterson et al (1998), for a stratified volume, the residence time of the buoyant jet within a volume, as well as the characteristic frequency of the jet, determines the characteristic time ratio for which mass, momentum and energy are transported during the jet plume residence time in the volume (see section 5). Specifically, the residence time of a buoyant jet is defined as the ratio of the volume occupied by the jet to its volume flow rate. The characteristic frequency is defined as the ratio of the rate of transport of mass, momentum, energy or species into the volume to the capacity of the volume to store these quantities.

A two-phase jet Richardson is given by Peterson et al (1998) to be:

$$\mathrm{Ri}_{\mathrm{d}} = \frac{g\pi^2 d_{bj}^5}{16 x_g^2 Q_m^2} \tag{3.65}$$

where the specific buoyancy flux added by the noncondensable gas is given by:

$$B = g x_g Q_m \tag{3.66}$$

where Q_m is the volumetric flow rate of the steam-gas mixture, x_g is the mole fraction of the non-condensable gas, and d_{bj} is the buoyant jet diameter. Peterson et al (1998) also gave a scaling parameter for stratified systems that preserve the jet Richardson numbers between scaled and prototypical systems for fluids of the same densities. The ratio of the scaled volume flow rate to the prototypical one was given as:

$$Q_R = \frac{Q_S}{Q_P} = n_{bj,R} d_{bj,R}^{5/2} \tag{3.67}$$

3.3.4 *Mechanistic Approaches to Plume Modeling*

In lumped-parameter models such as those of McDougall (1978) and Milgram (1983), the conservation equations for mass and momentum of the mixture are solved in integral form. The rise velocity of the plume and void radial distribution are assumed to have either Gaussian or top-hat profiles. Dynamic coupling between the plume-proper boundary and the pool ambient is achieved by assuming a constant coefficient of entrainment determined empirically from relevant data. In recent times, CFD has offered a way to calculate actual velocity distributions from the conservation equations of the two-phase dispersed flow using suitable models for the interaction of the phases. Another approach is to employ the two-fluid model which treats the liquid and vapor bubbles as interpenetrating continua (Ishii, 2004) to solve two separate sets of conservation equations for each phase with closure being possible from constitutive equations representing the phasic interactions.

As opposed to lumped-parameter models which rely heavily on experimental data, Smith (1998) used the two-fluid model for a submerged vertically-oriented plume with no mass or heat transfer. This approach accounts for the actual mechanisms that are involved in the transfer of momentum. In this case, the liquid and gas volume fractions are needed for a certain gas superficial velocity. The liquid superficial velocity was held as zero and the momentum transfer due to interfacial drag was solved numerically. This

problem was considered a dispersed flow situation, and turbulent mass diffusion, which was used alternately with turbulent dispersion force, was included for the inter diffusion of mass. The scale of the turbulent fluctuations was considered as an intermediate one, being larger than the control volumes used for computation and smaller than the scale of variation of the mean flow. In such case, the Reynolds averaging of the two-fluid equations was used on the condition that the void fraction could be decomposed into a mean and fluctuating part. The phase diffusion was taken as the ratio of liquid eddy viscosity and the turbulent Prandtl number for mass diffusion. Closure was also required for the virtual mass force, drag and lift forces. An unconventional method for defining the buoyancy force as extra momentum source terms for both the liquid phase (negative buoyancy) and the gas space (positive buoyancy) above the pool surface was used to avoid the use of a reference density for the calculation of the pressure drop for each phase which would lead to numerical inaccuracies. This approach provides more accurate bubble terminal velocities and the relative slip velocity between the phases. The addition of turbulent dispersion forces and lift gave the characteristic Gaussian shape of the plume spread and void distribution. The inclusion of energy-dispersion transport equations produced a broader Gaussian profile of the velocity field due to turbulent interactions between phases. Furthermore, the addition of turbulent viscosity due to the bubble-induced contribution coupled the plume to the ambient by, in effect, redistributing the liquid velocity field within the plume.

Modeling of stratification and mixing in large enclosed volumes, for computational purposes, considers two parts that naturally arise, these are the fluid contained within the buoyant jet and the fluid in the ambient volume (Christensen & Peterson, 2001). The Lagrangian approach by Christensen & Peterson (2001) was adopted to eliminate 'numerical diffusion' in computational applications. These 'false diffusions' are encountered in discretized equations on computationally coarse grids, and the Lagrangian formulation approach gives physically acceptable solutions at low computational cost. The 1-D Lagrangian formulation utilizes the 1-D Eulerian conservation equations for the incompressible multi-component ambient fluid using the Boussinesq approximation for an ambient fluid that is stratified by density. In such a

case, the conservation equations for the buoyant jet can be coupled to the ambient conservation equations due to fluid exchange between the two. In this 1-D formulation, the buoyant jet is assumed to occupy a small fraction of the total volume and is treated as quasi-steady with instantaneous inter-transport.

3.4 Condensation Heat Transfer and Regime Maps

3.4.1 *Steam Bubble Condensation with Non-Condensables in Subcooled Water*

Meier et al (1998) studied the steam-air injection problem in a downcomer. The liquid continuity and momentum equations were written as:

$$\frac{\partial \rho_f}{\partial t} + \nabla \cdot \rho_f \bar{u}_f = 0 \tag{3.68}$$

$$\rho_f \frac{D\bar{u}_f}{Dt} = -\nabla p_f + \mu_f \nabla^2 \bar{u}_f + \rho_f \bar{g} \tag{3.69}$$

where μ_f is also a variable dependent on temperature.

The conservation of energy is formulated from the thermal-energy equation neglecting dissipation and incorporating the caloric equation of state $\Delta h_f = c_{p,f} \Delta T_f$ and Fourier's law of heat conduction with an assumed conductivity λ_f; so a convection-conduction equation is written:

$$\rho_f c_{p,f} \frac{DT_f}{Dt} = \lambda_f \nabla^2 T_f \tag{3.70}$$

Dissipation for the liquid can be neglected, so the pressure term is left out of the energy equation. For the gas phase, the continuity equation is written

$$\frac{\partial \rho_g}{\partial t} + \nabla \cdot \rho_g \bar{u}_g = 0 \tag{3.71}$$

Accounting for the steam and air components, the mass conservation can be written in the form of species conservation by incorporating Fick's law of diffusion which is a typical approach to characterizing diffusive transport relating the bulk diffusion flux to an

apparent bulk diffusion coefficient for a species with a certain mass fraction. Using the steam mass fraction: $\omega_s = \rho_s / \rho_g$ where $\rho_g = \rho_s + \rho_a$ and the mass averaged velocity is $\vec{u}_g = \omega_s \vec{u}_s + (1-\omega_s)\vec{u}_a$. So for a binary gas mixture of steam and air and invoking Fick's law: $\rho_s(\vec{u}_s - \vec{u}_g) = -\rho_g D_{sa}(\nabla \omega_s)$, the steam continuity equation is written in the form:

$$\frac{\partial \omega_s \rho_g}{\partial t} + \nabla \cdot \rho_g \left(\omega_s \vec{u}_g - D_{sa} \nabla \omega_s \right) = 0 \tag{3.72}$$

The vapor momentum equation looks same as for the liquid:

$$\rho_g \frac{D\vec{u}_g}{Dt} = -\nabla p_g + \mu_g \nabla^2 \vec{u}_g + \rho_g \vec{g} \tag{3.73}$$

Using the caloric equation of state for an ideal mixture of perfect gases:

$$\Delta h_g = \left\{ c_{p,s}\omega_s + c_{p,a}(1-\omega_a) \right\} \Delta T_g \tag{3.74}$$

To determine how best to deal with the effect of the non-condensable gas on inhibiting steam condensation, it may be necessary to evaluate the importance of conduction compared with binary gas diffusion and the diffusion layer interface thickness.

A simplified energy balance energy balance for pure steam injection into water of the steam supply rate to the condensation rate can define a criterion for chugging (Liang et al, 1994) given by:

$$h_i A_i \Delta T_{sub} \geq \rho_s v_s A_j h_{fg} \tag{3.75}$$

where the interfacial heat transfer coefficient and the interfacial area are the most difficult quantities to determine. Condensation at the interface near the vent results in interfacial shear which determines the intensity of the interfacial eddies that are higher than that due to bulk liquid motion. A vertically-oriented vent can lead to a well defined bubble which is defined by a well rounded interface that collapses and swells during chugging. A transient conduction model can be used by assuming a warm layer of water forms periodically at the interface in which the water thermal layer thickness and water conductivity are needed to determine the conductance through the interface. If binary

diffusion transports heat from the gas mixture (for steam and air) to the interface, the latent heat the liquid receives by diffusion:

$$\dot{Q}_{lat} = h_{fg}\dot{m}_i = h_{fg}\frac{\rho_{g,i}D_{sa}\left|\nabla\omega_{s,i}\right|}{1-\omega_{s,i}} \tag{3.76}$$

The sensible heat by conduction is:

$$\dot{Q}_{sen} = k_g\left|\nabla T_{g,i}\right| \simeq k_g\frac{\left(T_{g,b}-T_{g,i}\right)}{\delta} \tag{3.70}$$

In the presence of non-condensables, the bubble surface temperature is not equal to the saturation temperature at the system pressure. It is possible for a steam-air bubble to have a stable equilibrium volume if during the process of condensation the partial pressure of the non-condensable increases simultaneously with the decreasing steam partial pressure until the gas mixture reaches the temperature of the bubble surface when the condensation ceases. According to Dalton's law of partial pressures, a steam - non-condensable mixture would occupy a bubble volume from the beginning of condensation to the termination and the ratio of final to initial volumes would be inversely proportional to the densities of the of both components

3.4.2 *Flow Regime Classification with Condensation*

Under various thermal-hydraulic conditions, the two-phase condensing buoyant jet (consisting of a mixture of steam and non-condensable gas) in a thermal suppression system exhibits a range of behavior as described by Kim & Song (2003). Physically based models and correlations are on-going pursuits to evaluate behavior related to heat transfer modes within suppression systems. Liang & Griffith (1994) and Pitts (1980) investigated flow regimes and flow regime transition criteria with the aim of developing models that predict external chugging. The external chugging regime (figure 3.1) occurs when the condensation capability of the subcooled pool far exceeds the steam injection flux, thereby resulting in a negative pressure on the gas-liquid interface, due to the surrounding pressure field, being formed on the steam plume intruding into the pool and

causing acceleration of water towards the steam plume. Depending on the periodicity of the steam injection flux and pool temperature, an oscillatory steam jet may occur at the steam vent exit characterizing the chugging regime. If the acceleration of the water load on the vent is very large, violent condensation shocks (Class et al, 1987) associated with bubble collapse may occur at the vent exits at very high pool subcooling and low steam mass flow rates.

Table 3.1 shows typical condensing regimes obtained under various experimental conditions by various authors, and Table 3.2 shows some phenomena of interest pursued by some authors and experimental conditions. Flow regime maps describing transitional behavior of the various condensing and jetting regimes, and flow rates, which are also mentioned in this table, have been dealt with in the studies of such authors as Chan & Lee (1982), Aya & Nariai (1991) and Liang & Griffith (1994). The regimes identified in Table 1 include: (1) chugging, and (2) transition from chugging (TC) to condensation oscillation ($G<200$ kg/ m^2-sec). These oscillations identified were classified as: condensation oscillation (CO), stable condensation (SC), interfacial condensation oscillation (ICO) and bubbling condensation oscillation (BCO) for a nozzle inner diameter of $d = 4.45$-10.85 mm and a nozzle length of $L = 0.12$ m. TC was found to occur when the frequency of the pressure oscillation was 20-80 Hz and subcooled water did not enter the nozzle but a cloud of tiny bubbles were formed near the nozzle exit, which is a precursor for a stable steam plume and which characterizes an atomizing regime where tip streaming becomes a feature. CO occurred with increase in G where the frequency was greater than 100Hz. BCO occurred at the same G as CO but at lower subcooling. For large G, SC was the case, and when subcooling was further reduced ICO occurred.

Lee & No (1998) identified criteria for boundaries and transitions between the regimes of chugging, subsonic jetting and steam cavity in gravity-driven injection experiments in a passive high-pressure system. These regimes were characterized in terms of Froud (Fr) and Jacob (Ja) numbers, where the Ja number gives a measure of the pool subcooling and the Fr number gives a measure of the force balance within the jet. They determined that this method of flow regime categorization fits data better with

different geometries than other dimensionless parameters. Their experiments involved conducting gravity-driven injection experiments of a passive high-pressure system in a small scale facility.

In the analysis of Liang and Griffith (1994), a transient conduction-diffusion model was developed to quantify how much non-condensable gas is required or pipe size alteration is needed to eliminate chugging. An *integral condensation distribution function* for calculating interfacial area and heat transfer coefficient was suggested for direct contact condensation (DCC) especially in the oscillatory jetting regime. This function was determined from measurements of the length of the condensing plume and the temperature of the water at several axial locations along the plume. For instance, in a subsonic jetting regime the product of the localized interfacial area and heat transfer coefficient can be related to the system operating specifications (like pool water temperature, stream injection flow rate and geometry) by an *integral condensation distribution function*. Their *transient conduction model* assumed a layer of warm water will form periodically at the interface as it collapses and swells.

The opposite extreme to the chugging regime is a fully developed turbulent jetting regime in which the condensing steam transfers sufficient momentum to the liquid ambient by way of the resulting fully condensed heated liquid jet. The resulting shallow submerged jet hits the far wall of the containment and in the process creates violent circulation patterns that eventually impinge on the free surface of the pool without necessarily being re-entrained into the jet. This fully developed jetting regime received some attention in the study of Gamble et al. (2001) for the cases of a single jet and three horizontally stacked jets. However, the multiventing of two-phase mixtures through vertically stacked rows of horizontal vents have not been completely addressed in the literature. Gamble et al. (2001), although making mention of the jetting velocity profiles of three simultaneous vertically stacked horizontally oriented vents, focused on the jet velocity profile case of three single-phase heated liquid jets. It was assumed in their study that condensation occurs over a short distance of 0.4 to 1.5 vent diameters from the vent exits, with the jets consisting of single-phase heated liquid beyond that range. This was

assumed for pure steam injection velocity of 150 m/s. The discharged steam jet was assumed to have a perfectly conical shape. However, a more reliable account of the typical shapes and penetration lengths of steam jets discharged from horizontal nozzles into subcooled water are well documented in the experiments of Song et al. (1998) and Chun et al. (1996).

Kukita & Namatame (1985) evaluated containment structural response due to hydrodynamic loads on the vent-to-vent desynchronization effects of LOCA (Loss of Coolant Accident) and steam condensation loads in the BWR pressure suppression pool. The direct-contact condensation of steam at the vent pipe outlets and the resulting oscillatory pressure loads on the pool boundary structure was their main focus. For an operating pressure of 7 MPa and postulated thermal-hydraulic conditions during a LOCA with initial vent pipe submergence in scaled tests representing the plant prototypical geometries, air was first blown down during the vent clearing period; this was followed by steam-air mixtures being discharged into the horizontal vents of their suppression pool. Prior to jet plume discharge into the subcooled pool, Kukita & Namatame (1985) identified that the most significant pool boundary loads was due to chugging which occurs when vent-flow steam mass flux is relatively low and is characterized by a minimum degree of penetration of gas-liquid interface into the vent pipe outlet. Depressurization in the vent pipe due to sudden increase in steam discharge can lead to high condensing rates and high frequency condensation oscillations prior to long term injection. Flow regimes within the SP can become complicated during simultaneous vent-to-vent discharge when the first row of submerged vents are cleared, steam-air mixtures are discharged into the suppression pool characterizing a well defined jet plume, followed by the middle and lower vents being cleared.

Various flow regimes of condensing steam injected into a subcooled pool of water have been categorized based on the criteria of the steam injection potential and the pool condensation potential or subcooling (Chan and Lee, 1982). The rationale for this basis is that the steam condensation behavior in the SP is dictated primarily by both the pool condensation potential and the steam injection flux (Chun et al., 1996). For the purpose

of mathematically modeling the vapor jet-plume and disintegration inside pools, quantitative information on the discharge at the vent exit over the accident transient is needed along with experimental assessment as a boundary condition for modeling the thermal-hydraulic response within the volume of interest. Figure 3.1 shows a summary of the condensation regimes reported by Chan and Lee (1982) classified according to injection flux and pool subcooling. In the case where high to pure noncondensable gas concentrations and high mass flux inputs occur, a bubbly plume consisting of a buoyant inner core and outer plume have been observed to drive the mixing in the surrounding fluid (Chen and Cardoso, 2000). In such a case, the driving mechanism may be the result of turbulent shear stresses.

As mentioned before, the other extreme case of gas injection into a subcooled pool is that of pure non-condensable gas injection which has the effect of enhancing circulation and mixing. Chen and Cardoso (2000) assessed the mechanism by which buoyant bubble plumes drive mixing in a surrounding liquid environment. In such a case, the bubble plume can be regarded as consisting of a buoyant inner core and an outer plume that imparts momentum to the surrounding liquid by turbulent shear stresses. In their experiments, bubbles generated by electrolysis rose into a density-stratified environment. The effectiveness of bubble-driven mixing was assessed by the efficiency of converting the input bubble energy into potential energy of the stratification. The mixing in the two-layer system consisted of turbulent entrainment of liquid in the upper layer by the plume liquid detrained at the interface, and the recirculation of environmental liquid in the lower layer through the plume. The modeling aspect of this study considered a rising plume in the lower layer of a step stratification of fresh water above a layer of salty water, of constant cross-section. The behavior of the plume of bubbles was considered as quasi-steady and neglected any variability in the entrainment coefficient. Using the Boussinesq approximation and a constant coefficient of entrainment, conservation equations of volume, momentum and buoyancy for the plume were formulated. The governing initial and boundary conditions that specify the volume flow rates, momentum and buoyancy were determined from the two uniform stratified layers and the plume source. A continuity condition for the rate of entrainment for the

upper layer at the interface was derived from assuming that kinetic energy of the plume at the interface is converted into potential energy of the lower layer. The model predicted mixing and efficiency of energy conversion in terms of the Richardson number where evolution of the density profile showed good agreement with experiments.

3.4.3 *Heat Transfer Correlations Developed for High Steam Mass Fluxes*

The efficiency of heat transfer in an enclosure also depends on the plume shape. Chun et al. (1996) defined three general idealized shapes of the pure steam jet plume in a subcooled pool of water. These idealized shapes; conical, ellipsoidal and divergent, are quantitatively inaccurate and were proposed based on experimental observation in an attempt to explain the local heat transfer mechanisms. The justification for defining these idealized shapes were based on experimental evidence, where the plume shape and length were found to depend on the injection diameter, injection orientation and pool subcooling, with combinations of these three well defined shapes occurring within specified ranges of steam mass flux. A correlation for pure steam injection is available (Chun et al, 1996) which predicts the length to diameter ratio of the plume as a function of the condensation driving potential and steam mass flux. This is given by:

$$\frac{l}{d} = 0.5923B^{-0.66}\left(\frac{G_o}{G_m}\right)^{0.3444} \tag{3.8}$$

where the driving potential for condensation is given by:

$$B = \frac{c_P\left(T_S - T_f\right)}{h_{fg}} \tag{3.9}$$

G represents the steam mass flux (see table 3.3). The justification for this correlation is based on the fact that the steam mass flux provides a measure of the driving force exerted on the liquid while the pool subcooling provides a measure of the condensation potential.

Chun et al. (1996) identified injection nozzle direction and nozzle submergence depth as being factors that characterize the shape of the jet plume, and obtained correlations of an average steam-water DCC heat transfer coefficient along with dimensionless steam plume lengths as described earlier. The average heat transfer coefficient of DCC for high steam mass velocities was found to be in the range 1.0~3.5 MW/m^2-°C, which shows some agreement with the maximum value of 2.4 $MWm^{-2}K^{-1}$ obtained by Jeje et al. (1990). Their correlation (Chun et al., 1996) does not, however, include the mean vapor transport modulus as this quantity cannot be directly measured in experiment. An R_T number, described by Kim and Song (2003), is similar to the Jacob number that describes pool subcooling and relates the energy potential of injected steam to condensing potential of the ambient subcooled water as:

$$R_T = \frac{c_P(T_g - T_f)G_f}{h_{fg}G_g} \tag{3.9}$$

For pure steam injection, the water mass flux G_f depends on the steam mass flux G_g and by momentum conservation, the R_T non-dimensional number becomes:

$$R_T = \frac{c_P(T_g - T_f)}{h_{fg}}\sqrt{\frac{A_g}{A_f}\frac{\rho_f}{\rho_g}} \tag{3.10}$$

However, this analysis assumes a constant mixing region diameter in order to apply momentum conservation to obtain the liquid jet velocity exiting from the condensing steam jet region and would be applicable to a stable mode of condensation. Although specific to stable steam injection, this same assumption was adopted in the study of Gamble et al. (2001) to obtain the average liquid jet velocity exiting the condensing region: $u'_{\text{liq. jet}} = u_{\text{steam}}\sqrt{\frac{\rho_{\text{steam}}}{\rho_{\text{liq. jet}}}}$. Such an assumption regards the steam penetration condensing region as perfectly conserving momentum and energy to the immediate condensed water. In actuality, this assumption may not necessarily be valid when the

non-condensable gas concentration increases and takes momentum with it, and the stable condensing regime is departed from.

Chun et al. (1996) also defined a heat transfer correlation which was independent of the plume length. The prediction by this correlation identifies the steam mass flow rate as the major controlling parameter in the direct contact condensation energy transport from the steam to the bulk liquid region by turbulent motion which originates at the vapor-liquid interface. This is given by:

$$h = 0.8012 c_p G_m B^{-0.6247} (\frac{l}{d})^{-1.0079} (\frac{G_o}{G_m})^{0.7185} \tag{3.11}$$

However, Chan and Lee (1982) identified the transport transfer processes in the vapor and liquid regions near the interface as the cause governing the complex behavior of the gas-liquid interface.

A model for the critical flow of the steam condensing region through a submerged sparger was the focus of Kang et al. (2003). In their experiment, saturated steam at high pressure (100 bar) was initially discharged through 4 levels of 16 circumferentially distributed horizontally sparger holes of diameter D = 1 cm and a single bottom hole of 2.5 cm diameter into subcooled water at 20 C at atmospheric pressure in a quench tank. The steam penetration length was reported as 5.3D at submergence depths within the range of approximately 260D to 230D in the horizontal holes. A penetration length of 13 cm was reported for the vertical downward oriented hole. The width of the jet at the end of the penetration length was 1.2D for the horizontal holes. Note the difference in the steam penetration length of 0.5D to 1.4D assumed by Gamble et al. (2001) for a single submerged jet.

For pure steam injection into a pool of water, the mass flow rate of condensed water as well as entrained water at the condensation boundary is determined from the conservation of mass, momentum and energy equations, being respectively:

$$\{\dot{m}_e + \dot{m}_{entrain} = \dot{m}_{cond}\} \tag{3.12}$$

$$\{(P_e - P_\infty)A_e + (\rho_e V_e^2 A_e) = P_{cond} A_{cond} + (\rho_{cond} V_{cond}^2 A_{cond})\} \tag{3.13}$$

and

$$\{(\dot{m}_e h_e) + (\dot{m}_{entrain} h_{entrain}) = (\dot{m}_{cond} h_{cond})\} \tag{3.14}$$

Kung et al. (2003) defined the steam penetration length as:

$$\frac{x_c}{r_0} = 20.57 \left(\frac{G_0}{G_s}\right)^{0.713} \left(\frac{\rho_\infty}{\rho_s}\right)^{-0.384} B^{-0.801} \tag{3.15}$$

with

$$B = \frac{(h_f - h_\infty)}{(h_s - h_f)} \tag{3.16}$$

and $\dot{m}$ being the critical mass flow rate

This correlation (equation 3.15) is comparable to that of Chun et al. (1996) and Song at al. (1998). Table 3.3 shows a comparison of some models and correlations developed by researchers as well as their agreement with experimental data.

3.5 Summary

Current nuclear reactor safety computer codes like RELAP5 do not consider condensation phenomena due to a submerged jet within the pool and at the surface, but incorporate a McAdams natural convection correlation model, when flow is stratified, to model heat transfer between bulk liquid and a saturated interface (Schumway, 1997). The correlation relates the Nusselt number and Rayleigh number as: $Nu = 0.27Ra^{0.25}$. In the SP, the actual heat transfer is expected to be higher than natural convection phenomena because there is mixing and condensation phenomena introduced by high energy, high momentum and high buoyancy steam jet-plumes. Various experiments that address the condensation phenomena due to turbulent mixing at a free-surface and natural

convection are available (Brown et al., 1990, Sonin et al., 1986, & Thomas, 1979) but cannot be applied to accurately predict the thermal response of direct contact condensation of discharged jet-plumes to an initially quiescent volume of water. It is an ongoing effort to derive correlations that encompass the physical processes that are component specific which could be used in reactor safety codes. Only an overview of the various models and mechanistic approaches to jet-plume modeling that are available in the literature have been discussed here, and it can be seen that the requirements for modeling the physical processes related to direct contact condensation are still lacking as this can be very complex and challenging.

Table 3.1: Condensation regimes of steam-air injection into subcooled water.

Authors (year)	Injection diameter (mm)	Exit orientation	Inlet air mass fraction	Steam/air mass flux or flow rates	Water subcooling (°C)	Regimes identified
Lee, No (1998)	15	Downward gravity driven High system pressure 4 bar	0-0.5	20-40 20-80 40-80 (kg $m^{-2}s^{-1}$)	30-55 60-80 30-60	Chugging Steam cavity Subsonic jetting Transition regimes
Chun, Kim, Park (1996)	4.45-10.85 10.85	Horizontal Vertical, nozzle L=0.12m	0	300-550 200-300 (kg $m^{-2}s^{-1}$)	17-82 16-81	*SC-IOC CO-BCO
Liang, Griffith (1994)	19	Upward rectangular channel	0-0.6 0.6-1.0	0.01~0.02 Ma 0.03~0.05 Ma	50-100	Chugging, bubbling, subsonic jet, sonic jet, Transition regimes
Aya, Nariai (1991)	9-38	Downward vent pipe	0	40 kg $m^{-2}s^{-1}$	0-100	Chugging, CO, bubbling
Jeje, Asante, Ross (1990)	5	Upward	0	< 1.6 g s^{-1} 1.6-1.9 g s^{-1} 1.9-6.1 g s^{-1}	16.5	Discrete bubbling Transition to unstable jet Nearly axisymmetric jet
Chan, Lee (1982)	51	Downward vent pipe in hexagonal pool	0	1-175 (kg $m^{-2}s^{-1}$)	40-90	Chugging Oscillatory bubble, Ellipsoidal oscillatory bubble, Ellipsoidal jet, Oscillatory jet cone
Class, Raft, Meyder (1987)	600	Vertically downwards at different elevation in 30° sector PSS**	0	20 kg $m^{-2}s^{-1}$	25	Violent condensation shocks, (with steam reservoir pressure of 117 kPa) Steam pocket with bottle neck
Kukita, Namatame (1985)	74-240	Multivent vertically downward in 20° sector	< 0.01	Rupture disk (steam pressure of 7 MPa used) (< 25 kg $m^{-2}s^{-1}$)	19-54	Chugging desynchronization, High frequency oscillation, Bubble collapse,
Brucker, Sparrow (1977)	1.6	Vertical upward injection	0	15-22 cm/s bubble rise velocity.	15-100	Bubbling, Bubble oscillation, Bubble collapse, at elevated pressures (10.3-62.1 bar)

*SC = stable condensation, CO = condensation oscillation, IOC = interfacial oscillation condensation, BCO = bubbling condensation oscillation.
**PSS = pressure-suppression system

Table 3.2: Experimental parameters and phenomena considered by various researchers.

Authors (year)	Nondimensional jet submergence H	Submergence aspect ratio A	Pool aspect ratio P	Enclosure aspect ratio E	Fluids	Phenomena
Kang et al (2003)	260 to 230	1.15 to 1.3	~ 0.875	0.75	Steam-water quench tank condensation	Thermal mixing
Christensen & Peterson (2001)	10.5	0.6	0.475	< 0.475	Immersed heater in water pool	Thermal mixing under stably stratified conditions
Peterson et al (1991)	50 to 67	18 to 10.8	3.2 to 2.8	2.5	Salt/water mixture	Transient thermal stratification
Baines & Turner (1969)	40 to 80	115 to 85	2.8 to 1	1, 1.5, 2	Fresh/salt water	Criteria for overturning, Turbulent buoyant convection

$$H = \frac{jet\ depth}{initial\ plume\ width},\ A = \frac{pool\ width}{jet\ depth},\ P = \frac{pool\ width}{initial\ water\ height},\ E = \frac{pool\ width}{enclosure\ height}$$

Table 3.3: Comparison of models and empirical correlations proposed by various researchers.

Author	Flow regime analyzed	Empirical correlation method with experiment	†Correlation equations or model	Agreement of correlation with data
Chun, Kim, Park	Steam plume	Balance of mass flow rate, transport modulus and condensation potential.	Dimensionless plume length: $\frac{l}{d} = 0.5923B^{-0.66}(\frac{G_o}{G_m})^{0.3444}$	within ± 20%
		Least square method for average heat transfer coefficient	Average heat transfer coefficient: $h = 0.8012c_p G_m B^{-0.6247}(\frac{l}{d})^{-1.0079}(\frac{G_o}{G_m})^{0.7185}$	within ± 15 %
Liang, Griffith	Chugging criterion	Transient conduction model	$-0.06\,\mathrm{Re}_f^{s0.5}\,\mathrm{Pr}^{0.5}\,\mathrm{Ja}^{-1} \le 1.0$	Within 65 %
			For steam-air mixture: $0.06\left(1+\frac{k_w}{k_d^a}\frac{\delta_a}{\delta_w}\right)\mathrm{Re}_f^{s0.5}\,\mathrm{Pr}^{0.5}\,\mathrm{Ja}^{-1} \le 1.0$	Within 30 %
	Jetting criterion	Two-layer turbulent eddy transfer model	$0.035\left(\frac{\rho_f}{\rho_s}\right)^{1/4}\mathrm{Re}_f^{s1/4}\,\mathrm{Pr}^{1/2}\,N\mathrm{Bo}^{2/3}\,\mathrm{Ja}^{-0.7} \ge 1.0$	Within 15 %
Lee, No	Steam cavity transition	Correlations for regime boundaries	Fr + 17Ja – 2367 = 0	*Absolute error:* |0.05 Fr| + |0.17 Ja|
	Chugging to subsonic jet transition		Fr = 212	*Absolute error:* 0.05 Fr
Pitts	Chugging	Control volume model, modified integral form of momentum equation	Axial velocity & displacement found by time integration of: $F_z + g\rho_L AL = \rho_L AL\frac{\partial V_z}{\partial t}$, when infinitesimal gas layer, $\varepsilon \to 0$ $F_z = \begin{cases}(P_G - P_L)A - \left(\lambda\frac{L}{D}+K_0\right)\frac{\rho_L V_z^2}{2}, & V_z > 0\\ (P_G - P_L)A - \left(\lambda\frac{L}{D}+K_i\right)\frac{\rho_L V_z^2}{2}, & V_z < 0\end{cases}$ Radial accelerations are integrated to obtain radial bubble boundary velocities and position	Predicted fundamental periods within 5 - 16 % of experimental data. Low frequency chugging predicted with quasi-steady state analysis, large computational time steps used

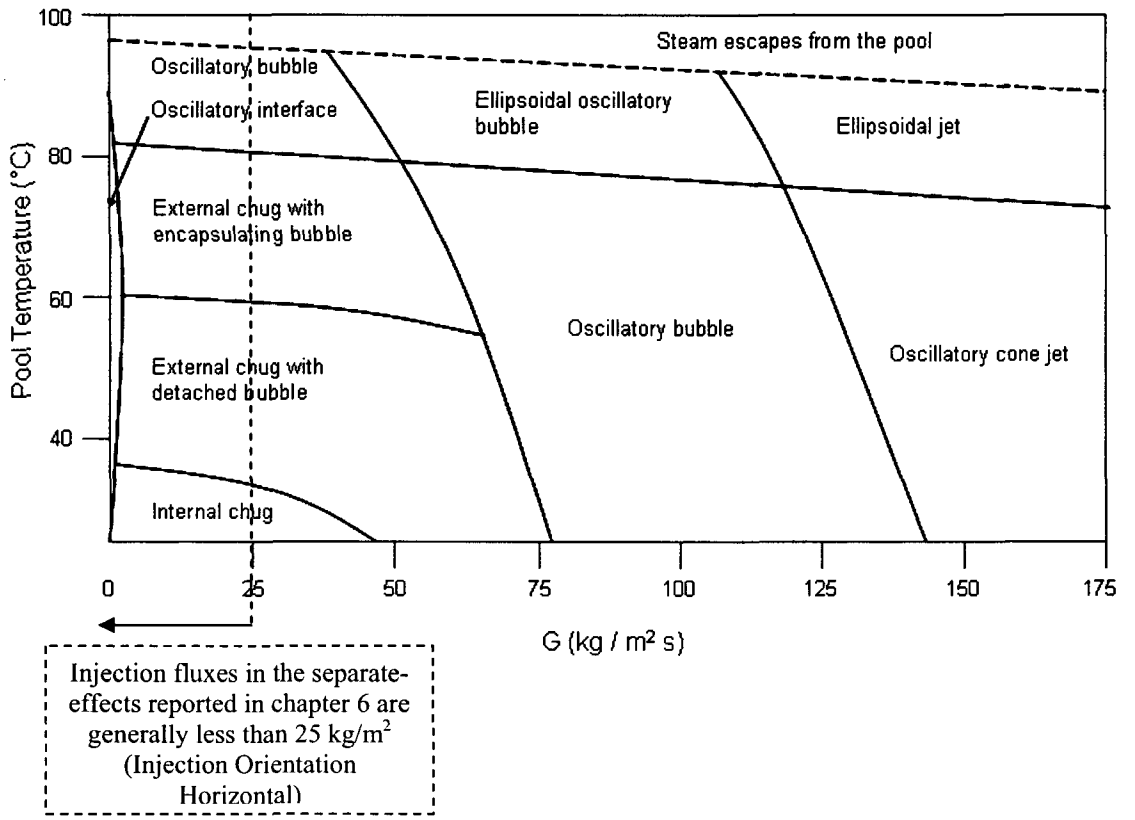

Figure 3.1 Steam condensation regime map for vertical orientation and atmospheric pressure conditions [ref. Chan and Lee (1982)]

3.6 References

Al-Najem, N.M., & El-Refaee, M.M. (1997). A numerical study for the prediction of turbulent mixing factor in thermal storage tanks. [Electronic version]. *Applied Thermal Engineering*, 17(2), 1173-1181.

Aya, I., & Nariai, H. (1991). Evaluation of heat-transfer coefficient at direct-contact condensation of cold water and steam. [Electronic version]. *Nuclear Engineering and Design*, 131(1), 17-24.

Baines, W. D., & Turner, J. S. (1969). Turbulent buoyant convection from a source in a confined space. *Journal of Fluid Mechanics*. 37(1), 51-80.

Bandurski, T., Huggenberger, M., Dreier, J., Aubert, C., Putz, F., Gamble, R. E., & Yadigaroglu, G. (2001). Influence of the distribution of noncondensibles on passive containment condenser performance in PANDA. *Nuclear Engineering and Design*, 204, 285-298.

Baskaya, S., Gilchrist, A., & Fraser, S. M. (1997). The radial spread and axial decay of temperature in turbulent condensing jets. [Electronic version]. *International Communications in Heat and Mass Transfer*, 24(4), 465-474.

Bombarbelli, F. A., Buscaglia, G. C., Rehmann, C. R., & Garcia, M. H. (2001). Scaling procedures for aeration bubble plumes. Retrieved March, 12, 2004, from http://cabmec1.cnea.gov.ar/~gustavo/last_pps/scaling/

Bosanquet, C. H., Horn, G. & Thring, M. W. (1961). The effect of density differences on the path of jets. *Proceedings of the Royal Society Series A Mathematical and Physical Sciences*, 1314(263), 340-352.

Brown, S. J., Khoo, B. C., & Sonin, A. A. (1990). Rate correlation for condensation of pure vapor on turbulent, subcooled liquid. *International Journal of Heat and Mass Transfer*, 33(9), 2001-2018.

Brown, W. G. (1962). Natural convection through rectangular openings in partitions – 2. *International Journal of Heat and Mass Transfer*, 5, 869-878.

Brucker, G. G., & Sparrow, E. M. (1977). Direct contact condensation of steam bubbles in water at high pressure. *International Journal of Heat and Mass Transfer*. 20(4), 371-381.

Chan, C.K., & Lee, C.K.B. (1982). A regime map for direct contact condensation. *International Journal of Multiphase Flow*, 8(1), 11-20.

Chen, M. H., & Cardoso, S. S. S. (2000). The mixing of liquids by a plume of low-Reynolds number bubbles. [Electronic version]. *Chemical Engineering Science*, 55, 2585-2594.

Choi, K.Y., Chung, H.J., & No, H.C. (2002). Direct-contact condensation heat transfer model in RELAP5/MOD3.2 with/without noncondensable gases for horizontally stratified flow. [Electronic version]. *Nuclear Engineering and Design*, 211(2-3), 139-151.

Christensen, J., & Peterson, P.F. (2001). A one-dimensional Lagrangian model for large-volume mixing. [Electronic version]. *Nuclear Engineering and Design*, 204, 229-320.

Chun, M.–H., Kim, Y.–S., & Park, J.-W. (1996). An investigation of direct condensation of steam jet in subcooled water. *International Communications in Heat Mass Transfer*, 23(7), 947-958.

Class, G., Raff, S., & Meyder, R. (1987). The mechanism of violent condensation shocks. *International Journal of Multiphase Flow*, 13(1), 33-46.

Collier, J. G., & Thome, J. R. (1994). Convective boiling and condensation. New York: Oxford University Press Inc.

Cruz, J. M. S., Hammond, G. P., & Reis, A. J. P. S. (2002). Thermal performance of a trapezoidal-shaped solar collector/energy store. [Electronic version]. *Applied Energy*, 73, 195-212.

Fan, L. –N., & Brooks, N. H. (1967). Turbulent buoyant jets into stratified or flowing ambient fluids. *California Institute of Technology, Report Number KH-R-15.*

Finkelstein, Y., & Tamir, T. (1976). Interfacial heat transfer coefficients of various vapors in direct contact condensation. *The Chemical Engineering Journal.* 12(3), 199-209.

Gamble, R.E., Nguyen, T. T., Shiralkar, B. S., Peterson, P. F., Greif, R., & Tabata, H. (2001). Pressure suppression pool mixing in passive advanced BWR plants. [Electronic version]. *Nuclear Engineering and Design*, 204, 321-336.

Gulawani; S. S., Joshi, J. B., Shah, M. S., RamaPrasad, C. S., & Shukla, D. S. (2006). CFD analysis of flow pattern and heat transfer in direct contact steam condensation. *Chemical Engineering Science.* 61, 5204-5220.

Han, J. T., Bessette, D. E, & Shotkin, L. M. (Oct. 25-17, 1993). NRC confirmatory testing program for SBWR. (NUREG/CP-0132). In *Transactions of the Twenty-First Water Reactor Safety Information Meeting*, Bethesda, Maryland.

Huh, B. G., Euh, D. J., Yun, B. J., Song, C. H., & Chung, C. H. (May 4-7, 2003). Development of particle interaction model of large bubbles in the interfacial area transport equation. *In Proceedings of ICAPP*, Cordoba, Spain.

Hunt, G. R., Cooper, P., & Linden, P. F. (2001). Thermal stratification produced by plumes and jets in enclosed spaces. [Electronic version]. *Building and Environment*, 36, 871-882.

Hussain, N. A., & Narang, B. S. (1984). Simplified analysis of air-bubble plumes in moderately stratified environments. *Journal of Heat Transfer*, 106, 543-551.

Ishii, M. (May 30- June 4, 2004). Two-fluid model based on interfacial area transport equation. In *5th International Conference on Multiphase Flow*, Yokohama, Japan.

Ishii, M., & NguyenLe, Q. (1999). Three Dimensional Analysis of Turbulent Steam Jets in Enclosed Structures: A CFD Approach. (ANL/RA/CP-98801) Illinois: Argonne National Laboratory.

Ishii, M., Revankar, S.T., Leonardi, T., Dowlati, R., Bertodano, M. L., Babelli, I., et al. (1998). The three–level scaling approach with application to the Purdue University Multi-Dimensional Integral Test Assembly (PUMA). [Electronic version]. *Nuclear Engineering and Design*, 186, 177-211.

Janicot, A., & Bestion, D. (1993). Condensation modelling for ECC injection. *Nuclear Engineering and Design*. 145, 37-45

Jeje, A., Asante, B., & Ross, B. (1990). Steam bubbling regimes and direct contact condensation heat transfer in highly subcooled water. *Chemical Engineering Science*, 45(3), 639-650.

Jirka, G. H., & Harleman, D. R. F. (1979). Stability and mixing of a vertical plane buoyant jet in confined depth. *Journal of Fluid Mechanics*, 94(2), 275-304.

Kelly, J. M. (March 17-20, 1997). Constitutive Model Development Needs for Reactor Safety Thermal-Hydraulic Codes. (NUREG/CR-0160). In *The OECD/CSNI, Specialist Meeting on Advanced Instrumentation and Measurement Techniques*, Santa Barbara, California.

Kang, H. S., Kim, Y. S., Park, C. K., Cho, S., & Song, C. H. (July 6-10, 2003). Numerical study on preliminary thermal mixing test in B&C loop facility. In *Proceedings of FEDSM2003: 4th ASME/JSME Joint Fluids Engineering Conference*, Honolulu, Hawaii.

Kim, Y.–S., & Song, C.–H. (2003). Overall review of steam jet condensation in a next generation reactor water pool. In *Proceedings of International Mechanical*

Engineering Congress & Exposition. Washington, D.C. The American Society of Mechanical Engineers.

Kim, H.Y., Koyama, S., & Matsumoto, W. (2001). Flow pattern and flow characteristics for counter-current two-phase flow in a vertical round tube with wire-coil inserts. [Electronic version]. *International Journal of Multiphase Flow*, 27, 2063-2081.

Kolev, N. (2002). Multiphase flow dynamics 2, mechanical and thermal interactions. New York: Springer-Verlag.

Kuhn, S.Z., Bernardis, R.D., Lee, C.H., & Peterson, P.F. (2001). Density stratification from buoyancy-driven exchange flow through horizontal partitions in a liquid tank. [Electronic version]. *Nuclear Engineering and Design*, 204, 337-345.

Kukita, Y., & Namatame, K. (1985). The vent-to-vent desynchronization effects on LOCA steam condensation loads in BWR pressure suppression pool. *Nuclear Engineering and Design*, 85(2), 141-150.

Lee, S. I., & No, H. C. (1998). Gravity-driven injection experiments and direct-contact condensation regime maps for passive high-pressure injection system. *Nuclear Engineering and Design*, 183, 213-234.

Legendre, D., Borée, J., & Magnaudet, J. (1998). Thermal and dynamic evolution if a spherical bubble moving steadily in a superheated or subcooled liquid. *Physics of Fluids*. 10(8), 1256-1272.

Liang, K.-S., & Griffith, P. (1994). Experimental and analytical study of direct contact condensation of steam in water. *Nuclear Engineering and Design,* 143(3), 425-435.

Longmire, E. K., Norman, T. L., & Gefroh, D. L. (2001). Dynamics of pinch-off in liquid/liquid jets with surface tension. *International Journal of Multiphase Flow*, 27, 1735-1752.

McDougall, T. J., (1978). Bubble plumes in stratified environments. *Journal of Fluid Mechanics*, 85(4), 655-672.

Meier, M. (1999). Numerical and experimental study of large steam-air bubbles injected in a water pool. *Ph.D. Thesis*. Swiss Federal Institute of Technology Zurich.

Meier, M., Andreani, M., & Yadigaroglu, G. (Nov. 15-20, 1998). Experimental study of large steam-air bubbles condensing in a suppression pool. In *IMECE/ASME*, Anaheim.

Milgram, J. H. (1983). Mean flow in round bubble plumes. *Journal of Fluid Mechanics*, 133, 345-376

Moalem, D., Sideman, S., Orell, A., & Hetsroni, G. (1973). Direct contact heat transfer with change of phase: condensation of a bubble train. *International Journal of Heat and Mass Transfer*, 16(12), 2305-2319

Morton, B. R. (1959). Forced Plumes. *Journal of Fluid Mechanics*, 5(1), 151-163.

Murase, M., Kataoka, Y., & Fujii, T. (1993). Evaporation and condensation heat transfer with noncondensable gas present. *Nuclear Engineering and Design*, 141, 135-143.

Murata, A., Hihara, E., & Saito, T. (1992). Prediction of heat transfer by direct contact condensation at a steam-subcooled water interface. *International Journal of Heat and Mass Transfer*, 35(1), 101-109.

Norman, T. L., Park, H. –S., Revankar, S. T., Ishii, M. & Kelly, J. M. (Nov. 5-10, 2006). Thermal stratification and mixing in an open water pool by submerged mixtures of steam and air. *In Proceedings of the IMECE 2006*, Chicago IL.

NguyenLe, Q., & Ishii, M. (1998). A Theoretical and Numerical Investigation of Turbulent Steam Jets in BWR Steam Blowdown. (ANL/RA/CP-96739) Illinois: Argonne National Laboratory.

Peterson, P.F., Schrock, V.E., & Greif R. (1998). Scaling for integral simulation of mixing in large, stratified volumes. [Electronic version]. *Nuclear Engineering and Design,* 186, 213-224.

Peterson, P. F., Rao, I. J., & Schrock, V. E. (1991). Transient thermal stratification in pools with shallow buoyant jets. *Nuclear Reactor Thermal-Hydraulics, HTD-Vol. 190*. The American Society of Mechanical Engineers.

Pitts, J. H. (1980). Steam chugging in a boiling water reactor pressure-suppression system. *International Journal of Multiphase Flow*. 6(4), 329-344.

Rao, A. S. (2003). *Revision 1 to NEDO-33084, "ESBWR Design Description."* Retrieved November, 12, 2003, from http://www.nrc.gov/

Robinson, J. L. (1967). A note on the instability of an infinite fluid heated from below. *Journal of Fluid Mechanics*, 29(3), 461-464.

Sang, I. L., & No, H. C. (1998). Gravity-driven injection experiments and direct-contact condensation regime map for passive high-pressure injection system. *Nuclear Engineering and Design*. 183(3), 213-234.

Sato, Y., Sadatomi, M., & Sekoguchi, K. (1981). Momentum and heat transfer in two-phase bubble flow – I. *International Journal of Multiphase Flow*. 7, 167-177.

Shumway, R.W. (1997). Condensation Enhancement on a Pool Surface Caused by a Submerged Liquid Jet. (INEL/CON--97-00261; CONF-971130--1) Idaho: Idaho National Engineering and Environmental Laboratory.

Smith, B. L. (1998). On the modelling of bubble plumes in a liquid pool. Applied Mathematical Modelling. 22, 773-797.

Snider, D.M., & Andrews, M.J. (1994). Rayleigh-Taylor and shear driven mixing with an unstable thermal stratification. [Electronic version]. *Physics of Fluids,* 6(10), 3324-3334.

Socolofsky, S. A., Crounse, B. C., & Adams, E. E. (2002). Multi-phase plumes in uniform, stratified, and flowing environments. In *Environmental Fluid Mechanics – Theories and Applications.*

Sonin, A. A., Shimko, M. A., & Chun, J.–H. (1986). Vapor condensation onto a turbulent liquid – I. The steady condensation rate as a function of liquid-side turbulence. *International Journal of Heat and Mass Transfer*, 29(9), 1319-1332.

Song, C.–H., Cho, S., Kim, H.–Y., Bae, Y.–Y., & Chung, M. K. (1998). Characterization of Direct Contact Condensation of Steam Jets Discharging into a Subcooled Water. In *International Atomic Energy Agency Technical Committee Meeting.* Thomas Heck Paul Scherrer Institut (PSI), Villigen, Switzerland.

Straatman, A.G. (1999). On the development of a computational method for modeling turbulent mixing in sharply stratified flows. *International Journal of Heat and Fluid Flow*, 20, 385-394.

Taitel, Y., & Tamir A. (1969). Condensation in the presence of a noncondensable gas in direct contact. *International Journal of Heat and Mass Transfer*, 12(9), 1157-1169.

Tamir, A., & Taitel, Y. (1970). Direct contact condensation with a multi-component mixture of non condensable gases. *International Journal of Heat and Mass Transfer*. 13, 1501-1503.

Theofanous, T. G., Houze, R. N., & Brumfield, L. K. (1976). Turbulent mass transfer at free, gas-liquid interfaces, with applications to open-channel, bubble and jet flows. *International Journal of Heat and Mass Transfer*, 19, 613-624.

Thomas, R. M. (1979). Condensation of steam on water in turbulent motion. *International Journal of Multiphase Flow*, 5, 1-15.

Wachs, D. M., Reyes Jr., J. M., & Davis, L. R. (1998). A Study of Thermal Stratification in the Cold Legs During the Subcooled Blowdown Phase of a Loss of Coolant Accident in the OSU APEX Thermal Hydraulic Testing Facility. (ANL/ED/CP-97607) Illinois: Argonne National Laboratory.

Xu, Y. (2004). Direct contact condensation with and without noncondensable gas in a water pool. *Ph.D. Thesis*. Purdue University.

4. EXPERIMENTAL FACILITY DESIGN AND TEST CONDITIONS

4.1 Scaling Philosophy

Justifiable scaling methods must be adhered to in model systems when simulating reactor accident scenarios primarily to preserve the thermal-hydraulic behavior or phenomenon of the individual reactor components of the prototype for the specific accidental scenario under consideration. Performing experiments in an actual prototypic reactor can become impractical because of cost limitations and safety reasons, in which case we rely on scaled down model separate-effects test facilities. In such an instance, a scaling philosophy is needed to relate phenomena observed in the model to that expected in the actual prototype. The design of the separate effects suppression pool discussed in this chapter first scales the power to volume ratio of the ESBWR suppression pool to simulate the mass and energy inventories over a broad range of prototypic conditions. One limitation of this facility is that the system pressure is approximately constant at pool atmospheric pressure. As a consequence of this limitation, pressure scaling and two-phase similarity criteria are adopted since the system pressure in the model facility cannot be altered to match that in the prototype. A comprehensive scaling analysis addresses the conservation principles and constitutive relations in both the top-down and bottom-up approach (Ishii et al, 1996). For a single component of the reactor under consideration, the integral response function scaling or first level scaling is not necessary. However, the control volume and boundary flow scaling which comprise the second level, as well as the local phenomena scaling which comprise the third level scaling are important and are considered for this application. An idealized pool geometry is preferred since complex test sections are difficult to fabricate, which means that scaling distortions are encountered and are considered when relating the actual engineering design with the ideal scientific design.

Reduced system pressure model tests introduce large uncertainties due to difficulties in matching all the dimensionless groups in the prototype under changing

system pressure conditions (Kocamustafaogullari and Ishii, 1987). For condensation phenomena scaling in the suppression pool, the parameters of primary importance are the pool condensation potential and the vapor latent heat energy given respectively by

$$\dot{Q}_c = a_i h_{cond}\left(T_{sat} - T_{pool}\right) \tag{4.1}$$

$$E_g = \rho_g Q_g h_{fg} \tag{4.2}$$

For proper scaling of pool condensation phenomena, the following ratio of prototype to model must be satisfied:

$$\left(\frac{\dot{Q}_c}{E_g}\right)_R = 1 \tag{4.3}$$

The most difficult parameters to measure are the total interfacial area concentration a_i and the local condensation heat transfer coefficient h_{cond}. If T_{sat}, T_{pool}, ρ_g and h_{fg} are also scaled then it is required that

$$\left(\frac{\dot{Q}_c}{E_g}\right)_R = \frac{a_{iR}}{Q_{gR}} = 1 \tag{4.4}$$

where $Q_{gR} = \left(a_{in}u_{in}\right)_R = a_{oR}\sqrt{l_{oR}}$ since from two-phase similarity requirements $\left(u_o\right)_R = \left(l_o\right)_R^{1/2}$ (Ishii et al, 1996), which therefore requires $a_{iR} = a_{oR}\sqrt{l_{oR}}$. For the prototype system, the interfacial area is $a_{ip} \approx \left(n\pi D_J l_J\right)_p$ and for the model pool it is $a_{im} \approx \left(n\pi D_J l_J\right)_m$. This requires:

$$\left(\frac{\dot{Q}_c}{E_g}\right)_R = \frac{a_{iR}}{Q_{gR}} = D_{JR}\frac{l_{JR}}{Q_{gR}} = 1 \tag{4.5}$$

Besides inside the actual pool volume, condensation in the SP also occurs in the intermediate gas flow rates in the vertical channel of the SP where a vertical gas jet forms before being expelled to the pool via the horizontal venting system. For this case the

relative condensation rate is scaled similarly as in equation 4.5, which is given by equation 4.6.

$$\left(\frac{\dot{Q}_c}{E_g}\right)_R = \frac{a_{iR}}{Q_{gR}} = \frac{l_{TR} D_{JR}}{Q_{gR}} \tag{4.6}$$

Here l_T is the depth of water and D_J is the jet diameter and the subscript R denotes the ratio of model to prototype. Disintegration to smaller bubbles is expected to occur when condensation rate is insufficiently high or due to the presence of noncondensable gas.

4.2 Design Basis

The design basis for the separate-effects test section in relation to the geometry of the ESBWR suppression pool and scaling strategy are discussed in this section. Here the power to volume ratio of the ESBWR suppression pool is considered for simulating the mass and energy inventories over a range of prototypic conditions.

4.2.1 *Prototype Containment*

The ESBWR containment, consisting of a wetwell and drywell, is a cylindrical steel-lined reinforced concrete structure integrated within the reactor building. Its design pressure and temperature are respectively 414 kPa and 171 °C. Figure 1.1 shows the cross-section of the ESBWR containment envelope, and the heat removal systems with associated piping. The suppression pool wetwell is a large volume of water that functions as a major but finite heat sink, and since its elevation is higher than the top of the RPV core, it also acts as reactor make up inventory via the equalization lines (total of four) in severe accidents where the reactor core may lose coolant become uncovered. The gas space in the WW can communicate with the gas volume in the GDCS (gravity driven cooling system) in this ESBWR design. The WW gas space serves as a non-condensable gas reservoir for receiving the DW non-condensable gas volume during a LOCA blowdown.

The top view of the RPV in relation to the SP is shown in Figure 4.1 along with a scaled idealized trapezoidal cross-section of a sector of the pool. The prototype venting system consists of 10 circumferentially arranged vertical vents at azimuth angles of 36° relative to each other. Each vertical vent branches into 3 horizontal vents stacked vertically as shown in Figure 4.2 for a total of 30 horizontal vents, each with 10 vents being diametrically positioned from the center of the RPV and stacked at 3 different elevations from the bottom of the pool (Figure 4.3). Over-pressurization of the WW relative to the DW is prevented via vacuum breaker check valves which open whenever the WW cover gas pressure exceeds that of the DW by 3.45 kPa.

4.2.2 *Scientific Design of a Scaled Suppression Pool for the ESBWR*

The top view of the RPV relative to the SP is shown in Figure 4.1. The height, volume and area are scaled as indicated by equations 4.7 to 4.9. The volume scale was first chosen in regard to the power capacity of the PUMA RPV heater so as to attain a broad range of test conditions. A reduced height facility causes the time for certain phenomena to be accelerated, where the time is given by the square root of the length scale. In this way, for instance, the time taken for vertical stratification degradation to occur in the model would be $1/\sqrt{4.5}$ of the time it would take in the prototype. This reduces the time by approximately 2.12 for conducting a separate-effects experiment.

$$l_R = \frac{1}{4.5} \tag{4.7}$$

$$V_R = a_R l_R = \frac{1}{400} \tag{4.8}$$

$$a_R = \frac{1}{88.9} \tag{4.9}$$

This gives a power scale of

$$q_R = a_R \sqrt{l_R} = \frac{1}{188.6} \tag{4.10}$$

1/10th of the SP pool section (36° sector) is being considered and since the prototype volume is already scaled 400 by volume (equation 4.8), this means that 1/4000

of the actual prototype volume is being used and therefore the power to volume ratio is high with the maximum output of the PUMA RPV being 400 kW. This gives the extra flexibility of studying high flow rate cases at a reduced pressure condition.

Table 4.1 Scaled suppression pool dimensions

SCALING of ESBWR SP	1/10 th of Model SP
Initial Water Volume (m^3)	0.9025
Initial Gas Space (m^3)	1.1260
Height (m)	2.7222
Pool Surface Area (m^2)	0.7451
Top Vent Elevation (m)	0.7778
Middle Vent Elevation (m)	0.4733
Bottom Vent Elevation (m)	0.1689
Water Level (m)	1.2111

The dimensions of the scaled pool geometry based on the ESBWR are given in Table 4.1. Since $1/10^{th}$ of the pool is considered, an idealized trapezoidal cross-section is being used as depicted in Figure 4.3 which is easier to fabricate. The arrangement of the RPV radial spacing with respect to suppression pool, the SP vertical and horizontal vent distribution and wall thicknesses within the prototype were taken into account in this design. The elevations of the 3 horizontal vents and the initial pool water level were scaled from the vent submergence in the prototype using the height ratio 1/4.5 (equation 4.7). However, a 4th vent is included based on the length scale which is determined from the area ratio of $1/\sqrt{88.9}$. The 4th vent is placed at a submerged depth of 1/9.4 of the top-most (prototypic) vent from the initial water level to enable the study of the venting effect when preserving the same scale in height and radius representing a 1:1 scaled arrangement.

4.3 Hardware Design

4.3.1 *Pool Engineering Design*

Since 1/10th of the pool is considered, an idealized trapezoidal cross-section was designed for. Figures 4.3 to 4.6 show the details of the pool design which was fabricated from ¼ inch thick stainless steel plates. Viewing windows, made from clear ½ inch thick polycarbonate sheets, were designed and fitted to the pool for the purpose of illumination, flow visualization, and LDA implementation. Flanges for the view holes (see Appendix B) were custom made and were sliced from 6-inch diameter schedule 160 pipes. The windows were mounted with bolts and gaskets made from ultra-strength neoprene rubber prevented leakage during tests. These view ports are placed on the sides of the pool at alternating levels so that each injection vent can be illuminated from one of the off parallel sides at the same elevation to the vent and at distances away from the vent as shown in Figure B.2 (Appendix B) to track the horizontal path of the effluent. Viewing ports are also placed on the far wall facing the vents to view the behavior of the effluent as it exits from the vents. Additional illumination ports are placed to coincide with the initial water line elevation to visualize any pool swelling due to the submerged flux and also to act as a sight glass to measure water level increases in condensation experiments. Penetrations (¼ inch diameter) also provide a means to add additional transparent tubing to measure the water level changes in experiments where the water level may increase beyond the view of the top-most windows. These penetrations (which can be seen in the photographs of Figures 4.3 and 4.5) can also be utilized for inserting additional instrumentation such as thermocouples if needed. Half-couplings (¼ inch) are welded over the penetrations for screwing plugs to make the walls water tight when the penetrations are not being used.

Fill and drain lines are also placed as shown in the layout plan (Figure 4.5). The fill and drain lines are shut on or off via 1-inch stainless steel valves and although they are not placed directly to the base of the pool, but slightly higher, any excess water remaining in the pool after draining can be removed by a siphon since the pool is resting

on an elevated base. The support base is designed so that the test-section can be fastened to the base with high-tension stainless steel cables and can be anchored securely to the ground. In addition the wheels of the base can be locked during tests, and unlocked whenever the test-section needs to be repositioned. Figures 4.3 and 4.5 are photographs taken of the model pool resting on the custom-made support base. The test section, showing the vent and window arrangement of the model pool resting on the support base, is also shown.

4.3.2 *Piping for Routing Steam from PUMA RPV*

The steam supply to the model suppression pool is routed from the PUMA RPV. The steam is tapped from the SRV-A (safety relief valve A) line and flanged valves are used to shut-off steam supply to the PUMA SP via the SRV line (V-SRV-05) and route the steam to the model pool (V-SRV-06) as shown in Figures 4.4, 4.5 and 4.6. Figures 4.4 and 4.5 show the details of this tee-ing of the SRV-A line, and Figure 4.6 shows the isometrics of the pipeline arrangement from the PUMA facility to outside of the facility. See also Figures B.3 to B.6 in Appendix B. The SRV-A line is a 2 inch stainless steel pipe. The RPV has a height of 6126.3 mm, an inner diameter of 600 mm, an area of 0.2827 m^2, and a total volume of 1.7 m^3. It is composed of lower plenum, core plate, core, shroud, chimney, downcomer, and separator and dryer assemblies. The core has 38 electrical heater rods. There are 6, 12 and 20 heater rods in inner, middle and outer rings, respectively. Their maximum rod powers are 11.0, 13.5, and 9.0 kW respectively, and their operating powers are 5.5, 6.6 and 4.4 kW, respectively. The details of the piping arrangement to the model pool are shown in Figures B.3 to B.6 (in Appendix B). These show the detailed drawings of the supply lines indicated in Figure 4.6. The injection arrangement to the new model suppression pool is shown in Figure B.6 for the 2-inch and 3-inch venting cases respectively.

The air is supplied from an air supply tank through 2-inch schedule 40 pipe on which the mass flow controller is installed. Figure B.1 shows a schematic of the piping arrangement and Figure 4.6 shows the isometric of the piping.

The k-loss is calculated from the point where the pressure tap measures the steam pressure before it gets mixed with air at the tee (see Appendix B). The frictional pressure drop along the piping can then be estimated for the steam-air mixture from:

$$\Delta P = \frac{1}{2} k_m \rho_m v_m^2 \tag{4.11}$$

The k-losses for gradual reducers and enlargements were obtained from the Crane handbook. This is given by equation 4.12, and k-losses are summarized in Table 4.2

$$k_2 = \frac{2.6\left(\sin\frac{\theta}{2}\right)\left(1-\beta^2\right)^2}{\beta^4} \tag{4.12}$$

Table 4.2 K-loss in steam-air piping system from mixing tee to vent exit

Pipe size	Type	k
2"	Tee branch	1.14
2"	elbow	0.29
2"	ball valve	0.04
2"	Tee through	0.38
2"	elbow	0.29
2"	elbow	0.29
2"	flexible coupling	0.00
2"	elbow	0.29
2"	ball valve	0.04
2"	elbow	0.29
2"	Tee branch	1.14
2" to 3"	gradual enlargement	1.16
Total	k_m	5.32

All pipe lines were well insulated. The test section was also insulated. Proper insulation was necessary in order to inhibit any significant condensation within the piping. Heat losses were taken into account by checking the energy balance.

4.4 Defining a Test Matrix

The following is a discussion on defining a test matrix for the top vent opening in the model SP separate-effects test using the PUMA SP separate-effects test as a complementary counterpart (Woo, 2005). This discussion addresses not only local phenomena scaling but also global scaling and scaling in terms of non-dimensional mass, momentum and energy.

4.4.1 *Preserving Pool Condensation Potential in Scaled Facility*

In pool condensation it is widely accepted that the steam condensation potential is driven by the pool subcooling (Chan and Lee, 1982, and Lee and No, 1998 for example) where the subcooling is defined as the pool bulk temperature relative to the saturation temperature, $T_{sat}(p)$, of the incoming vapor mixture at the system pressure in the region of the vent exit. However, if the incoming vapor is not at saturation condition and is superheated, then the driving force for condensation is the temperature difference between the injected vapor (T_{in}) and the pool bulk temperature. If the vapor is superheated, the amount of heat transfer may be different compared with that of a saturated vapor. If, for example, the vapor is pure steam and is superheated by an amount 25 °C, then the gas enthalpy is 2726.54 kJ/kg at atmospheric pressure (101.325 kPa) compared with that of the saturated steam of 2675.53 kJ/kg at the same atmospheric pressure and 100 °C. The latent heat of saturated steam is 2256.47 kJ/kg, and the additional sensible heat due to superheated steam is given by equation 4.13

$$c_{p,g}\Delta T_{sup} = 1.511 \text{ kJ/(kg °C)} \times 25 \text{ °C} = 37.78 \text{ kJ/kg} \qquad (4.13)$$

This is only 1.67 % of the saturated steam latent heat, and the latent heat of saturated steam at atmospheric pressure is itself already large. Therefore the amount of heat that is transferred from the steam vapor to the liquid by the superheated steam is not very

significant compared with the saturated steam. Furthermore, when air is mixed with the superheated steam, this brings the value of $c_{p,g}$ even lower and this decreases the additional sensible heat. In addition, any impurities that may be present in the water that is heated to supply the steam can act to reduce the boiling point.

One can therefore distinguish the pool subcooling, given by equation 4.14a from the temperature difference of the injected vapor mixture and the pool bulk temperature, given by equation 4.14b which is the actual driving potential for condensation:

$$\Delta T_{sub} = T_{sat}(p) - T_w \tag{4.14a}$$

$$\Delta T = T_{in} - T_w \tag{4.14b}$$

If one is instead interested in the effective driving potential for condensation, and the effect of the gas superheat is negligible as demonstrated in the previous calculation, the temperature difference given by equation 4.15 is considered a measure of this driving potential for condensation instead of ΔT in equation 5.3b (Meier et al, 1998).

$$\text{Condensation driving potential} = T_{sat}(p_s) - T_w \tag{4.15}$$

It can, as a result, be justified that a preferred measure of the condensation driving potential is the partial pressure difference between the injected vapor and the saturation pressure of the liquid at the pool temperature (from discussions with J. M. Kelly of the U.S. NRC) given by equation 4.16.

$$\Delta p_s = p_s - p_{sat}(T_w) \tag{4.16}$$

These pressure quantities are measurable and can be determined from pitot-static probe measurements by traversing the probe along the vapor jet protruding into the water pool.

Kim and Song (2003) discussed the characteristics of a steam jet plume in subcooled water, citing the work by Fukuda and Saitoh (1982), and explained that the thermodynamic process of the vapor flow from the injection nozzle to the liquid pool can

be assumed as an isotropic process. If the water vapor injected from a nozzle, even though it may be a little superheated, can be assumed to be saturated, and so the steam pressure varies little through the isentropic process, which is higher than the saturation pressure at the same temperature. In the superheated condition of the steam, a portion of the steam condenses and the steam quality decreases which can result in fog forming inside the steam bubble which provides another mechanism for condensation. The injection configuration, whether a divergent nozzle or a vent, also can have the effect of altering the steam quality and is worth investigating as an experimental parameter. In the chugging regime the vapor pressure in the vapor plume varies a lot.

4.4.2 *Steam-Air Mixture Injection*

The steam partial pressure at the vent exit is obtained from the following analysis. The non-condensable mass concentration is given by equation 4.17.

$$x = \frac{\dot{m}_a}{\dot{m}_a + \dot{m}_s} \tag{4.17}$$

where

$$\dot{m}_a = \rho_a v_a A \tag{4.18a}$$

and

$$\dot{m}_s = \rho_s v_s A \tag{4.18b}$$

So the non-condensable mass fraction is given by

$$x = \frac{\rho_a}{\rho_a + \rho_s \frac{v_s}{v_a}} \tag{4.19}$$

Then

$$\rho_a = \rho_s \frac{v_s}{v_a}\left(\frac{x}{1-x}\right) \tag{4.20}$$

Now from,

$$\frac{1}{\rho_m} = \frac{V}{\dot{m}_a + m_s} = \frac{V}{\left[1 + \frac{v_s}{v_a}\left(\frac{x}{1-x}\right)\right]\rho_s V} \tag{4.21a}$$

The following result is obtained:

$$\rho_m = \rho_s\left[1+\frac{v_s}{v_a}\left(\frac{x}{1-x}\right)\right] \tag{4.21b}$$

But

$$\rho_s = \frac{\rho_a v_a}{v_s}\left(\frac{1-x}{x}\right) \tag{4.22a}$$

Therefore,

$$P_s = \rho_s R_s T_m = \frac{\rho_a v_a}{v_s}\left(\frac{1-x}{x}\right)R_s T_m \tag{4.22b}$$

Where

$$\rho_a = \frac{P_a}{R_a T_m} \tag{4.23}$$

Assuming the steam and air are well mixed and are in thermal equilibrium, $T_m = T_s = T_a$

From Dalton's law of partial pressures:

$$P_m = P_a + P_s \tag{4.24}$$

This gives

$$P_s = (P_m - P_s)\frac{v_a}{v_s}\left(\frac{1-x}{x}\right)\frac{R_s}{R_a} \tag{4.25a}$$

And so

$$\frac{v_s}{v_a} = \frac{P_m - P_s}{P_s}\frac{R_s}{R_a}\left(\frac{1-x}{x}\right) \tag{4.25b}$$

Finally

$$\rho_m = \rho_s\left[1+\frac{P_m - P_s}{P_s}\frac{R_s}{R_a}\right] \tag{4.26}$$

Steam volume fraction is also given by

$$\frac{\dot{m}_s/\rho_s}{(\dot{m}_s/\rho_s)+(\dot{m}_a/\rho_a)} = \frac{P_s}{P_m} \tag{4.27}$$

Substituting $\rho_a = \frac{P_a}{R_a T_m} = \frac{P_m - P_s}{R_a T_m}$ and $T_m = \frac{P_s v_s}{R_s \rho_a v_a}\left(\frac{x}{x-1}\right) = \frac{P_s}{R_s}\frac{1}{\rho_s}$ from the ideal gas law

This gives

$$P_s = \frac{-2P_m \pm \sqrt{(2P_m)^2 - 4P_m^2\left[\left(\frac{R_a}{R_s}\right)\left(\frac{x}{1-x}\right)-1\right]}}{2\left[\left(\frac{R_a}{R_s}\right)\left(\frac{x}{1-x}\right)-1\right]} \tag{4.28}$$

Taking the first root gives the steam partial pressure required at the vent inlet to the model SP:

$$P_m = P_s\left[\sqrt{\frac{R_a}{R_s}\left(\frac{x}{1-x}\right)}+1\right] \tag{4.29}$$

Where R_a = 286.9 J/kgK, and R_s = 455 J/kgK

The presence of non-condensable gas inhibits the steam condensation process by two ways. The first kind of condensation resistance occurs on the water side of the injected steam-air mixture jet-plume. Locally, the water becomes heated and its cooling capability diminishes, this acts to retard the water conduction. The second kind of condensation resistance occurs inside the jet-plume in which gas diffusion resistance of steam through a medium of air takes place and also thermal conduction resistance in the gas takes place. Liang and Griffith (1994) proposed a transient conduction-diffusion model given by equations 4.30.

$$0.06\left(1+\frac{k_w}{k_d^a}\frac{Ja}{2}\frac{\rho_s}{\rho_a}\sqrt{\frac{D_{sa}}{\alpha_w}}x_n\right)^{0.5} \mathrm{Re}_f^{s\,0.5}\,\mathrm{Pr}^{0.5}\,Ja^{-1} \le 1 \quad \text{Chugging} \tag{4.30a}$$

$$0.06\left(1+\frac{k_w}{k_d^a}\frac{Ja}{2}\frac{\rho_s}{\rho_a}\sqrt{\frac{D_{sa}}{\alpha_w}}x_n\right)^{0.5} \mathrm{Re}_f^{s\,0.5}\,\mathrm{Pr}^{0.5}\,Ja^{-1} > 1 \quad \text{Bubbling and Jetting} \tag{4.30b}$$

The terms in equations 4.30 are given in Table 4.3

Table 4.3: Terms defined in equations 4.30a and 4.30b

ρ_a	Air density (kg/m^3)
ρ_f	Liquid density (kg/m^3)
k_w	Water conductivity (W/(m.K))
k_d^a	Diffusion-equilibrium thermal conductivity of air (W/(m.K))
α_w	Water conduction $k_w/\rho_w c_p$ (m^2/s)
*D_{sa}	Mass diffusion coefficient of steam through a medium of air (m^2/s)
Re_f^s	Steam-liquid Reynolds number, $v_s D_j/\nu_f$ (inertial / viscous)
Pr	Prandtl number of the liquid, $\mu c_p/\kappa$ (kinematic viscosity / thermal diffusivity)
Ja	Jacob number, $\rho_f c_p \Delta T/\rho_s h_{fg}$
ρ_s	Vapor density (kg/m^3)

*A correlation for binary mass diffusion coefficient of steam through air is found in MELCOR Material Properties Package Reference Manual as $D_{sa} = 4.7931\times10^{-5}\left[\frac{T^{1.9}}{P}\right]$ for T in units of °K and P in units of Pa

The equations 4.30a and 4.30b are transition criteria for the onset of external chugging from the bubbling or jetting regime. D_{sa} is the binary mass diffusion coefficient of steam through air. A correlation for this is given by $D_{sa} = 4.7931\times10^{-5}\left[\frac{T^{1.9}}{P}\right]$ (found in MELCOR Material Properties Package Reference Manual).

Liquid conduction is given by $\alpha_w = k_w / \rho_f c_{p,f}$ and gas conduction by $\alpha_g = k_g / \rho_g c_{p,g}$, where heat is transferred from the gas to the interface by both conduction and binary diffusion transport. So for atmospheric pressure with a small hydrostatic head and for a saturation temperature (i.e. 105.5 kPa and 100 °C), the following are obtained as shown in Table 4.4.

Table 4.4: Water conduction, liquid conduction and binary diffusion at atmospheric conditions

α_w (m²/s) .10⁻⁶	α_g (m²/s) .10⁻⁶	D_{sa} (m²/s) .10⁻⁶
0.197	19.493	35.347

This shows that the gas conduction and the binary diffusion transport are of the same order of magnitude. This is indicated by the Lewis number $Le = \alpha_g / D_{sa} = 0.55$. We could therefore assume that both gas conduction and binary diffusion transport from the gas to the liquid are important. However, in cases of complete steam condensation the gas conduction is diminished and the Lewis number increases. So, by this assumption latent heat transfer by binary diffusion would be much larger than sensible heat transfer from conduction in the gas.

Since the PUMA facility has prototypic pressure, the density ratio $\rho_R = 1$ is satisfied. However, the drywell/wetwell venting depends on a pressure difference between the drywell and suppression pool where this pressure difference is related to the height scale: $(P_{DW} - P_{SP})_R = l_{oR} = 1/4$. Furthermore, for a reduced pressure facility like the model SP, the model SP cover gas pressure cannot be varied (P = 105.5 kPa) since the pool is open to atmosphere. Similarity criteria (Kocamustafaogullari & Ishii, 1987) require that certain conditions such as the subcooling and phase change numbers, as described by equations 4.31 and 4.32, be satisfied.

$$N_{pch} = \frac{\Delta\rho.\dot{Q}}{\rho_g.\dot{m}_{in}.\Delta h_{fg}} = \frac{\Delta\rho/\dot{m}_{in}}{\rho_g/\Gamma_g} \tag{4.31}$$

$$N_{sub} = \frac{\Delta\rho}{\rho_m}\frac{\Delta h_{sub}}{\Delta h_{fg}} = \frac{\Delta\rho.c_{p_f}.\Delta T_{sub}}{\rho_m.\Delta h_{fg}} = \left.\frac{\Delta\rho}{\rho_g}\right|_{P_{in}} \frac{c_{p_f}\left(T_{sat}\big|_{P_{in}} - T_{f_{in}}\right)}{\Delta h_{fg}\big|_{P_{in}}} \tag{4.32}$$

Physically, the phase change number is the scale for the amount of heating and vapor flow generated by phase change which relates the inlet mass flux to the condensation

mass flux. The subcooling number ratio is the scale for the cooling in a condensation section relative to the saturation condition or the ratio of the pool subcooling to the inlet latent heat. The steam density is a function of pressure and the similarity criteria $(N_{pch})_R$ =1 and $(N_{sub})_R$=1 needs be satisfied from prototype to model since the system pressure is different. In addition, from a phenomenological point of view, local phenomena scaling would require that the Jacob number (equation 4.33) be preserved. This has a similar form to the subcooling number.

$$Ja = \frac{\rho_f c_{p,f}\left(T_m - T_w\right)}{\rho_m h_{fg}} \tag{4.33}$$

An R_T number, described by Kim & Song (2003), is similar to the Jacob number that describes pool subcooling and relates the energy potential of injected steam to condensing potential of the ambient subcooled water as: $R_T = \frac{c_P\left(T_g - T_f\right)G_f}{h_{fg}G_g}$. For pure steam injection, the water mass flux G_f depends on the steam mass flux G_g and by momentum conservation, the R_T non-dimensional number becomes: $R_T = \frac{c_P\left(T_g - T_f\right)}{h_{fg}}\sqrt{\frac{A_g}{A_f}\frac{\rho_f}{\rho_g}}$. However, this analysis assumes a constant mixing region diameter in order to apply momentum conservation to obtain the liquid jet velocity exiting from the condensing steam jet region and would be applicable to a stable mode of condensation. In addition G_f is dependent on G_g which is not a controllable parameter but depends on the former. Although specific to stable steam injection, the same assumption was adopted in the study of Gamble et al. (2001) to obtain the average liquid jet velocity exiting the condensing region: $u_{\text{liq. jet}} = u_{\text{steam}}\sqrt{\frac{\rho_{\text{steam}}}{\rho_{\text{liq. jet}}}}$. Such an assumption regards the steam penetration condensing region as perfectly conserving momentum and energy to the immediate condensed water. In actuality, this assumption may not necessarily be valid when the non-condensable gas concentration takes momentum with it and introduces a buoyancy flux, and a stable condensing regime is departed from. For a steam-air mixture injected into a subcooled pool of water, the condensation potential or

driving force for condensation is the temperature difference between the seam-air injected mixture and the bulk pool temperature. Since the system pressure is scaled we therefore should preserve the subcooling number or Jacob number which contains steam properties that are pressure dependent.

4.4.3 *Preserving Injection Fluxes in Scaled Facility*

There are correlations (for example Chun et al., 1996) that identify the steam mass flow rate as the major controlling parameter in the direct contact condensation energy transport from the steam to the bulk liquid region by turbulent motion which originates at the vapor-liquid interface. The pool mixing is also dependent on the amount of momentum and buoyancy carried by the jet-plume, and for the purpose of local scaling it is desirable to preserve the Froude number, given by equation 4.34, which preserves the momentum and buoyancy balance of the jet-plume.

$$Fr = \frac{\rho_f v_m^2}{(\rho_f - \rho_m) g D} \tag{4.34}$$

This Froude number is a measure of the amount of inertia carried by the jet-plume, and in preserving this inertia from the PUMA SP separate-effects cases it is desirable to preserve the mass flux, which also preserves the enthalpy flux. Similarly, the Richardson number characterizes the transition from inertial to buoyant behavior and is the inverse of the densimetric Froude number, as indicated by equation 4.35.

$$Ri = \frac{(\rho_f - \rho_m) g D_j}{\rho_f v_m^2} \tag{4.35}$$

Also, since the condensation reduces the amount of vapor injected, it is desirable to preserve the total volumetric flux.

All the above quantities are property-dependent, only the steam-liquid Reynolds number contains velocity and length parameters that can be easily adjusted in the experiment. This is given by equation 4.36 (Ishii et al, 1998).

$$\left(\mathrm{Re}_f^s\right)_R^{0.5} \alpha \left(\upsilon_s D_j\right)_R^{0.5} = \left(\frac{1}{20}\right)^{0.5} \tag{4.36}$$

However, since the steam-fluid Reynolds number is given by $\left(\mathrm{Re}_f^s\right)_R^{0.5} = \upsilon_s D_j / \nu_f$, for a reduced system pressure facility, equation 4.36 needs to be adjusted to include the fluid viscosity which is pressure dependent. Equation 4.36 assumes the system pressure of prototype and model is preserved. Since $\left(\dot{V}_s\right)_R$ α $\left(\mathrm{Re}_f^s\right)_R$, the injected steam volumetric flow rate is a fluid-dynamic parameter that can be used to compare the volume reduction in a prototype to that of an experimental model of the injected jet-plume after condensation takes place inside the pool. In the proposed model SP tests, the steam is directly supplied from the RPV and is routed via the SRV-A line to the model SP. The pool volume and exit flow area are already scaled from the ESBWR prototype and is given by V_R = 1/400 and $(a_{in})_R$ = 1/88.9 respectively for a height ratio of $(l_{in})_R$ = 1/(4.5) (see equations 4.7 to 4.9). Since 1/10 th of the pool is considered for one stack of 3 horizontal vents only 1/10 th of the volume is considered. Scaling the mass flux also scales the enthalpy in the prototype. Table 4.5 and Figure 4.7 indicate prototypic conditions determined from RELAP5 simulation of a BDLB (bottom drain line break) scenario. Tables 4.6 and 4.7 show respectively the scaled mass and volumetric flow rates from Table 4.5. They are scaled from conditions obtained from RELAP5 simulations of a BDLB (bottom line drain break) accident (see Table 4.5 and Figure 4.7). Tables 4.8 and 4.9 show respectively the comparison in preserving ΔT and the subcooling number for the saturated steam and the pool initial temperature for the pressure conditions in the PUMA and model cases.

4.4.4 *Preserving Time Scales of Phenomena*

In inertia-dominated jets in which buoyancy is much smaller than inertia, four time constants are identified (Ishii et al., 1998 & Peterson et al., 1998). These are

(1) The jet transport time given by equation 4.37. This is also known as the jet residence time.

$$\tau_{Jt} = \frac{n_J \frac{\pi}{4} D_J^2 H}{\dot{V}} \tag{4.37}$$

(2) The jet entrainment time constant given by equation 4.38, where α is Taylor's jet entrainment constant. The inverse of this is the characteristic frequency for energy transport.

$$\tau_{Je} = \frac{n_J \frac{\pi}{4} D_J^3}{4\sqrt{2}\alpha\dot{V}} \tag{4.38}$$

(3) The transport time of the surrounding fluid given by equation 4.39, and

$$\tau_{st} = \frac{V}{\dot{V}} \tag{4.39}$$

(4) The entrainment time of the surrounding fluid given by equation 4.40.

$$\tau_{se} = \frac{V}{\alpha 4\sqrt{2}\frac{H}{D_j}\dot{V}} = \frac{\tau_{st}\tau_{Je}}{\tau_{Jt}} \tag{4.40}$$

Two independent dimensionless groups (equations 4.41 and 4.42) are formed by the first three equations (4.37, 4.38 and 4.39). Equation 4.41 is the change in mass, momentum, energy or species during the fluid's residence time in the volume.

$$\Pi_J = \frac{\tau_{Jt}}{\tau_{Je}} = 4\sqrt{2}\alpha \frac{H}{D_j} \tag{4.41}$$

Also equation 4.42 is the time ratio that controls mixing behavior in a stratified fluid, where H is the vent submergence.

$$\Pi_s = \frac{\tau_{Jt}}{\tau_{st}} = \frac{n_J \frac{\pi}{4} D_J^2 H}{V} = n_J \frac{D_J^2}{D^2} \tag{4.42}$$

The ratio $\Pi_{s\ \text{experiment}} / \Pi_{s\ \text{prototype}} = 1$, implies that $n_{JR} D_{JR}^2 = D_R^2 = A_R$ which is already satisfied by the area ratio scaling. Preservation of Π_J imposes $\left(\frac{D_J}{H}\right)_R = 1$. To satisfy the time scale for mixing in stratified volumes, this ratio needs to be satisfied. For the PUMA SP separate-effects test, and equivalent diameter is given by $D_J = 0.121268$ m, and for the model SP $D_J = 0.0779$ m (3.068 inches). Another vent diameter that will be used in the model is given by $D_J = 0.0508$ m (2 inches). For the mixing time scales to be the same in the PUMA SP tests and the model SP tests it requires that the top-most vent in the new model SP be utilized. The height is scaled linearly according to the area ratio. For PUMA SP horizontal vent submergence of $H = 0.446$ m requires H to be 0.28 m in the model SP. In this case, the top-most vent (based on a linear scale) in the model SP at an elevation of 1.004 m from the bottom of the SP is utilized and the water level is set to 1.284 m.

4.4.5 *Separate-Effects Test Conditions*

These separate-effects pool tests are intended to be a counterpart to the PUMA suppression pool separate-effects experiments. In the PUMA SP experimental program, the suppression pool is distorted to a cylindrical volume and integrated within the other reactor components for the purpose of performing integral tests under prototypic high pressure conditions whereas the prototype SBWR suppression pool geometry is annular in shape. In the PUMA SP, the eight vertical vent modules connecting the drywell to the suppression pool (as is the case in the SBWR prototype), a single vent line scaled by the

total prototype vent flow area and boundary flow scaling criteria are used. Each vent cross-section in the PUMA SP is a rectangular slit since the height and area scales are not in the 1:1 linear ratio. The single vertical vent line is centered in the suppression pool with eight of the slit vent openings on the perimeter of that submerged line simulating the eight SBWR prototype vent openings into the SP. In the current model SP, the vent cross-section is maintained as circular which is the same in the ESBWR prototype; however, it is scaled by flow area. $1/10^{th}$ of the ESBWR prototype volume is considered and then scaled by volume to a trapezoidal cross-section which is idealized from a sector of an annulus. In the initial blowdown, PUMA integral tests start at around 1 MPa, however, in the present model suppression pool, since the power to volume ratio in the model SP is much higher, we have the flexibility to set the boundary conditions to those of the actual prototype when conditions inside the prototype suppression pool are at atmospheric and prior to 1 MPa conditions in the prototype.

In counterpart PUMA SP test conditions (Woo, 2005), three vents at the top elevation are open. The test matrices and conditions were obtained from RELAP5 simulation of a BDLB accident as shown in Figure 4.7. For the model pool, the actual scaling ratios are as follows: $H_R = \frac{1}{4.5}$, $V_R = \frac{1}{400}$, $A_R = \frac{1}{88.9}$, Ideally, the height and volume ratios are the same as equations 4.7 and 4.8. However the actual area ratio for the vent for the 3-inch vent case is $A_R = \frac{1}{80.7}$ because of the use of commercial piping. See Tables 4.5 to 4.9 and Figure 4.7 for the test conditions.

Table 4.5 Prototypic conditions determined from RELAP5 simulation of SBWR-600

DW Pressure (kPa)	V V NC	steam mass flow rate (kg/s)	total mass flow rate (kg/s)	air mass flow rate (kg/s)	steam density (kg/m^3)	air density (kg/m^3)
261.9	0.007	18.6	18.73	0.13	1.453	2.269
244.7	0.013	9.92	10.05	0.13	1.364	2.132
247.1	0.012	5.25	5.314	0.064	1.376	2.152
247.9	0.02	8.88	9.06	0.18	1.380	2.158
237.3	0.179	14.67	17.87	3.2	1.325	2.073
230.3	0.279	21.41	29.7	8.29	1.288	2.017

Table 4.6 Mass flow rate scaled conditions

model Pressure (kPa)	V V NC	steam mass flow rate (kg/s)	total mass flow rate (kg/s)	air mass flow rate (kg/s)	steam density (kg/m^3)	air density (kg/m^3)
105	0.0069	0.0123	0.0124	0.00009	0.6179	0.9778
105	0.0129	0.0066	0.0067	0.00009	0.6179	0.9778
105	0.0120	0.0035	0.0035	0.00004	0.6179	0.9778
105	0.0199	0.0059	0.0060	0.00012	0.6179	0.9778
105	0.1791	0.0097	0.0118	0.00212	0.6179	0.9778
105	0.2791	0.0142	0.0197	0.00550	0.6179	0.9778

Table 4.7 Volumetric flow rate scaled conditions

model Pressure (kPa)	V V NC	steam mass flow rate (kg/s)	total mass flow rate (kg/s)	air mass flow rate (kg/s)	steam density (kg/m^3)	air density (kg/m^3)
105	0.0070	0.0052	0.0053	0.00004	0.6179	0.9778
105	0.0131	0.0030	0.0030	0.00004	0.6179	0.9778
105	0.0122	0.0016	0.0016	0.00002	0.6179	0.9778
105	0.0201	0.0026	0.0027	0.00005	0.6179	0.9778
105	0.1808	0.0045	0.0055	0.00100	0.6179	0.9778
105	0.4419	0.0068	0.0122	0.00539	0.6179	0.9778

Table 4.8 Calculation of model pool temperature based on temperature difference

PUMA Pool T (deg-C)	230 kPa PUMA steam sat (deg-C)	ΔT (deg-C)	105 kPa model steam sat (deg-C)	model Pool T (deg-C)
40	128.95	88.95	101	12.05
50	128.95	78.95	101	22.05
60	128.95	68.95	101	32.05

Table 4.9 Calculation of model pool temperature based on subcooling number

PUMA Pool T (deg-C)	230 kPa PUMA steam sat (deg-C)	N-sub	105 kPa model steam sat (deg-C)	model Pool T (deg-C)
40	128.95	110.85	101	62
50	128.95	96.96	101	67
60	128.95	83.1	101	72

A number of tests have been performed to obtain temperature profiles in the pool for related thermal-hydraulic parameters using 2- and 3-inch vent pipes. Sixteen tests were performed with 2-inch diameter vent pipes and 53 tests with 3-inch diameter vent pipes. The experimental test matrix and experimental conditions for 2-inch and 3-inch vent pipe injection cases are summarized in Table 4.10 and 4.11 respectively.

Table 4.10: Test matrix and experimental conditions for 2-inch vent pipe injection

Test ID	Steam flow rate (g/s)	Air flow rate (g/s)	Initial pool temperature (°C)	Pool Status (Stratified or Mixed)
T2-09	17.0	1.207	37.6	Mixed
T2-10	23.6	0.302	18.7	Mixed
T2-11	24.2	0.302	35.8	Mixed
T2-12	23.6	7.499	24.3	Mixed
T2-13	23.4	7.499	39.1	Mixed
T2-14	24.4	7.499	55.7	Mixed
T2-15	23.4	0.302	52.4	Mixed
T2-16	42.9	0.504	21.5	Mixed
T2-17	43.3	0.526	55.9	Mixed
T2-18	13.8	0.202	20.8	Mixed
T2-19	13.4	5.000	25.2	Mixed
T2-20	12.9	5.000	33.0	Mixed
T2-21	13.9	0.202	32.7	Mixed
T2-22	13.8	0.202	42.7	Mixed
T2-23	42.8	5.549	29.1	Mixed
T2-24	42.5	5.549	59.8	Mixed
T2-25	14.8	5.000	39.5	Mixed

Table 4.11: Test matrix and experimental conditions for 3-inch vent pipe injection

Test ID	Steam flow rate (g/s)	Air flow rate (g/s)	Initial pool temperature (°C)	Pool Status (Stratified or Mixed)
T3-01	12.1	0.000	22.7	M
T3-02	12.4	0.089	26.8	S
T3-03	12.2	0.089	40.4	S
T3-04	12.1	0.456	47.3	M
T3-05	12.2	0.456	57.6	M
T3-06	12.8	0.180	35.9	M
T3-07	13.3	0.135	29.8	M
T3-08	10.9	0.108	29.3	M
T3-09	12.3	0.000	44.6	M
T3-10	12.2	0.000	48.9	M
T3-11	12.0	0.089	48.3	M
T3-12	13.5	0.089	57.7	M
*T3-13	13.6	0.065	21.1	MST
T3-14	19.1	0.086	22.5	M
T3-15	9.2	0.125	34.8	M
T3-16	13.1	0.948	36.0	M
T3-17	10.8	0.970	48.6	M
T3-18	22.4	0.086	24.8	S
T3-19	21.6	0.086	43.4	S
*T3-20	24.4	0.151	34.3	MST
T3-21	25.4	0.000	22.7	M
*T3-22	25.4	0.000	42.6	MST
T3-23	17.8	0.000	31.1	M
*T3-24	16.4	0.000	46.4	MST
*T3-25	20.6	0.129	27.9	MST
T3-26	20.7	0.069	50.9	S
T3-27	19.5	0.000	55.9	SD
*T3-28	25.7	0.181	27.4	MST
*T3-29	13.5	0.000	55.8	MST
T3-30	17.6	0.517	26.6	M
T3-31	12.1	0.000	43.7	M
T3-32	11.1	0.056	41.7	S
T3-33	12.4	0.000	40.3	M
*T3-34	15.8	0.000	53.2	MST
*T3-35	12.5	0.000	43.4	MST
T3-36	12.2	0.196	32.8	M
T3-37	12.6	0.052	42.9	S
T3-38	11.6	0.056	52.9	SD
*T3-39	11.2	0.101	30.3	MST

T3-40	12.1	0.151	40.9	M
T3-41	12.2	0.116	50.4	M
T3-42	13.0	0.000	63.1	S
T3-43	32.1	0.000	49.1	SD
T3-44	15.1	0.101	41.1	S
T3-45	10.1	0.050	50.3	S
T3-46	9.3	0.026	55.3	S
*T3-47	27.2	0.000	42.2	MST, SD
T3-48	12.4	0.082	47.3	SD
*T3-49	27.0	0.000	25.3	MST
*T3-50	29.3	0.000	61.5	MST, SD
*T3-51	12.3	0.123	26.9	MST
T3-52	28.6	0.123	43.3	SD
**T3-53	12.8	0.000	25.7	PS
**T3-54	12.1	0.123	34.4	M
**T3-55	12.5	0.123	52.9	M

Key: M: Mixed, S: Stratification, SD: Stratification Degradation, MST: Mixed-to-Stratification Transition, PS: Partial Stratification

The test ID's with the asterisks (*) in the preceding table indicate the cases where problems were encountered with chugging in the injection line, therefore the phenomena observed may not be prototypic due to mixing by chugging in the horizontal injection section. Therefore, these tests will be rerun with an improved injection design geometry which is intended to eliminate the chugging instability. The test ID's in Table 4.11 preceded by a double asterisk (**) indicate that the orifices were inserted in the horizontal vent lines, as shown in Figure 4.8.

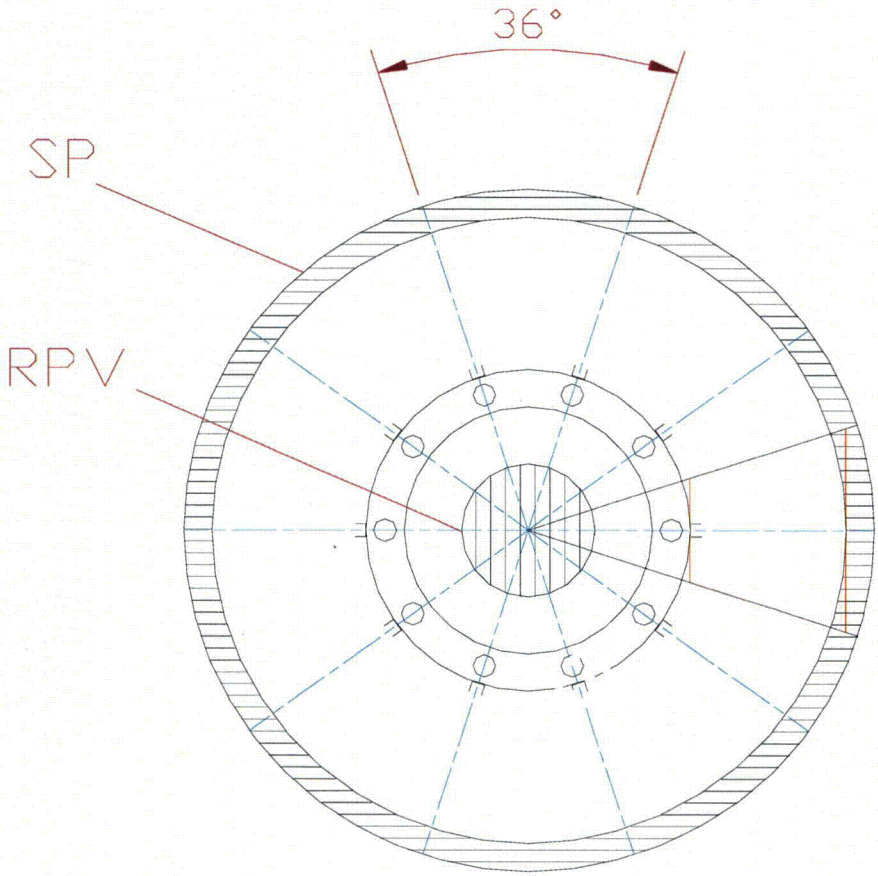

(a) Prototype RPV relative to SP

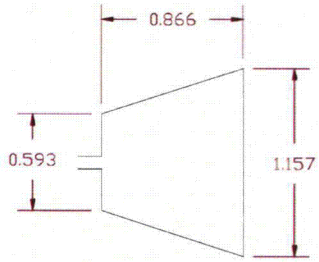

(b) Scaled idealized trapezoidal cross-section

Figure 4.1 ESBWR geometry of RPV and SP showing 1/10 th 'pie' shape

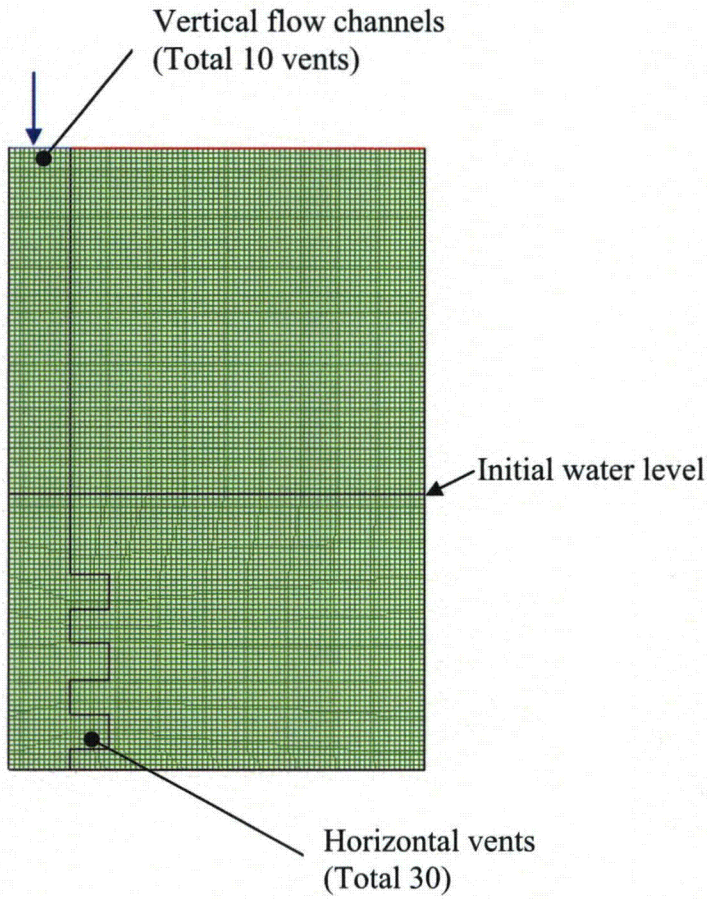

Figure 4.2 Horizontal vent module between the DW and the WW

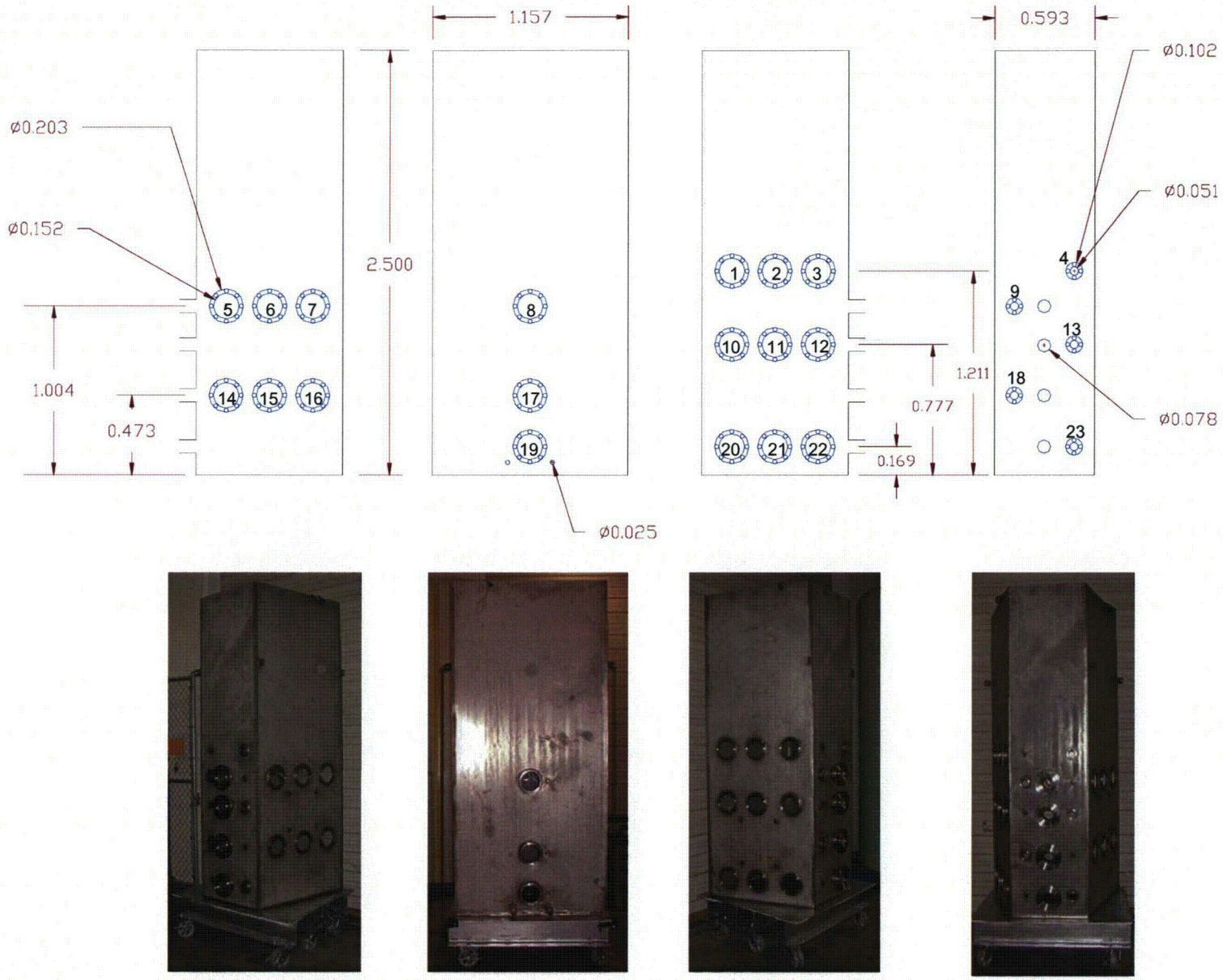

Figure 4.3 Front, sides and back layouts of model pool with window numbering and respective photographs. Units in meters.

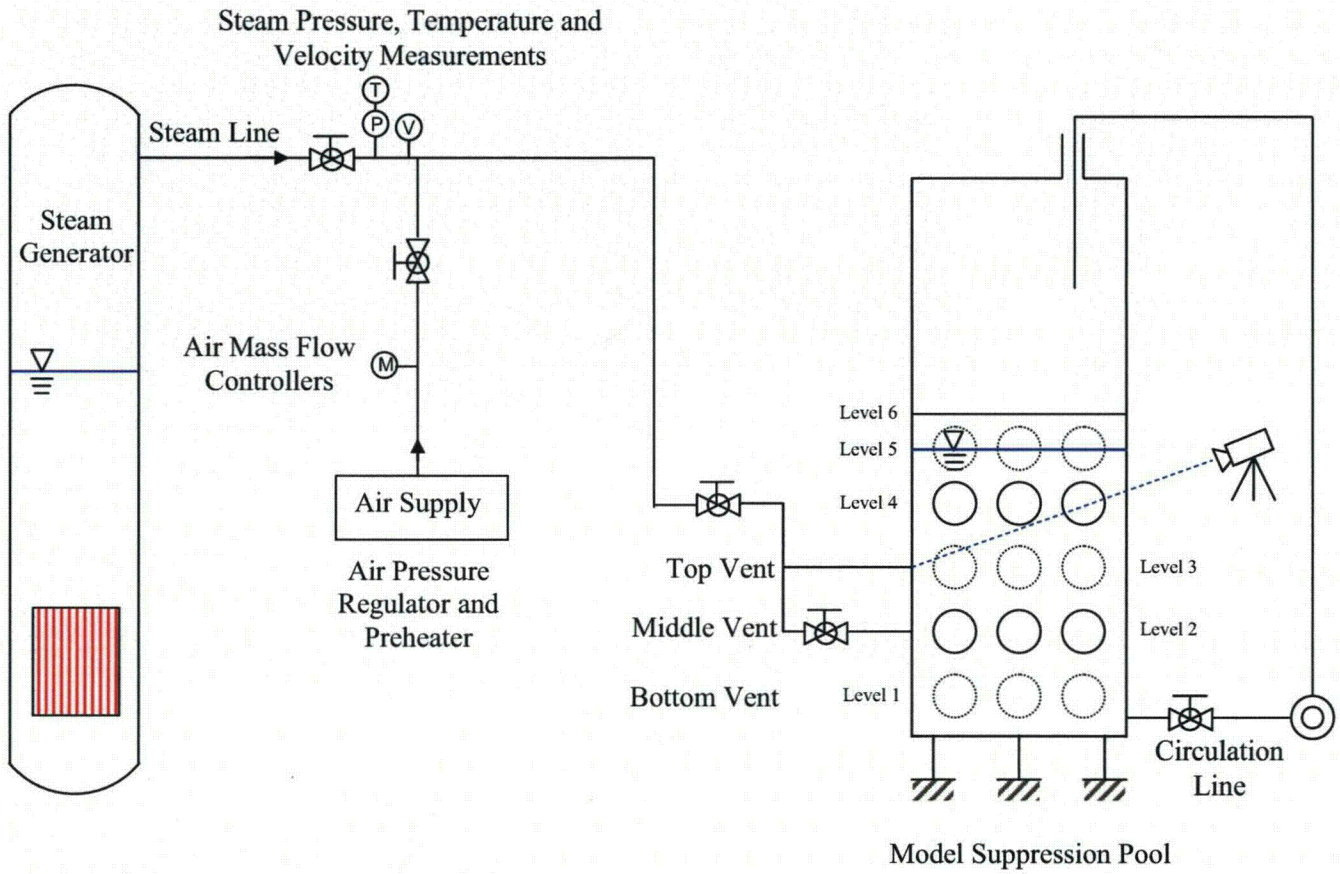

Figure 4.4 Schematic of 1/10th SP model facility showing the levels at which thermocouples are placed (not to scale)

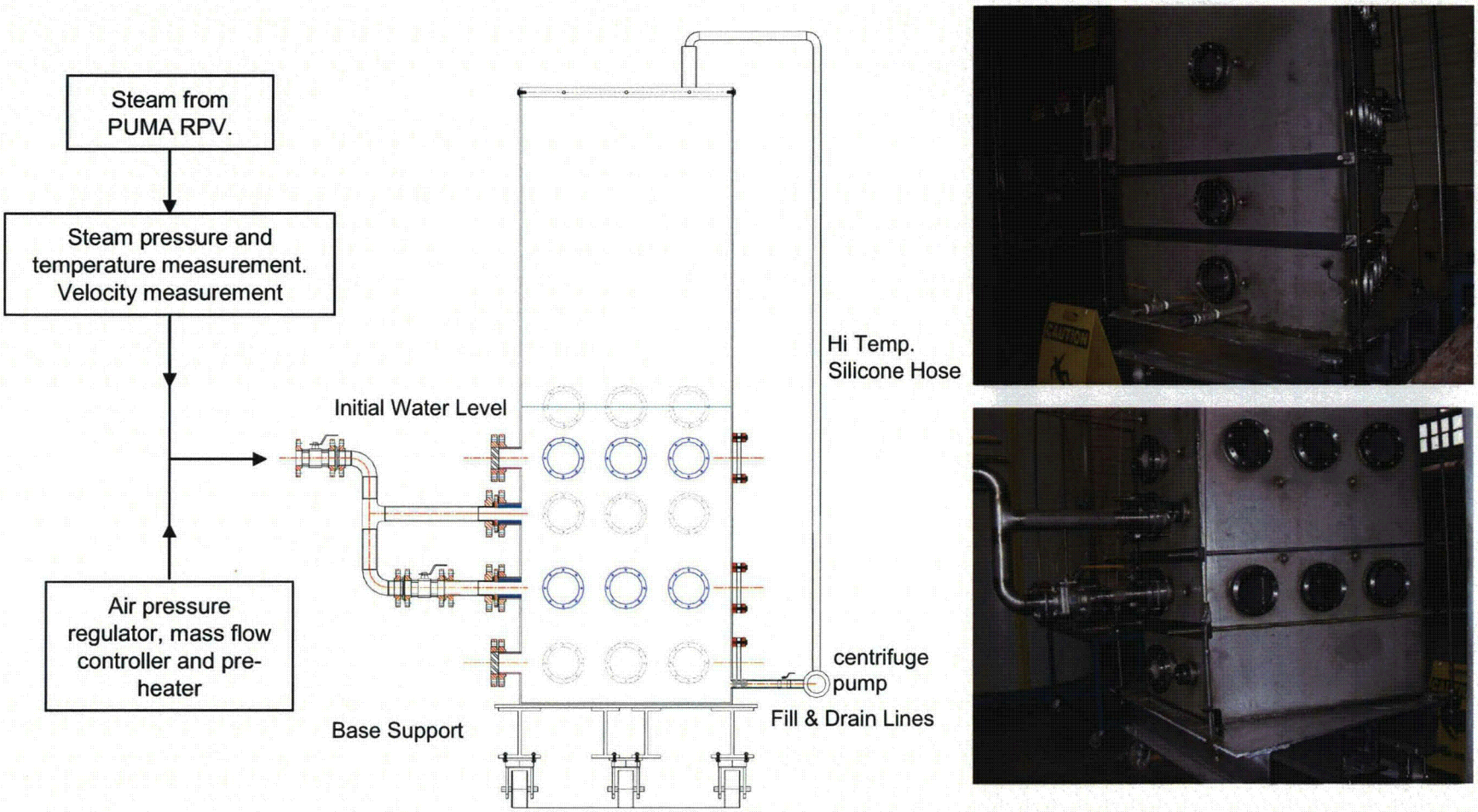

Figure 4.5 Vent and window arrangements of model pool resting on support base

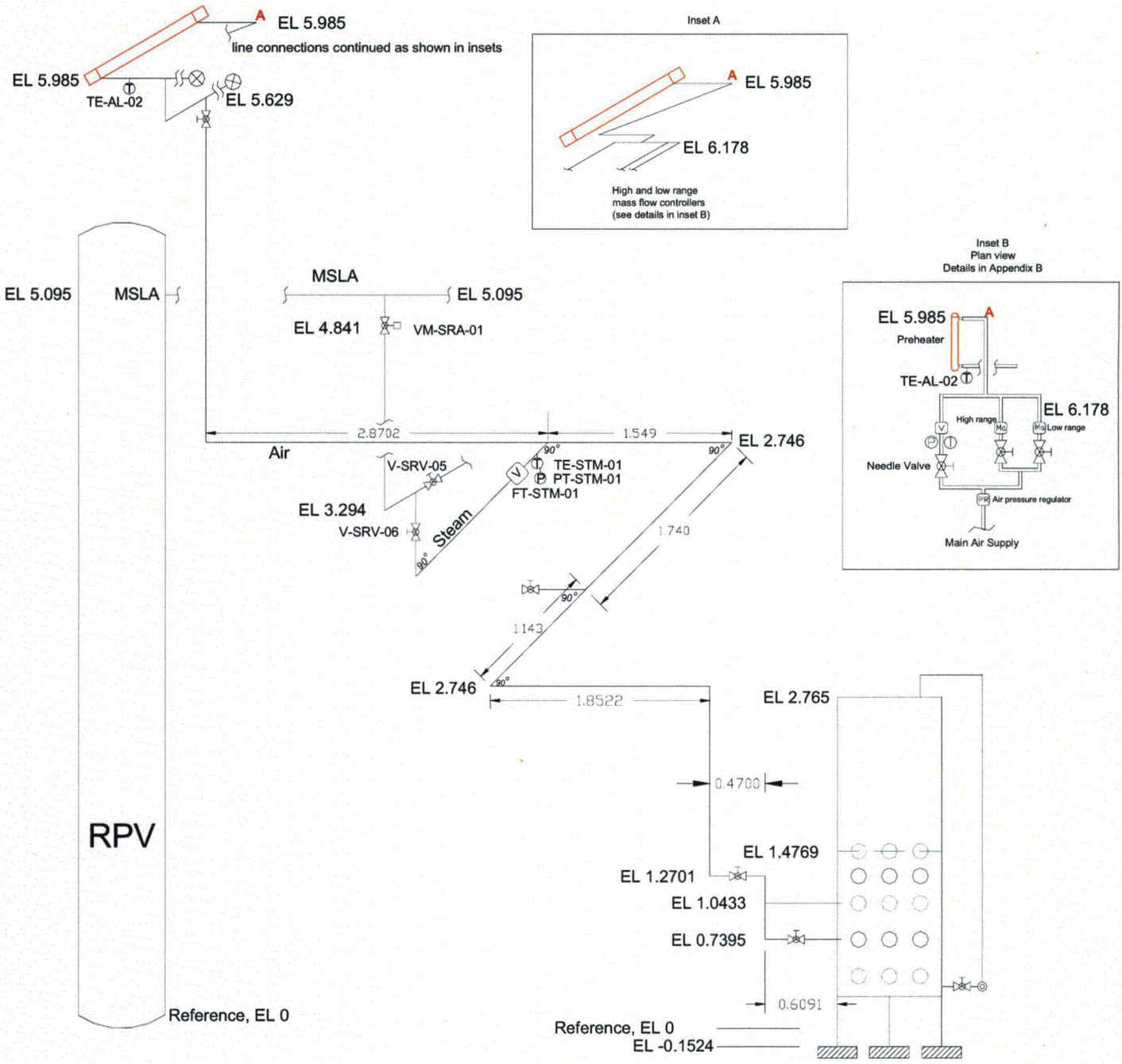

Figure 4.6 Isometric drawing of steam, air and water lines routed from PUMA

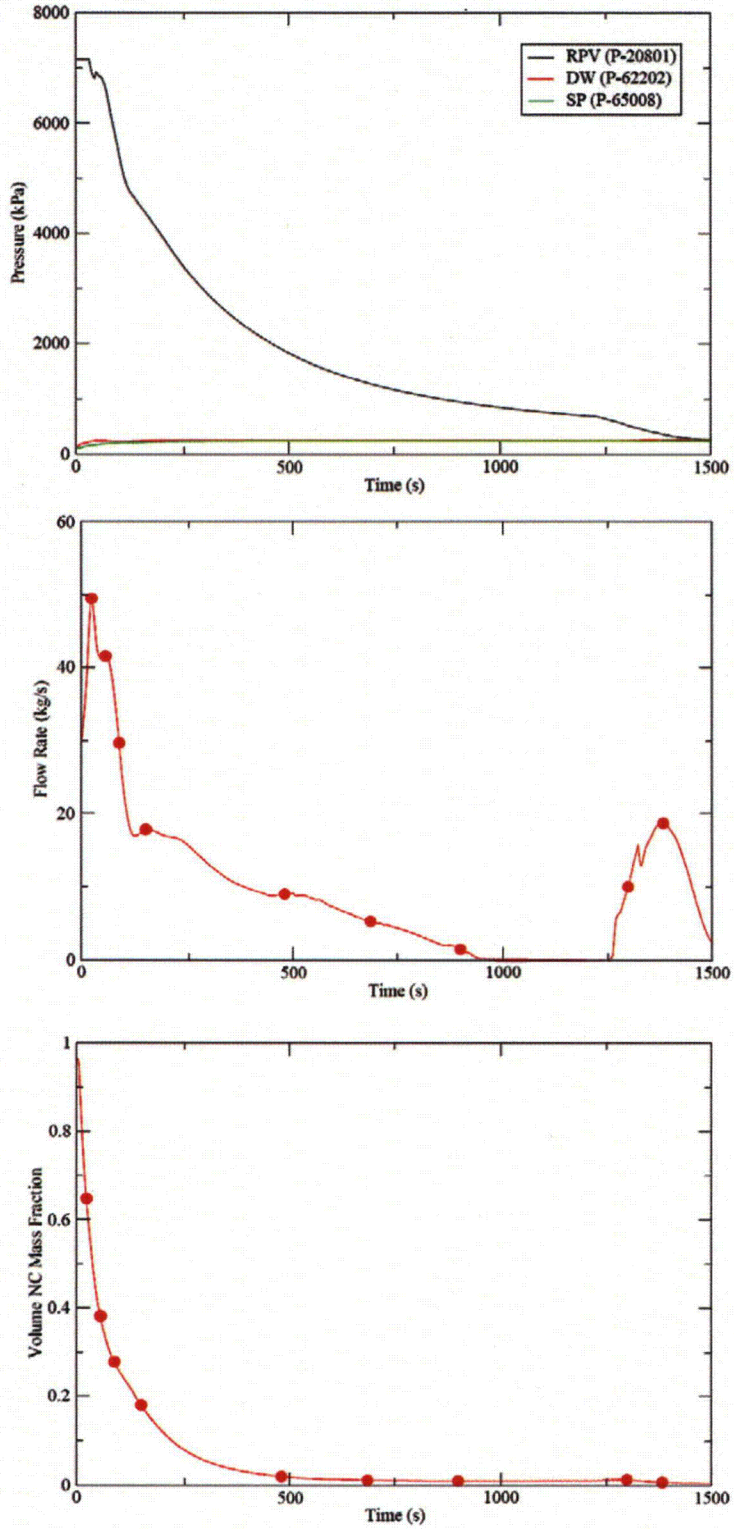

Figure 4.7 Pressure, flow rate and NC mass fraction obtained from RELAP5 simulations of a BDLB scenario over 25 minute duration. [Ref. Woo, 2005]

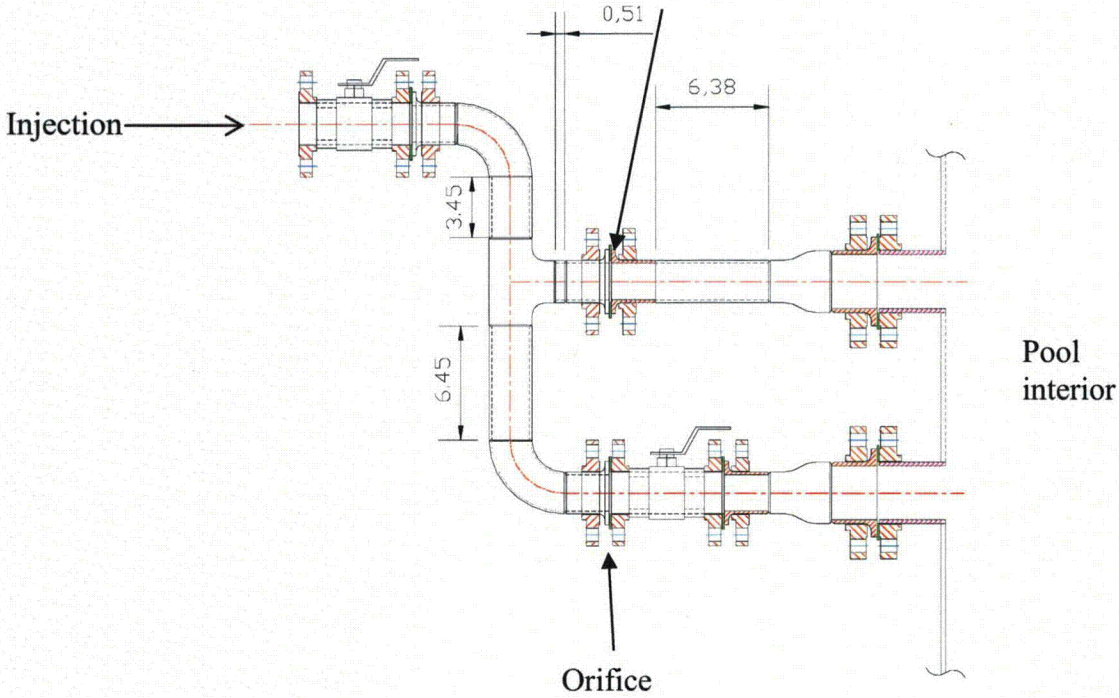

Figure 4.8 Modified top vent for inserting orifice between flanges

4.5 References

Chan, C.K., & Lee, C.K.B. (1982). A regime map for direct contact condensation. *International Journal of Multiphase Flow*, 8(1), 11-20.

Crane Co. 1998, Flow of Fluids through Valves, Fittings, and Pipe. Technical paper No. 410.

Gamble, R.E., Nguyen, T. T., Shiralkar, B. S., Peterson, P. F., Greif, R., & Tabata, H. (2001). Pressure suppression pool mixing in passive advanced BWR plants. [Electronic version]. *Nuclear Engineering and Design*, 204, 321-336.

Ishii, M., Revankar, S. T., Vierow, K., Choi, S. W., Yang, J., & Yoon, H. J. (2004), PCCS Separate Effect Test in the PUMA Facility. PU/NE-04-04.

Ishii, M., Revankar, S. T., Xu, Y., Yoon, H. J., Kuran, S., Cheng, L., Sun, X., Lindsey, M., & Wang, W. (2002). Thermal-Hydraulic Instability Study for Natural Circulation BWRs in PUMA Facility. PU/NE-02-09.

Ishii, M., Revankar, S. T., Dowlati, M. L., Bertadono, M. L., Babelli, I., Wang, W., Pokharna, H., Ransom, V. H., Viskanta, R., Wilmarth, T., & Han, J. T. (1996). Scientific Design of Purdue University Multi-Dimensional Integral Test Assembly (PUMA) for GE SBWR. NUREG/CR-6309.

Ishii, M., Sun, X., Revankar, S. T., Vierow, K., Xu, Y., Kim, S., Yoon, H. J., Cheng, L., Ozar, B., Vasavada, S., Paranjape, S., Kuran, S., Situ, R., Choi, S. W., Lim, J., Norman, T., Woo, K. S., Yang, J. (2004). Second scaling and scientific design study for GE ESBWR relative to PUMA facility with volume ratio of 1/475. PU/NE-04-04.Proprietary

Kim, Y.–S., & Song, C.–H. (2003). Overall review of steam jet condensation in a next generation reactor water pool. In *Proceedings of International Mechanical Engineering Congress & Exposition*. Washington, D.C. The American Society of Mechanical Engineers.

Kocamustafaogullari, G., & Ishii, M. (1997). Scaling of two-phase transients using reduced pressure system and stimulant fluid. *Nuclear Engineering and Design*, 104, 121-132

Kocamustafaogullari, G., & Ishii, M. (1984). Scaling criteria for two-phase flow loops and their application to conceptual 2 X 4 simulation loop design. *Nuclear Technology*, 65, 146-160.

Lee, S. I., & No, H. C. (1998). Gravity-driven injection experiments and direct-contact condensation regime maps for passive high-pressure injection system. *Nuclear Engineering and Design*, 183, 213-234.

Liang, K.-S., & Griffith, P. (1994). Experimental and analytical study of direct contact condensation of steam in water. *Nuclear Engineering and Design,* 143(3), 425-435.

Meier, M., Andreani, M., & Yadigaroglu, G. (1998). Experimental study of large steam-air bubbles condensing in a suppression pool. In *The IMECE/ASME Meeting.* Anaheim.

MELCOR Computer Code Manuals – Materials Properties (MP) Package Reference Manual, NUREG/CR-6119.

Woo, K. S. (2005). Non-condensable gas effect on thermal stratification in the suppression pool. M. S. Thesis. Purdue University

Yadigaroglu, G., & Zeller, M. (1994). Fluid-to-fluid scaling for a gravity- and flashing-driven natural circulation loop. *Nuclear Engineering and Design.* 151, 49-64.

5. INSTRUMENTATION AND EXPERIMENTAL PROCEDURES

Changes in mass and energy inventories from the steam supply vessel (in this case the PUMA RPV) to the model suppression pool are important in quantifying phenomena such as thermal stratification associated with certain mass fluxes. Numerous thermocouples are employed to obtain detailed measurement of pool energy content and distribution via temperature measurements. Appendix A details the list of thermocouple instrumentation mounted inside the pool and Appendix B figures show the layouts of thermocouple distribution. Additional instrumentation that measure steam and air flow rates that are needed to assess injection fluxes and non-condensable mass concentrations are discussed in this chapter. The PUMA reactor pressure vessel contains instrumentation such as DP (differential pressure) cells for measuring the changes in water level and P (pressure) cells for determining the thermodynamic state of the steam. In this way the steam mass output can be matched against the mass condensed steam inside the pool and energy balance calculations can be performed. The following sections discuss details of instrumentation and the experimental approach.

5.1 Instrumentation

Thermocouple junctions were made from duplex-insulated ANSI *K*-type wires. The wires are Teflon-coated solid wires with a nominal size of 0.024 in. x 0.040 in. (gage 30). Using these *K*-type thermocouple wires, 64 thermocouple junctions using these gage 30 *K*-type thermocouple (TC) wires were made by twisting the wire pairs together and spot welding them at the junction. These were made in 32 feet lengths so that at one end the junctions would be immersed inside the pool and the free end could connect to a DAS (data acquisition system) some distance away from the measurement point. Each thermocouple was tested at room temperature using an 'ultramite' high resolution thermocouple tester from Thermo Electric Instruments. This thermocouple size provides for higher stability of temperature measurements in these tests with the drawback of having less accuracy. The response to temperature changes, however, is better for

recording temperature fluctuations during condensation oscillations. The appendix shows the coordinates and tag names of the thermocouples.

Tables 5.1 and 5.2 outline the specifications and ranges of the vortex flow meter and mass flow meters that are used in this experiment. The vortex flow meter is used to measure the steam flow rate that is set with the RPV heater power. The maximum range of the VP715TS model vortex flow meter for steam at atmospheric conditions is 0.029 kg/s, which is within the maximum range of steam flow rate desired for the experimental conditions. Air mass flow controllers are used to set the air mass flow rate.

Table 5.1: Range of vortex flow meter

FLOWMETER				FLOW RANGE (kg/s) IN STEAM									
MODEL	PIPE SIZE (inch)	ACFM		273.7 (kPa)		446.1 (kPa)		618.5 (kPa)		790.8 (kPa)		1135.6 (kPa)	
		MIN	MAX	MIN	MAX	MIN	MAX	MIN	MAX	MIN	MAX	MIN	MAX
VP715TS	1.5	3	100	0.0018	0.071	0.003	0.113	0.004	0.154	0.005	0.194	0.007	0.274
TEMPERATURE (DEG-C)				131		147		160		170		186	

Table 5.2: Air mass flow controllers

Type	Vol. flow rate (l/min)	Mass flow rate (g/sec)	Error range
1	0-100	0 – 1.96	1.5 % (± 0.0296 g/sec)
2	0-500	0 – 9.80	1.5 % (± 0.1470 g/sec)

The range of the mass flow controllers (Ishii et al, 2004) enables one to perform experiments with 25% non-condensable gas mass fraction using the maximum measurable steam flow rate. A pressure regulator is used to control the upstream air pressure and an air pre-heater attached to the air line is used to heat the air to a desired temperature before it is mixed with the steam. The positions of these as well as the positions of the flow controllers are shown in Figure B.1. In addition to these instrumentation, Table 5.3 summarizes the other instrumentation and Table 5.4 indicates the related phenomena of interest sought by the utilization of the specific instrumentation.

Data obtained provide information on the phenomena of interest as indicated in Table 5.4.

Table 5.3: Instrumentation

Instrument	*Measurement*
*K-type Thermocouples (62)	Temperature in pool
*Surface Thermocouples (2 k-type)	Floating on pool surface
†P Cell, PT-STM-01	Pressure
†Vortex flow meter, FT-STM-01	Low steam flow rate
†Mass flowmeter (2), MA-AL-01, MA-AL-02	High and low air flow rates
Laser Doppler Velocimeter	Local liquid velocity
Camera (high speed)	Flow visualization

* Details are given in Appendix B
† Refer to Figure 4.4

Table 5.4: Parameters measured and phenomena of interest

Measurement	*Phenomena*
Temperature	Thermal Stratification
Visualization	Jet – plume extent
Laser Doppler Velocimeter Visualization	Pool mixing and circulation
Laser Doppler Velocimeter High speed camera	Local liquid velocity and circulation

A skeleton frame for holding the thermocouple wires is shown in Figure 5.1. The frame itself is a regular parallelepiped fitted with sliding bars. It has a trapezoidal cross-section that is designed to fit and stand inside the model suppression pool without

additional fastening. The frame stands about 54.5 inches high which is higher than the initial water level inside the pool. It is designed to hold instrumentation such as thermocouples not only in the water volume but also in the gas space above the water level. The sliding bars are attached to the frame with clamps to position and anchor wires at desired coordinates within the volume. The wires, which are thin soft-temper stainless steel wires (0.032 gage), are placed in tension along the sliding bars and then clamped in to position. These wires would serve for holding instrumentation. As an initial guess, the wires are placed according to a developing and fully developed region; this is depicted in Figure 5.1. Schlichting (1960) (in Gamble et al. 2001) suggested that a fully developed jet extends linearly with axial location given by equation 5.1. For a forced turbulent jet the developing and fully developed regions can be given by equation 5.1

$$\left.\begin{aligned} \frac{r_{1/2}(x)}{r_0} &= \left(1+0.013\frac{x}{r_0}\right) \quad \textit{for} \quad \frac{x}{r_0} \le 8.75 \quad \textit{Developing region} \\ \frac{r_{1/2}(x)}{r_0} &= 0.0848\left(4.39+\frac{x}{r_0}\right) \quad \textit{for} \quad \frac{x}{r_0} > 8.75 \quad \textit{Fully developed region} \end{aligned}\right\} \quad 5.1$$

The radius $r_{1/2}$ along the axial extent x of the jet can be determined once the initial jet radius r_0 is known. Thermocouples locations are not restricted to the injection region and effluent horizontal path but are placed within (see Appendix B) strategic grid locations to simultaneously measure temperature at various locations with as minimum as possible interference. The thin soft-temper stainless steel wires and thermocouple wires are selected to offer minimum resistance to the injected vapor and flow field.

5.2 Data Acquisition System

A Keithley 2700 model digital multi-meter (DMM) data acquisition system (DAS) is being used. This model can be configured for various thermocouple types including *K*-type thermocouples. This DAS has a high resolution of 6 ½ digits (22-bits) which, when configured for a given thermocouple type, has a maximum scanning rate of

around 40/50 samples per second. This Keithley 2700 model is modularly configurable and has 2 slots. Two 7708 cards allow 40 thermocouples to be scanned per card for a maximum channel count of 80. Each card has multiple (usually 8 or 9) cold junction compensation (CJC) spread out and uses a sophisticated mathematical algorithm to weigh the value of each CJC value while taking into account of how physically close it is to the thermocouple junction. The result is a very accurate CJC value for thermocouple conversion, all done internally and automatically. All thermocouple conversions are done on board once the thermocouple type is specified and CJC (internal or simulated) is fixed. The DMM is controlled from a PC via a PCI GPBI card and PCI bus. Data are sent to the GPIB (PCI) so that it is stored in PC memory. The communication between GPIB card and the instrument is through ASCII strings (which can also be formatted as binary). An ExceLINX-1A Microsoft Excel add-on software allows data to be input and controlled in Excel spreadsheets.

The data acquisition card was installed to a Compaq computer. The appropriate driver (cec488) was installed and connections were made including the GPIB-PCI IEEE communication bus. The equivalent 'expansion board' was installed to the Integra system prior to connecting the thermocouples. As previously mentioned, this state-of-the-art DAS has cold junction compensation and can measure thermocouple readings simultaneously and accurately within the limitations of the response time of the thermocouple (TC). Minimum programming was required after installation of the software; however, configuring the software was mandatory to match the type of DAS. After tests were done to determine whether the system was communicating, a trial run was performed to take data for a short duration of time. Some programming was required for the DAS software to output a data file containing the thermocouple measurements. All data files were stored and backed-up for all tests.

5.3 Test Procedures

The following discussion briefly outlines the experimental method of operation adopted for these tests.

(i) Water used for experiments was demineralized using a water filter prior to all tests.

(ii) Prior to using the RPV, it was preheated to achieve pressures between 25 and 10 psig depending on the steam flow rate desired and any air in the vessel was purged outside until the vent gas temperature was equal to the steam saturation temperature at the exit.

(iii) The pre-test procedures consisted of assuring power availability, DP (differential pressure) cell sense line purging on the PUMA RPV for accurately monitoring the RPV water level. The water level was set to approximately 4.2 m in height. The DAS system was checked and all manual valves were lined up for the tests.

(iv) The pool initial water level was also set to a pre-determined value using the fill and drain lines (see Figure 4.6). The RPV was preheated and steam was discharged to the pool to set its initial temperature for high initial temperature cases. A circulation pump fitted to the pool was used to circulate the pool water so that the bulk initial temperature was homogenized. The pump was also used to reduce the bulk temperature if the pool had to have higher subcooling.

(v) Using the PUMA steam supply, the steam mass flow rate was controlled by the heater power, where $\dot{m}_s = \dot{Q} / h_{fg}$ and $\dot{Q}$ is the RPV heater power. The steam flow rate was monitored by the vortex flow meter until it was stabilized. The range of the vortex flow meter is shown in Table 5.1

(vi) The steam mass flow rate was set by the RPV power and it maintains a constant value by maintaining a constant upstream stagnation pressure in the PUMA RPV by choking the steam flow using V-SRV-06 (refer to Figure 4.7).

(vii) Air mass flow controllers were used to set the air volumetric flow rate and the arrangement is shown in Figure B.1 in Appendix B. The specifications of the flow meters are shown in Table 5.2. The air was preheated using a preheater to the steam saturation temperature before it was mixed with the steam

(viii) The steam temperature and pressure were measured just downstream of the vortex flow meter prior to the two gas streams being joined at a tee.

(ix) The inlet vapor temperature T_m was monitored although there was some difficulty in controlling T_m due to the large thermal inertia of the piping system. However, assuming the steam was saturated and in thermal contact with air the mixed streams were allowed to run for a while before taking data until the desired flow rates and temperatures are achieved.

(x) Data were taken for 1800 seconds usually and in some cases for over 5000 seconds. Temperatures at discrete locations inside the pool as well as the voltage signals from the vortex flow meter and P cell were monitored during the course of every test so that proper action could be taken if any irregularities in the system conditions occurred or injection fluxes strayed from a quasi-steady condition.

In summary, 3 parameters were adjusted independently; these are steam and air mass flow rates and pool bulk temperature. Since the system pressure near the vent exit was approximately constant (around atmospheric pressure), the gas compressibility had an influence on the bubble size and frequency. Furthermore, the steam quality would have an influence on the condensation mode at the vent exit. The vent configuration would also have an influence on the steam quality; for instance a divergent nozzle near the vent exit will act to reduce the steam quality. This would also have the effect of reducing the gas momentum at the exit. Therefore two injection sizes have been considered, these are: (a) a 2-inch vent and (b) a 2-inch to 3-inch diverging nozzle.

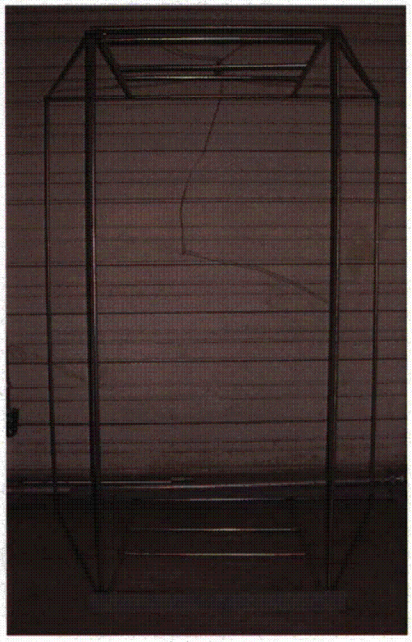

(a) Front

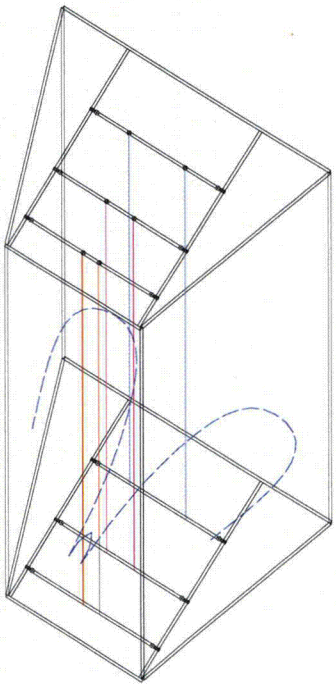

(b) Side

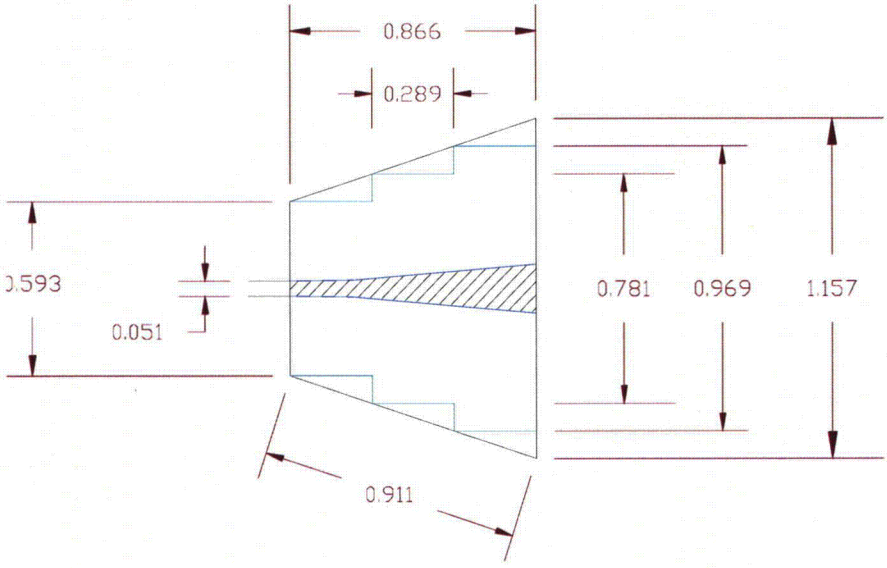

(c) Top

Figure 5.1 Thermocouple cage frame showing a few wires suspended on the sliding bars

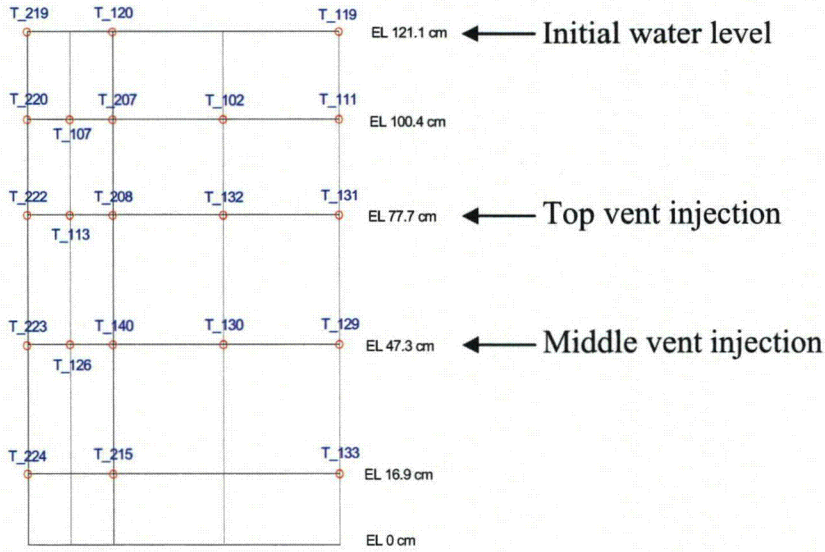

Figure 5.2 Thermocouple locations along pool center plane.

5.4 References

Gamble, R.E., Nguyen, T. T., Shiralkar, B. S., Peterson, P. F., Greif, R., & Tabata, H. (2001). Pressure suppression pool mixing in passive advanced BWR plants. [Electronic version]. *Nuclear Engineering and Design*, 204, 321-336.

Ishii, M., Revankar, S. T., Vierow, K., Choi, S. W., Yang, J., & Yoon, H. J. (2004), PCCS Separate Effect Test in the PUMA Facility. PU/NE-04-04.

6. FACILITY CHARACTERIZATION AND PRELIMINARY DATA

6.1 Pool Structural Heat Losses

A conservative calculation is performed to determine the heat loss in the pool with 1.5-inch thick insulation blanket insulating the sides, front and back of the pool structure. The calculation assumes a static case in which the temperature of the pool bulk water volume is 353 K and the temperature of the pool inner walls are uniform. As indicated in equations 6.1 and 6.2, the pool walls are taken to be in thermal contact with the hot water, and the outer walls are insulated from the ambient air. The following information in Table 6.1 was used to calculate heat losses.

Table 6.1 Parameters used for calculating pool heat loss

Parameter	Value
Insulation thickness, t_1	0.0381 m
Pool wall thickness, t_2	0.00635 m
Water layer thickness near wall, t_3	0.01 m
Area of back plate, A	1.401 m^2
Area of side plate, A	1.049 m^2
Area of front plate, A	0.718 m^2
$\Delta T = (T_{pool} - T_{air})$	(383-303) K = 80 K
Air, heat transfer Coefficient, h_4	7.949 W/m^2-K
Insulation thermal Conductivity, k_1	0.039 W/m-K
Stainless steel thermal conductivity, k_2	14.41 W/m-K
Carbon steel thermal conductivity, k	50.2 W/m-K
Water thermal Conductivity, k_3	2.1247 W/m-K

The heat loss is taken to be

$$\frac{Q}{t} = UA(\Delta T), \text{ with } U = \frac{1}{R} \tag{6.1}$$

$$R = \left(\frac{1}{h_4}\right) + \left(\frac{t_1}{k_1}\right) + \left(\frac{t_2}{k_2}\right) + \left(\frac{t_3}{k_3}\right) \tag{6.2}$$

Insulation + stainless steel + water + air

Heat losses through sides, back, and front are 0.25 kW, 0.17 kW, and 0.09 kW respectively. The estimated total loss is about 0.51 kW. The evaporation heat transfer from the pool surface which is very important in determining the steam partial pressure in the SP cover gas of the prototype is not considered here since we are primarily interested in the losses due to the pool structure. This loss represents 1.3% of an input power of 40 kW.

The mass and energy balance in the model wetwell are calculated using the following equations:

$$\dot{Q}_{in} = \dot{Q}_{cond,pool} + \dot{Q}_{evap} + \dot{Q}_{loss} \tag{6.3}$$

$$\dot{m}_s h_{fg} t = \left[M_{final} \cdot c_{p,f} \left(T_{ww,final} \right) \cdot T_{final} \right] - \left[M_{initial} \cdot c_{p,f} \left(T_{ww,initial} \right) \cdot T_{initial} \right] + Q_{evap} + Q_{loss} \tag{6.4}$$

where $Q_{evap} = h_{evap} \left(T_{ww,g} - T_{ww,f} \right) A_{evap} t$

h_{evap} = evaporation heat transfer coefficient

A_{evap} = area available for evaporation heat transfer form pool surface to gas space

$\dot{Q}_{evap}$ determines the steam contribution to the pressure in the SP gas space in the actual prototype.

6.2 Scoping and Feasibility Tests

Preliminary results of scoping tests for 2-inch pipe diameter vent injection are discussed here. The pool section vent arrangement is also equipped to study venting from a 3-inch diameter cross-section (see details in Figure B.6). The purpose of these scoping tests is to evaluate the maximum range of the facility in terms of the power to volume ratio and the energy and mass transfer rates that are associated with a prototypic accidental scenario. Energy balance calculations, using equations 6.3 and 6.4, were

performed for all test cases. The energy supplied by the PUMA RPV was matched to the energy increase in the pool using equation 6.4. The structural heat losses are also taken into account. Table 6.2 summarizes the pure steam and steam-air mixture scoping tests. A total of 8 tests performed are reported here; 4 tests for pure steam and another 4 tests for steam-air mixture injection cases. The typical cases of pure steam and steam-air injection are depicted in detail in the sections that follow. Cases 1 and 2 are for pure steam single- and double-venting respectively, and case 6 is a steam-air single vent case. Detailed plots are given for cases 1, 2, and 6 and are shown in Figures 6.1 through 6.15 for comparison. Figures 6.16 through 6.20 show timed photographic sequences of bubble motions inside the suppression pool as captured through the viewing ports (Figure 4.4).

Table 6.2 Summary of pure steam and steam-air mixture scoping tests

CASE #	Pool init Temp (°C)	Pool final water level (m)	Air mass flow rate (g/s)	Steam mass flow rate (g/s)	Vent opening
1	20.4	1.273	0.00	37.2	Level 3
2	24.3	1.334	0.00	34.6	Level 2 & 3
3	23.5	1.303	0.00	30.2	Level 3
4	23.5	1.300	0.00	25.4	Level 3
5	41.2	1.257	0.56	16.3	Level 3
6	58.8	1.251	0.56	18.9	Level 3
7	42.0	1.295	1.05	22.8	Level 3
8	22.3	1.264	1.03	16.0	Level 3

Data were taken over a period of time so as to track both the vertical and horizontal development of the temperature distribution inside the pool volume. Every thermocouple data were plotted with the variation of time and the ones that are not presented in this chapter can be referred to in Norman et al., 2005. Also a 2-D linear interpolation function in the *matlab* software was used to interpolate the thermocouple data in the vertical center plane within the measurement domain to produce 2-D temperature maps spanning the time of the experiment. Another *matlab* program plotted the 2-D surface temperature using the discrete thermocouple values at level 5 (see Figure

B.11) which measures the temperature distribution at the initial water level. Two floating thermocouples also provided a means of tracking the temperature of the pool surface both near the vent side and at pool side as the mass inventory increases during each test.

The elevations (y) for levels 1 through 6 are defined in Figure 4.3, 4.4, 5.2 and Appendix B, where $y = 0$ indicates the bottom of the pool. In the trapezoid cross-section, the locations of thermocouples are defined by co-ordinates (x, w), with (x, w) = (0, 0) defining a point on the axis of symmetry of the trapezoidal cross-section. The placement of the coordinate system can be seen from Figures 6.4 and 6.5. The mixture injection fluxes used in these tests are much lower than the range used by Chan and Lee (1982) as shown in Figure 3.1 where the injection fluxes are generally less than 25 kg/m^{2}s and the initial pool temperatures used are greater than 20 °C. Their injection orientation is downward and similar phenomena such as oscillation condensation are observed in our tests. However, in a vertical orientation of a smaller diameter exit and with a controlled release of the steam effluent, a single detached bubble can be achieved at high fluxes and high subcooling with less break-up at the exit. The results of the tests reported in this chapter show oscillations and breakup that lead to a two-phase condensing jet plume. The following sections provide discussions of the results of steam and steam-air injection and phenomena observed from temperature data along with a qualitative assessment of high frame-rate images. The major conclusions drawn from some cases are also summarized.

6.2.1 *Pure Steam Injection Cases*

Case 1 shows a steam flow rate of 49.56 g/s and an initial pool temperature of 20.4 °C, and its temperature data in the suppression pool are shown in Figures 6.1 through 6.5. The initial pressure of the PUMA reactor pressure vessel was maintained at around 9 psig and the steam was generated using the internal electrical heater rods. Steam was injected to the pool at level 3 (y = 77.7 cm).

Figure 6.2 shows the time variation of water temperature in the suppression pool at levels 1 to 5 on the vent side of the pool. As the steam is injected through the vent pipe, temperatures increase gradually in the suppression pool. After the steam supply is shut off around 1150 seconds, it can be observed from the temperature data that the thermal stratification persists to 1700 seconds when the data acquisition system is stopped, defining an equilibrium state. The temperature strata are sharply defined after the steam supply is shut off; this is due to the effects of gravity causing less dense fluid to arrange itself as horizontal thermoclines above the more dense fluid. Figures 6.2 and 6.3 show the real time temperature data at the centerline near the vent side and far wall respectively. Both temperature profiles are similar to the case of level 1 as its location is below the venting elevation.

Figures 6.4 and 6.5 show the real time temperature profiles at the centerline and pool surface (y = 121.1 cm) respectively. The temperatures exhibited a fluctuating characteristic as the steam exited through the venting pipe. The intensity of these fluctuations was much higher near the vent exit than away from the vents where it gradually dampened (Figures 6.2 and 6.3). As shown in Figure 6.2, the temperature variation of T_222 shows the oscillations due to condensation at the vent exit. However, this temperature data is not a clear indication of the actual periodicity of the oscillations since it was observed that these occurred with much higher frequency than the response time of the thermocouple. In this case, high frame rate photographic images from a high speed camera proved to be a better way to track the movement and frequency of the effluent exiting and retracting between the vent exit and the pool. At level 4 (y = 100.4 cm) the temperature profiles showed little fluctuation due to the rising bubbles or hot plumes from the vent exit. Figure 6.2 shows that the temperature, although fluctuating at the vent exit (T_222), had less fluctuation above the vent exit due to the thermal mixing and damping of these fluctuations. Partial thermal stratification was observed below the vent exit. The path of the jet-plume can be indirectly inferred from the temperature response of the pool. The trend shows that the pool water volume began to be thermally stratified from the start of the test. This phenomenon can be observed in Figures 6.2 and 6.3 for both the vent side and pool side vertical thermocouples and in Figures 6.4 and 6.5

for two-dimensional temperature distributions of vertical center plane and pool surface for certain times. The actual movement of the stratification is also interesting. From 1000 seconds, the warmer liquid occupies mostly the volume of water above the vent, however, that horizontal boundary slowly moves downward (at 1600 seconds on Figure 6.4) with time as the upper liquid starts to become saturated. The surface of the liquid maintains some degree of homogeneity of temperature; however, it can be observed in Figure 6.5 that closer to the near wall the temperature is slightly higher than at the far wall.

The temperature profiles at level 5 (y = 121.1 cm) show the similar trends as level 4. However, the temperature profiles at level 6 are different because level 6 (y = 128.43 cm) is above the initial water level. The random perturbations of temperatures above the initial pool level are due to the back and forth motions of the water surface which contributes pool swelling (Figure C.9 in Norman et al., 2005 for example). The two-phase water level increased as the mass was added to the suppression pool due to the condensation of supplied steam, and the water density decreased due to the increased pool temperature. The two-phase water level increased to immerse the thermocouples at level 6 around 500 seconds and their temperatures are near surface temperatures similar to those of level 5. As the steam supply was terminated, the collapsed water level went below level 6 and the temperature measured is the gas space temperature near the pool surface. Figure 6.1 shows the real time temperature data at the water surface measured from the floating thermocouples. These thermocouples, T_109 and T_117, were mounted on small pieces of Styrofoam floats and were used to track the water surface temperatures throughout the test run. T_109 and T_117 are located near the front and back walls of the pool, respectively.

Case 2 shows a steam flow rate of 34.59 g/s with initial pool temperature of 24.3 °C, and its temperature data in the suppression pool are shown in Figures 6.6 through 6.10. The initial pressure of the reactor pressure vessel was maintained at around 15.8 psig. In this case, steam was allowed to vent at both the middle (level 2) and top (level 3) vents simultaneously. This case is considered to be a transient scoping test since the

lower vent was shut off around 900 seconds and then turned back on around 1550 seconds. During the test the complete mixing phenomena was observed while the injected mass flux was held constant. The steam mass flux was redistributed across both vents by manipulating the middle vent at level 2. Venting communication and desynchronization were observed and shown in Figure 6.9.

A two-phase jet plume was observed at level 3, while at level 2 the effluent was a hot liquid jet plume with a smaller but more horizontal penetration into the pool. Cases 1 and 2 can be easily compared from the pool surface temperature and the temperature distribution along the vertical center plane. Figures 6.6 through 6.10 for case 2 are compared with Figures 6.1 through 6.5 for case 1.

6.2.2 *Steam-Air Mixture Injection Cases*

Case 6 has a steam flow rate of 18.92 g/s, an initial pool temperature of 58.8 °C and an air flow rate of 0.56 g/s (3% non-condensable mass concentration). The corresponding temperature data in the suppression pool are shown in Figures 6.11 through 6.15. During the test no stratification was observed and the pool volume was entirely mixed. The non-condensable gas had a tendency to carry more steam from the pool vent side and to mix the pool interior while decreasing the condensation rate and providing additional buoyancy. This effect can be seen from Figures 6.14 and 6.15. At the initial stages the water surface temperature near the vent side is about 4 degrees higher than the pool side, but this difference was reduced as the experiment progressed and the mixing behavior became more pronounced.

6.2.3 *Flow Visualization*

Figures 6.16 through 6.19 show timed photographic sequences of the horizontal venting under different steam mass flow rates, frame rates and view ports. The images in

Figures 6.16 and 6.17 were taken at the frame rate of 125 fps or with 0.008-second intervals. Their initial pool temperature is 20 °C with an injection steam superficial velocity of approximately 40 m/s, or a steam flow rate of about 50 g/s. The vent exit cannot be seen in the photograph since the camera focus is zoomed out. The vent exit location is at the right of the frames. The flow is from the right to the left with gravity pointing downwards. These images show the movement of the injected jet-plume front very well as it exits the vent. Figure 6.17 shows a continuation of the sequence of Figure 6.16. However, for this case there is suction of liquid into the vent followed by residual recirculation patterns, as shown, following which an isolated eruption occurs causing steam to suddenly burst into the pool. The frame numbers are located below each photograph in order to determine the time lapse between frames for a 125-frame-per-second framing rate.

Figures 6.18 and 6.19 show the photographic sequences for pure steam injection with flow rates of 20 and 50 g/s respectively. These images were taken at view port 8 with a framing rate of 60 fps or at 0.017 second intervals. It can be seen in Figure 6.18 how the buoyancy force of the jet-plume results in a vortex pair that propagates to the top of the pool. This is in analogy with the vortex pair that is produced when a vertically injected jet plume is subjected to cross flow as shown in Figure 6.20. The analogy of the 'bent-over' cross flow of a jet-plume, as depicted in Figure 6.20, is compared to the visualization results in Figure 6.18, where the buoyancy flux provides the velocity for the cross flow causing a vortex-pair to result and propagate to the top of the pool. Figure 6.19 shows the case, as viewed from view port number 8 (see Figure 4.6), of a higher injection moment flux when the vortex pair disappear and a single toroidal cell forms around the effluent, with the upper part having more buoyancy. At the top part of the toroid, bubbles are detached before the jet-plume propagates towards the far wall; these detached steam bubbles rise to the surface with characteristic spherical and cap shapes, most of which completely condenses before hitting the pool surface. More horizontal penetration was observed at higher injection flow rates, whereas a tendency towards plume behavior was observed at steam injection flow rates of lower than 20 g/s for this 2-inch diameter vent case.

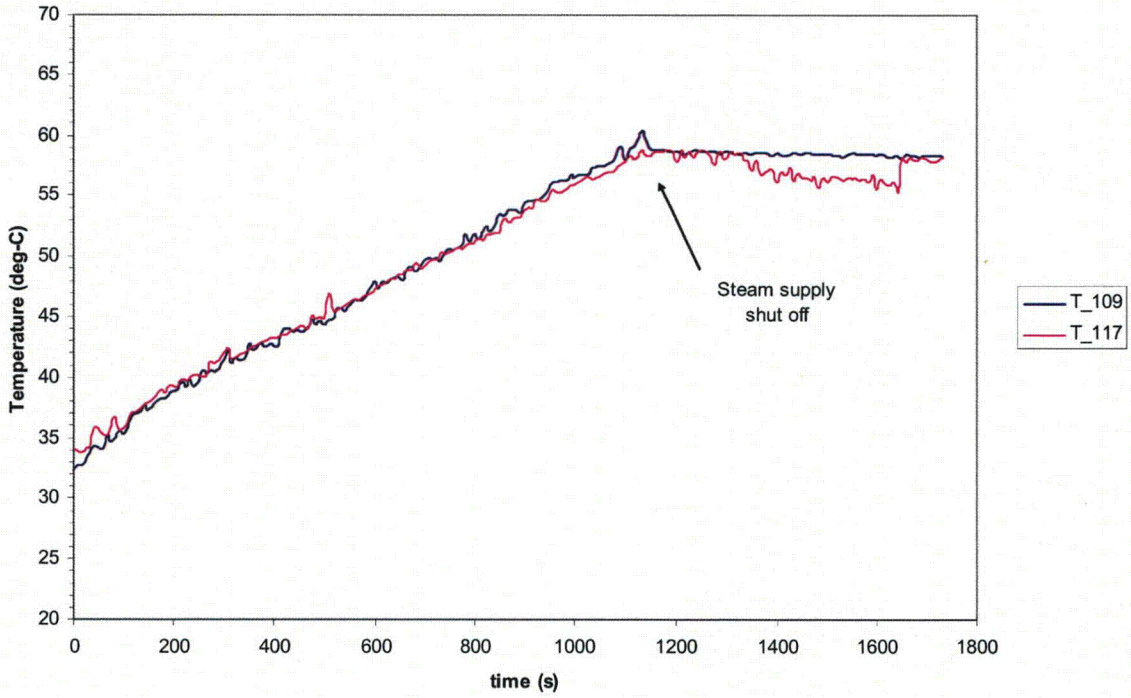

Figure 6.1 Real-time temperature data at the water surface for Case 1

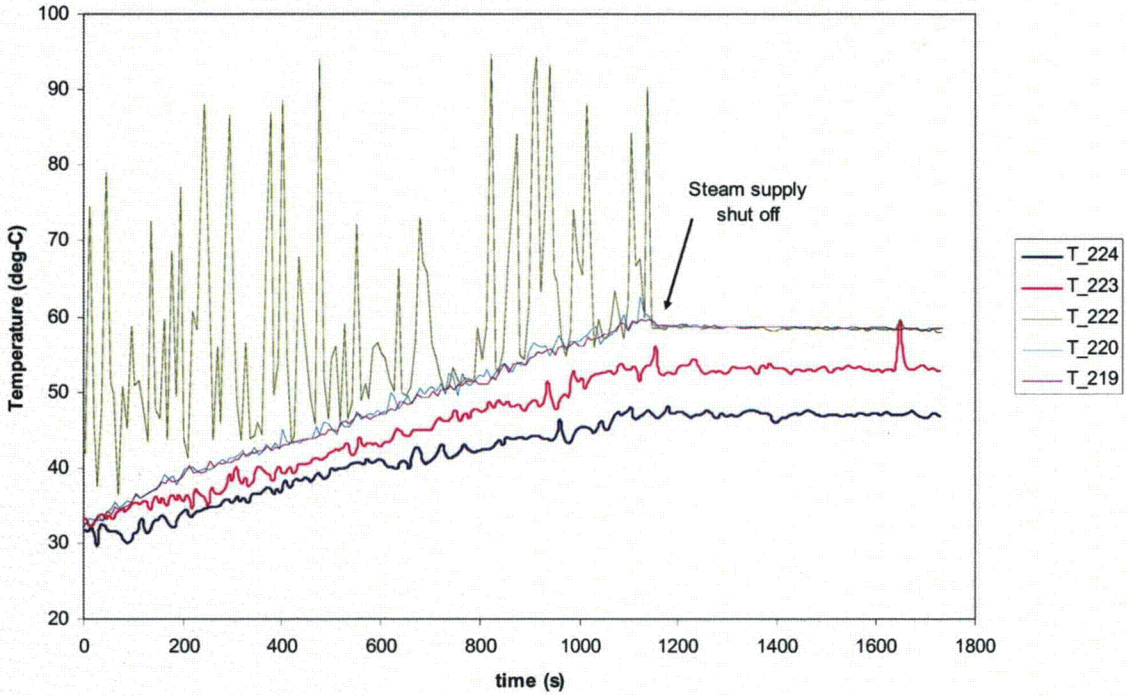

Figure 6.2 Vertical temperature distributions along the vent side centerlines for Case 1

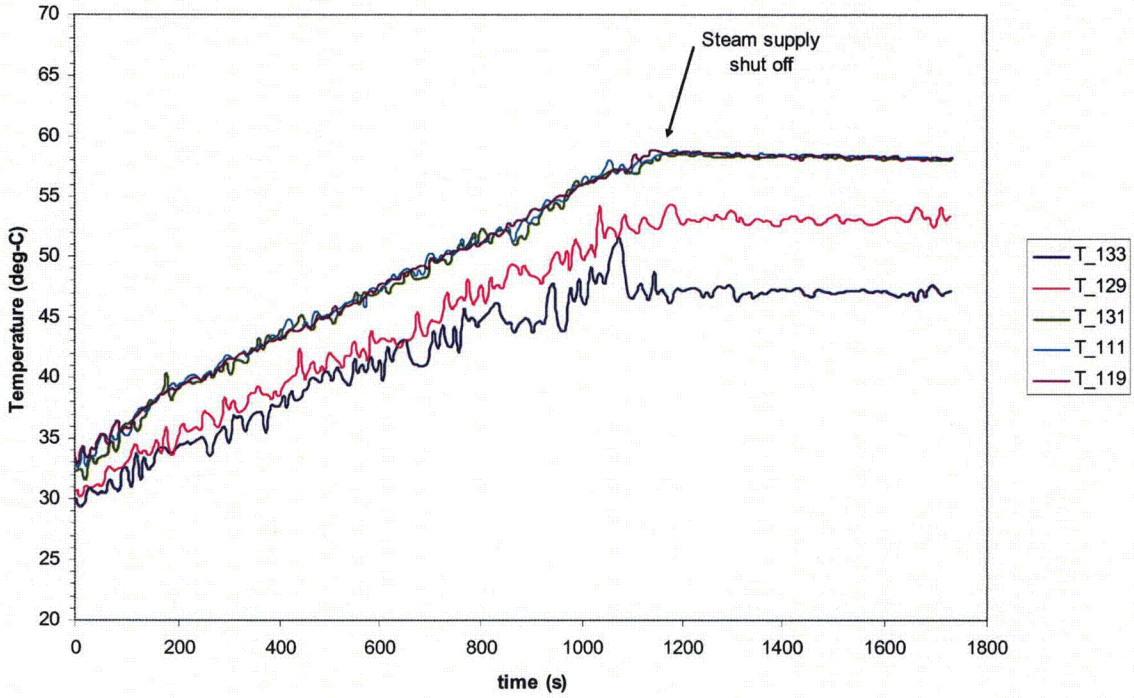

Figure 6.3 Vertical temperature distributions along the pool side centerlines for Case 1

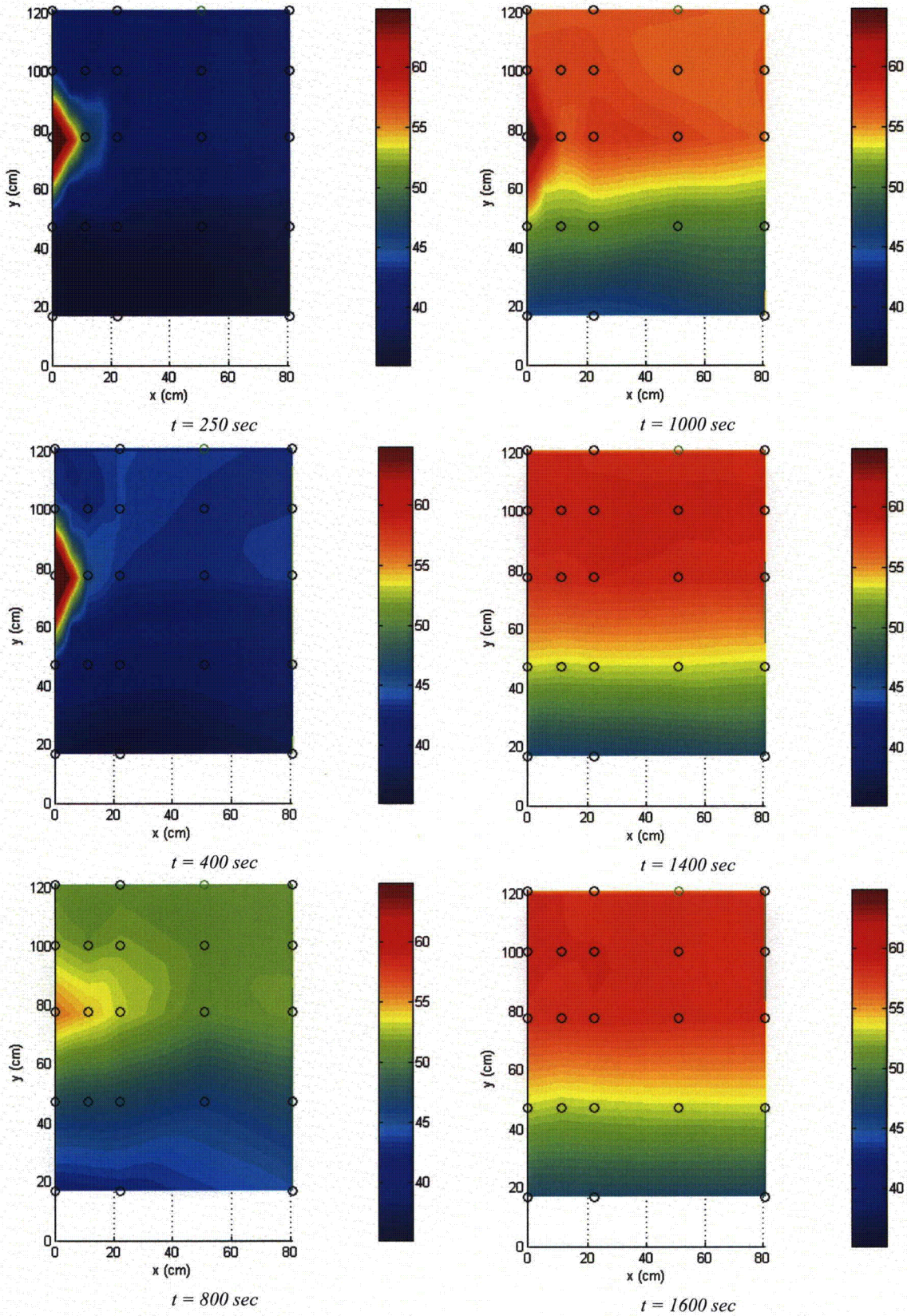

Figure 6.4 Temperature profile development along pool vertical center plane for Case 1

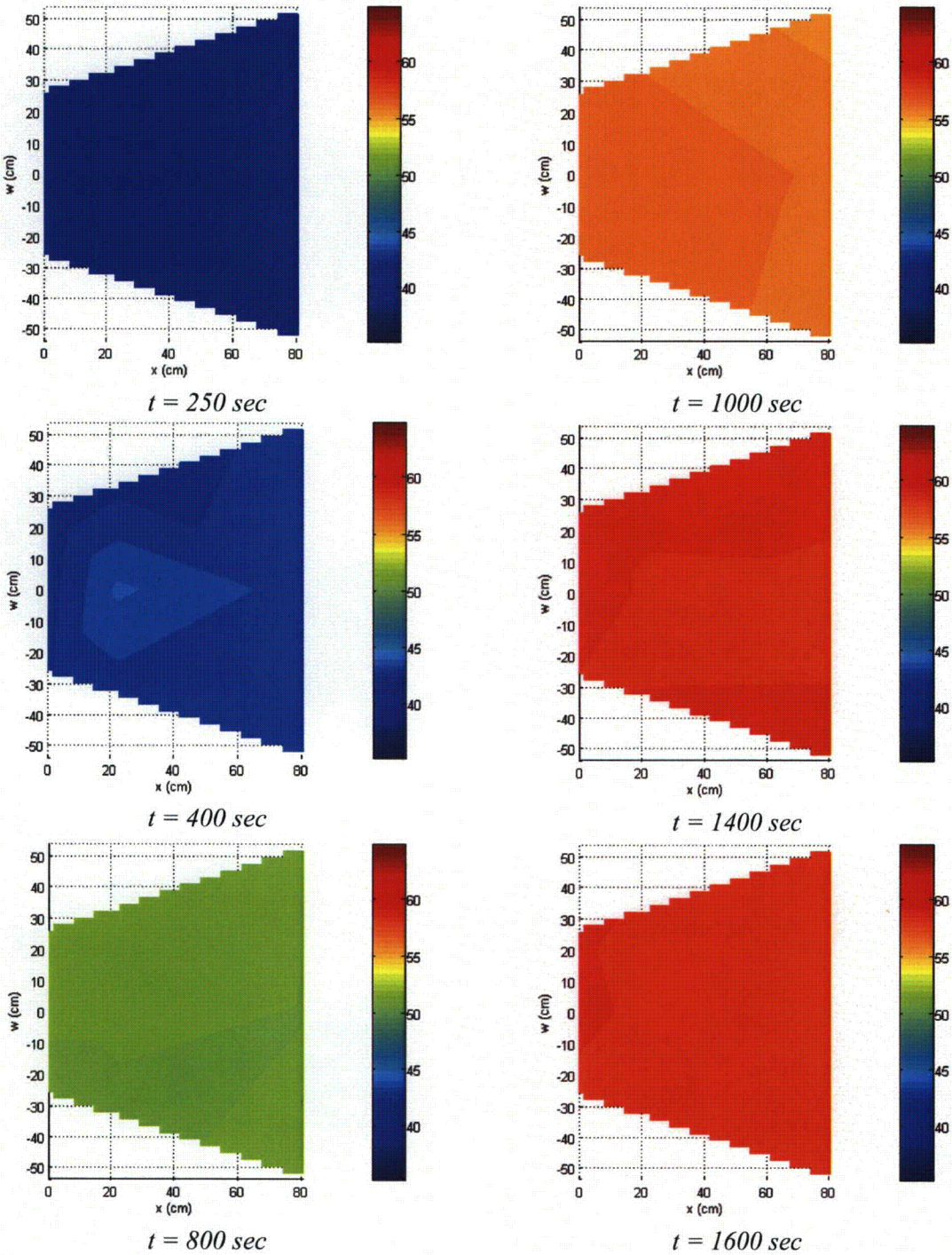

Figure 6.5 Temperature profile development along pool surface for Case 1

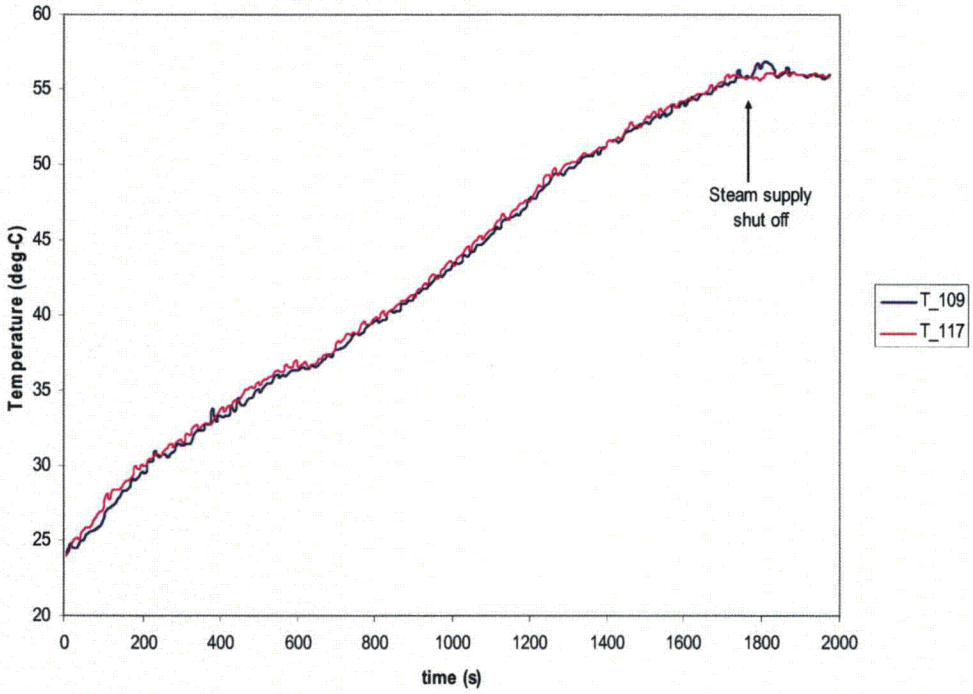

Figure 6.6 Real-time temperature data at the water surface for Case 2

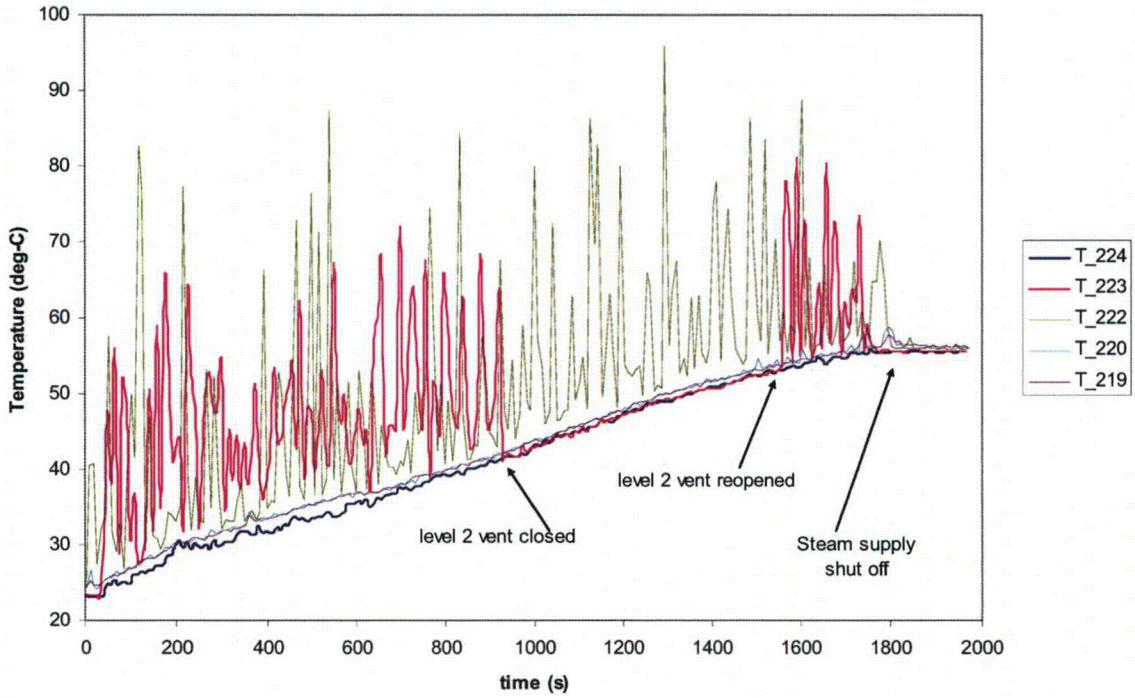

Figure 6.7 Vertical temperature distributions along the vent side centerlines for Case 2

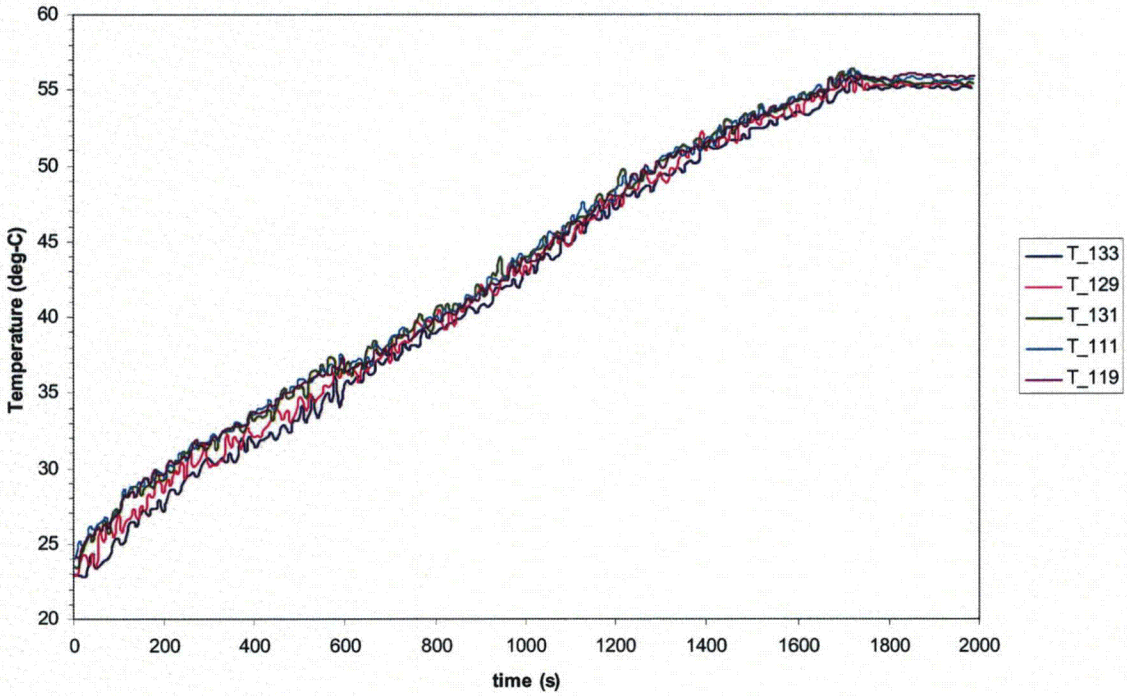

Figure 6.8 Vertical temperature distributions along the pool side centerlines for Case 2

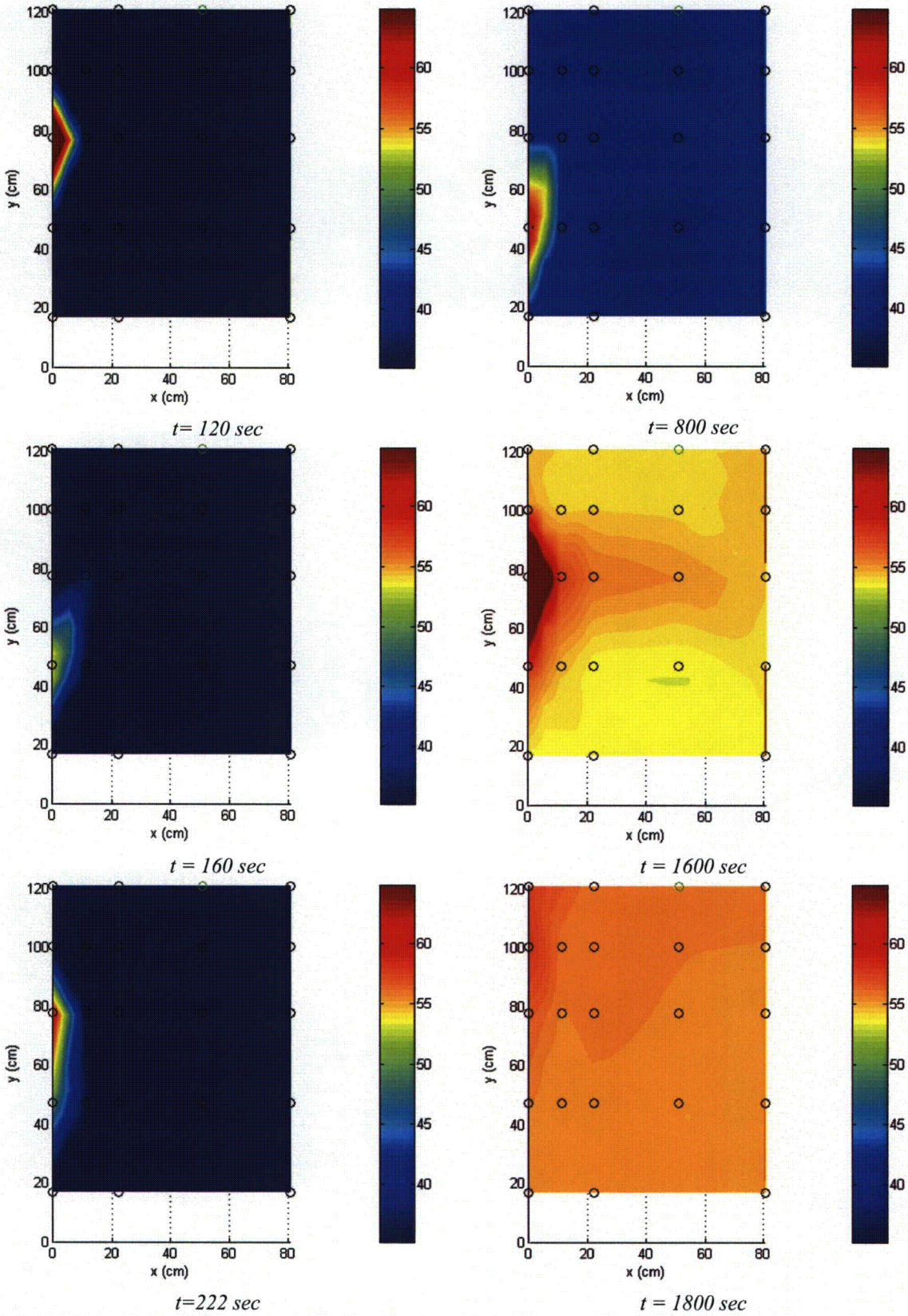

Figure 6.9 Temperature profile development along pool vertical center plane for case 2

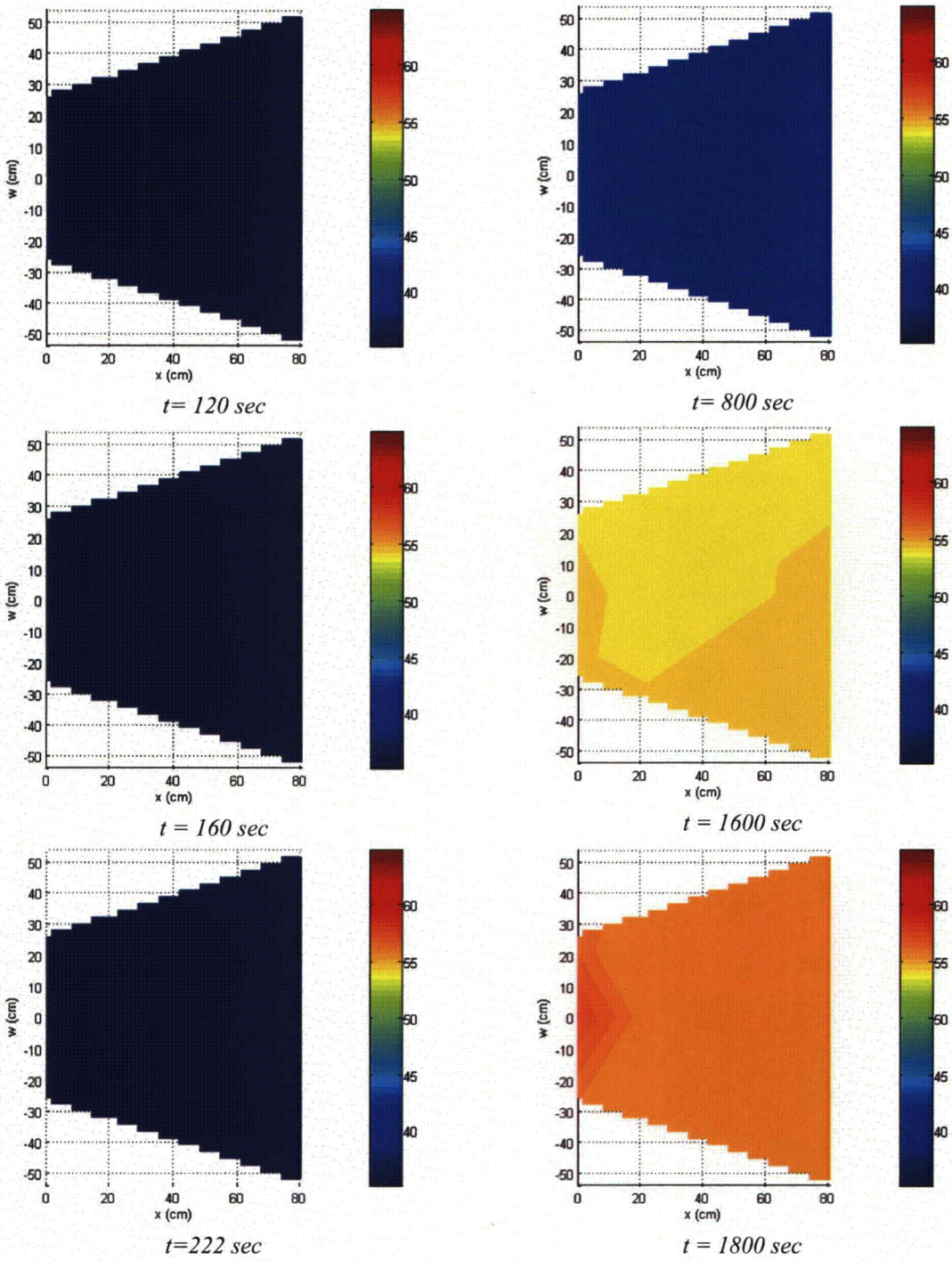

Figure 6.10 Temperature profile development along pool surface for Case 2

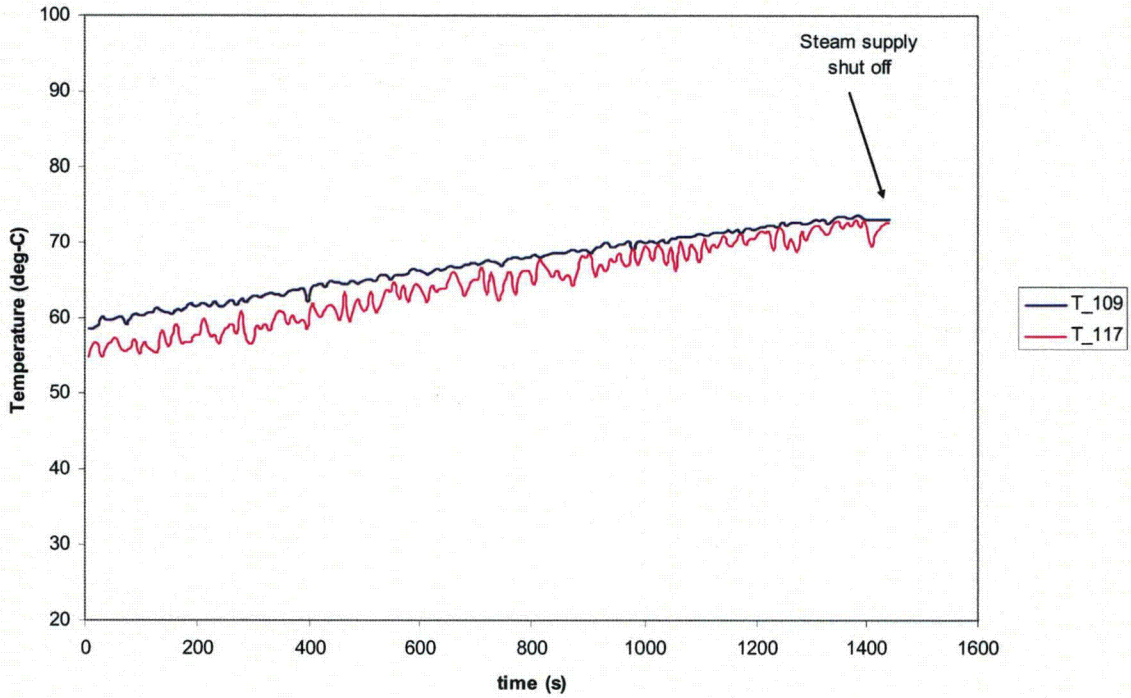

Figure 6.11 Real-time temperature data at the water surface for Case 6

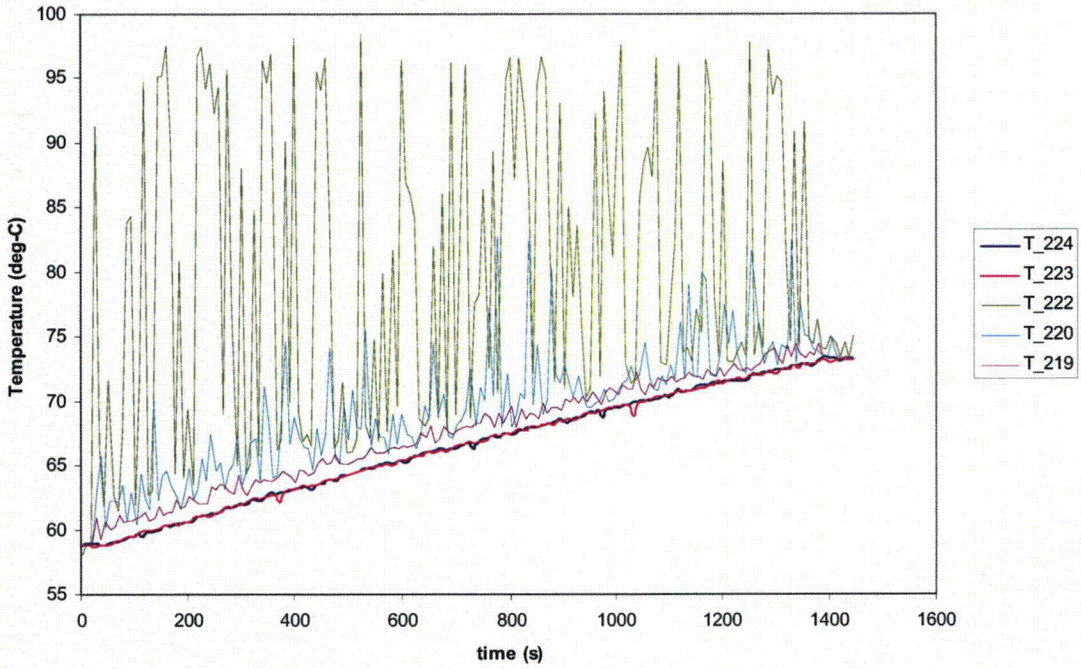

Figure 6.12 Vertical temperature distributions along the vent side centerlines for Case 6

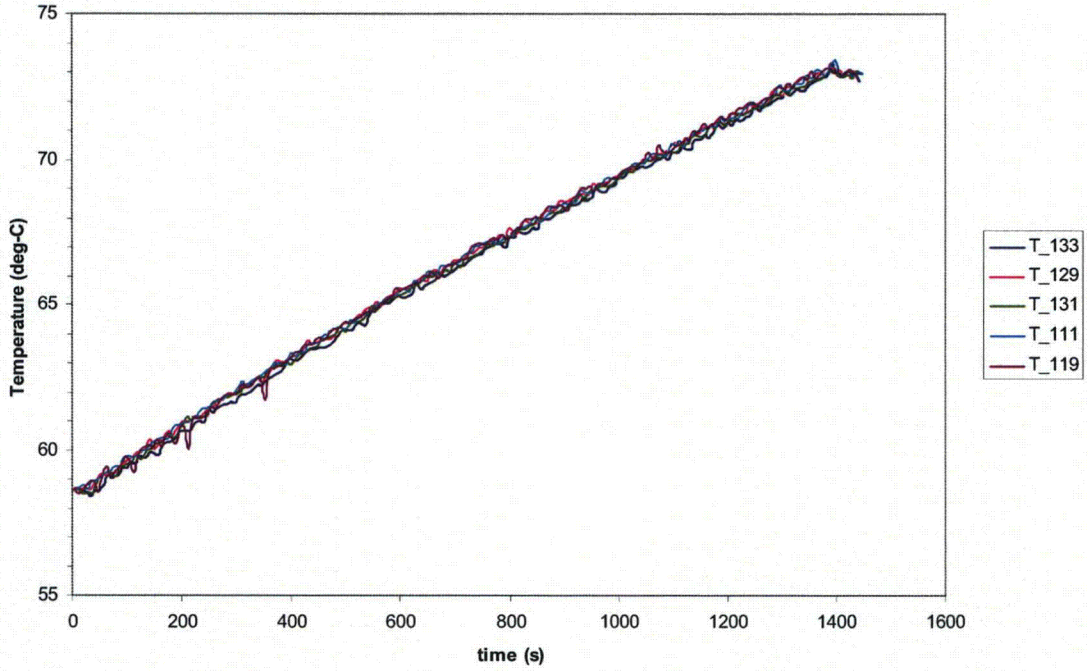

Figure 6.13 Vertical temperature distributions along the pool side centerlines for Case 6

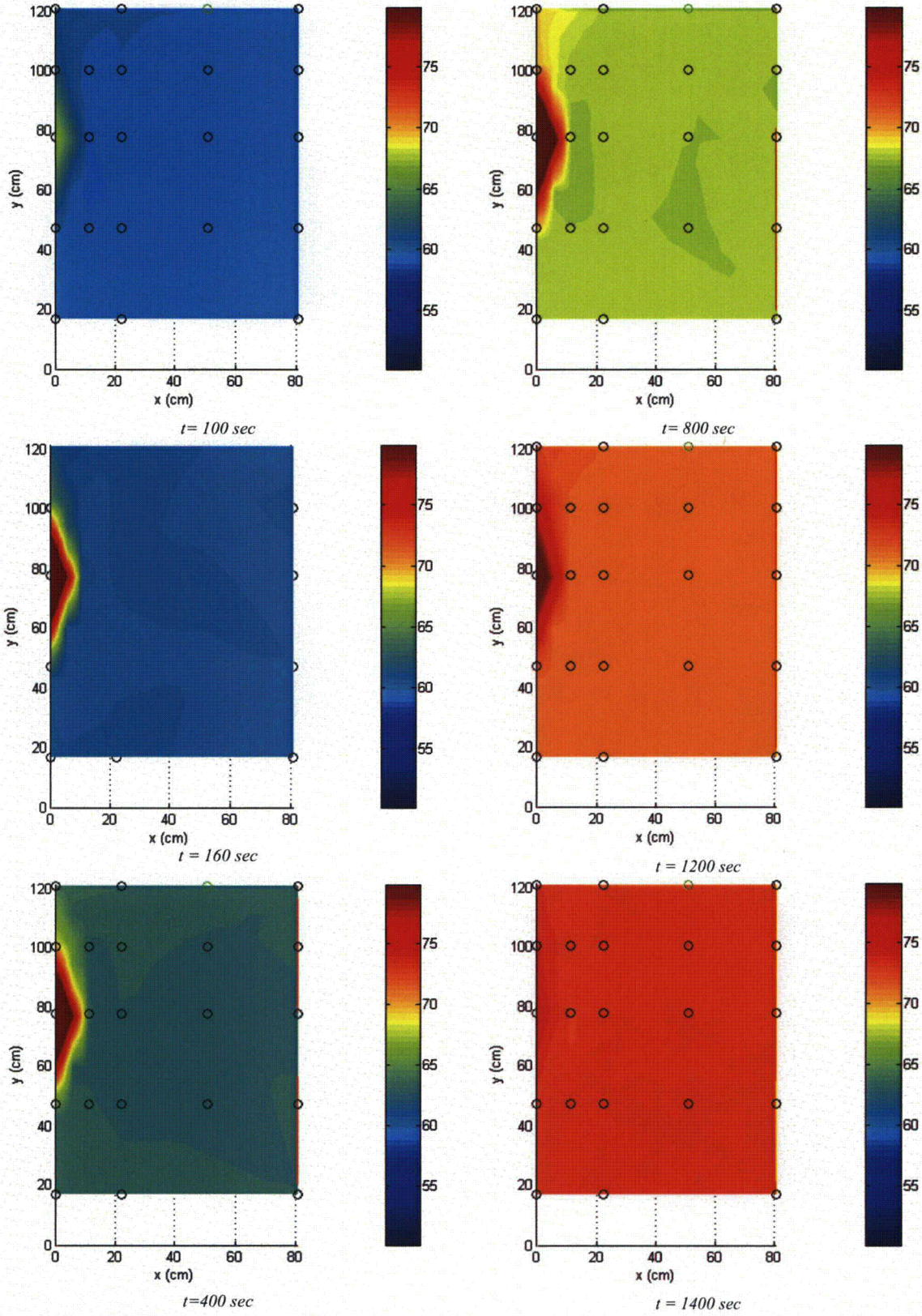

Figure 6.14 Temperature profile development along pool vertical center plane for Case 6

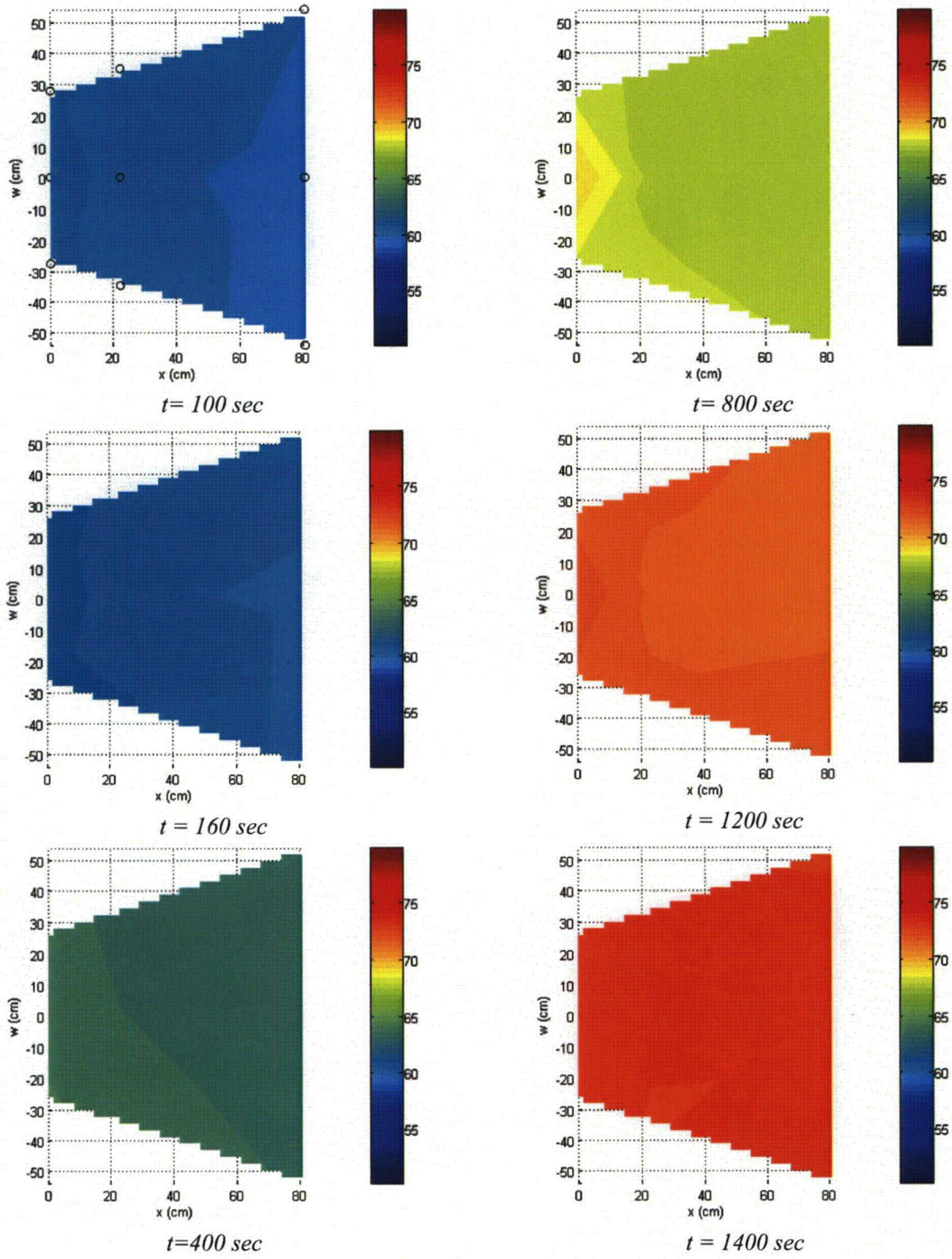

Figure 6.15 Temperature profile development along pool surface for Case 6

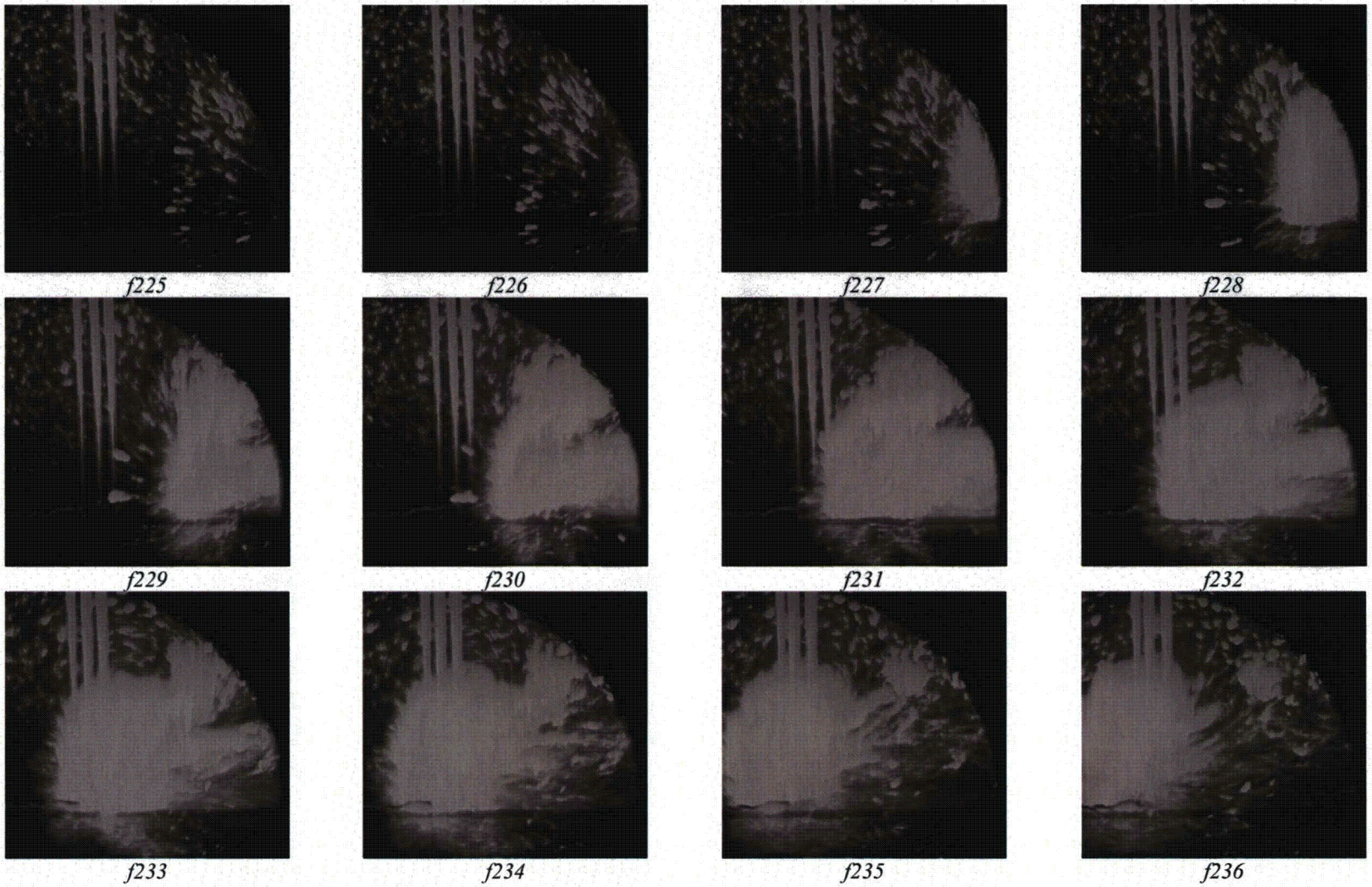

Figure 6.16 High speed photography sequences at the steam flow rate of 50 g/s with 125 fps and view port 12 (1)

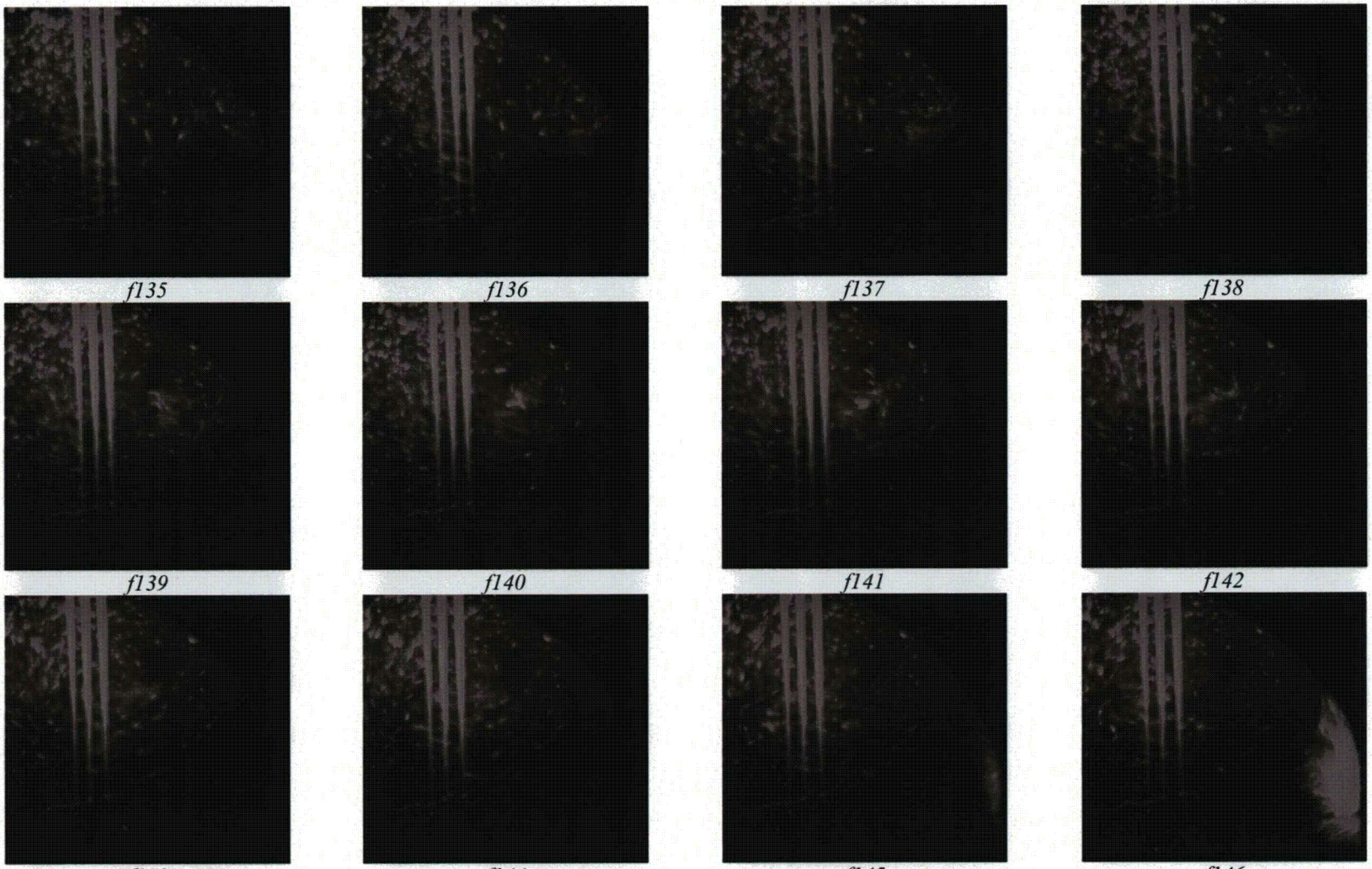

Figure 6.17 High speed photography sequences at the steam flow rate of 50 g/s with 125 fps and view port 12 (2)

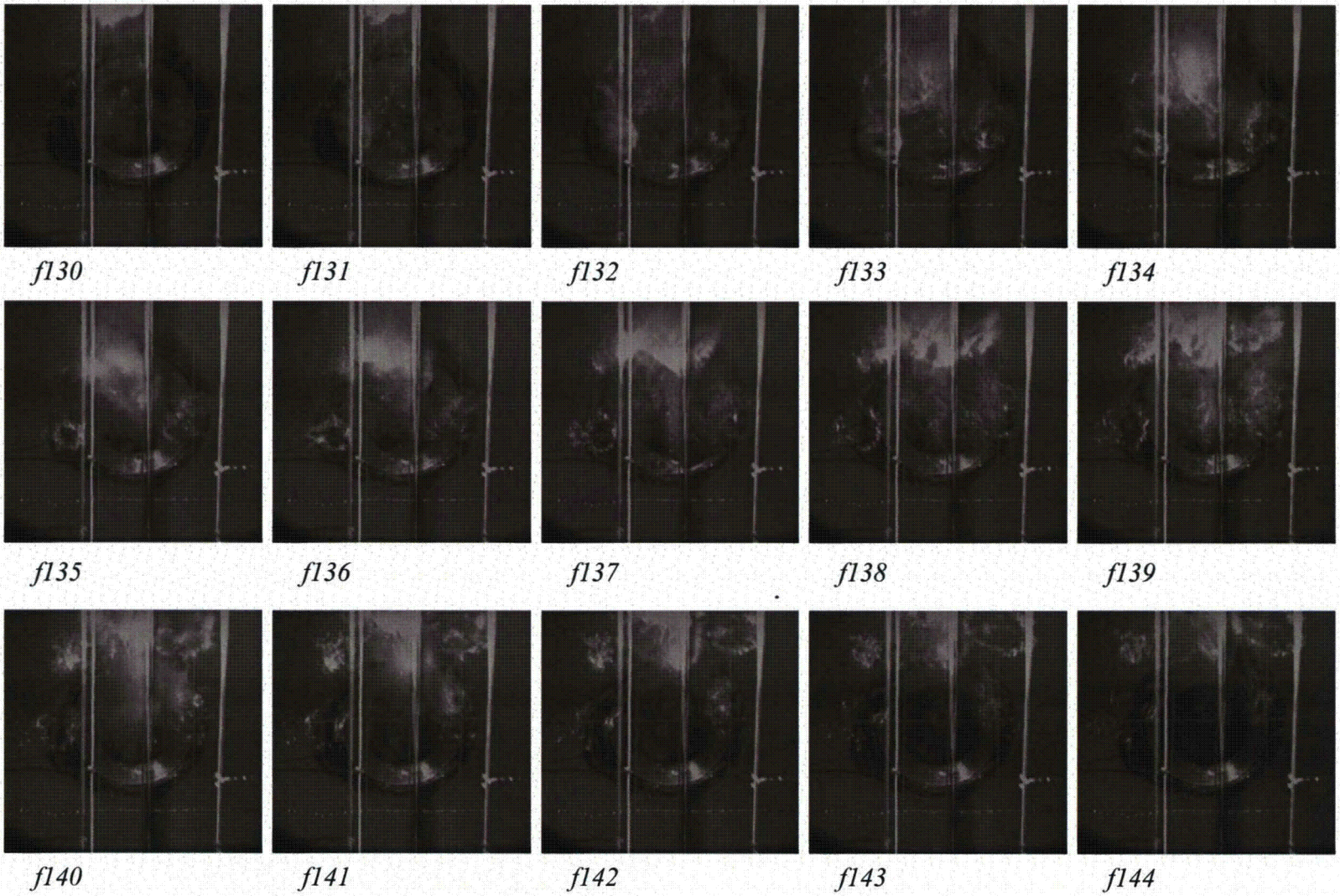

Figure 6.18 High speed photography sequences at the steam flow rate of 20 g/s with 60 fps and view port 8

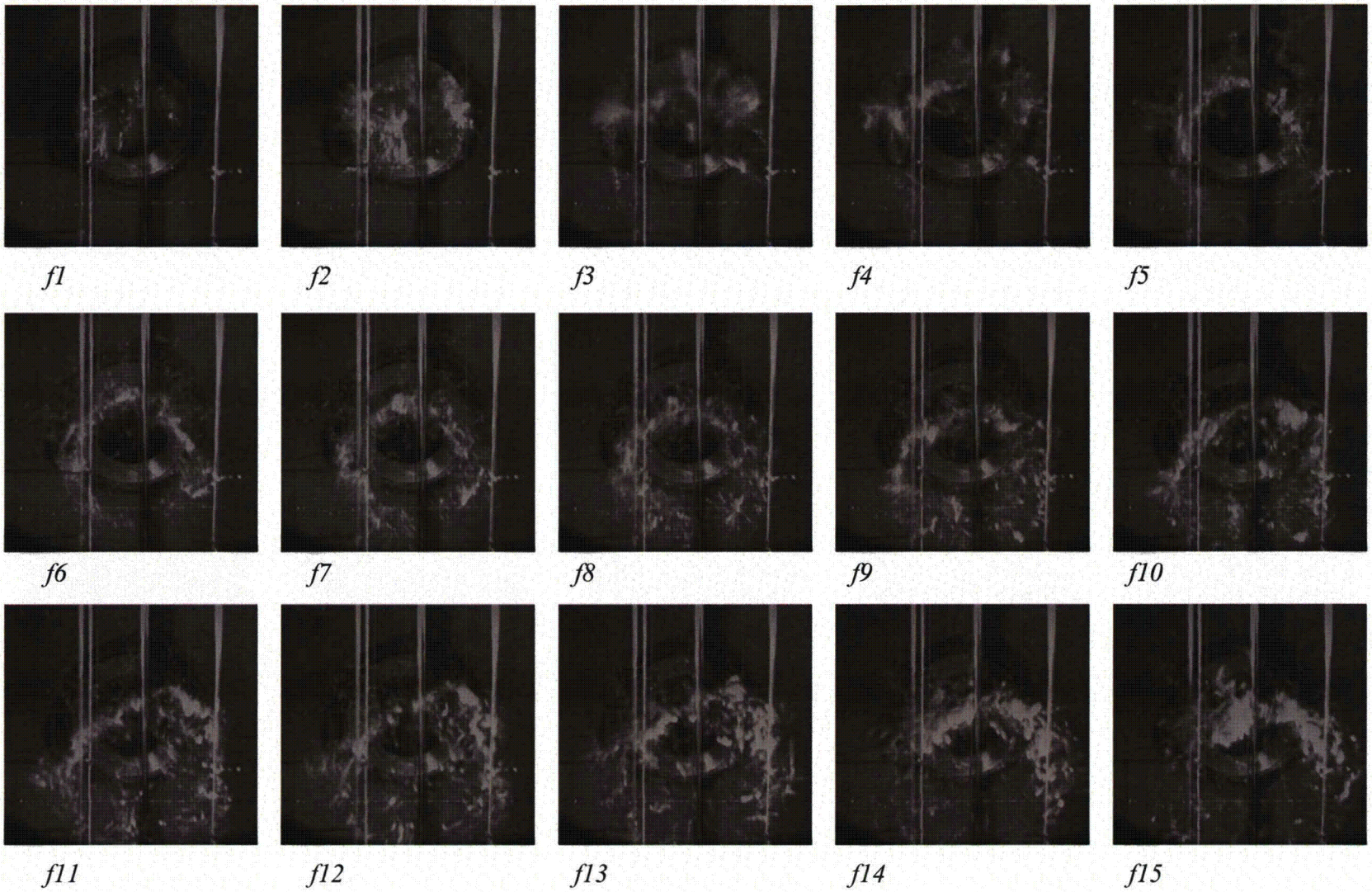

Figure 6.19 High speed photography sequences at the steam flow rate of 50 g/s with 60 fps and view port 8

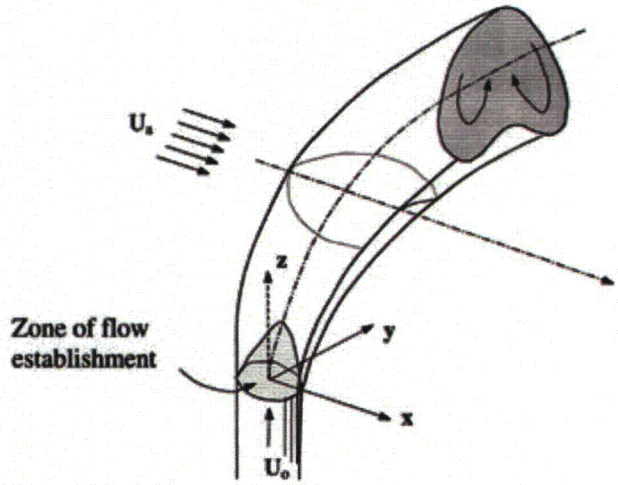

Figure 6.20 Vertical buoyant jet in cross-flow [Lee et al., 2004]

6.3 Reference

Chan, C.K., & Lee, C.K.B. (1982). A regime map for direct contact condensation. *International Journal of Multiphase Flow*, 8(1), 11-20.

Lee, J. H. W., Cheung, V., Lee, A. W. T., Chu, P. C. K., Wong, C. F., & Guo-quian, C. (2004). Mixing of submerged buoyant jets: advected puffs and thermals. Retrieved April 30, 2005, from http://www.hku.hk/civil/envhydraulics/pro_03.htm .

Norman, T. L., Park, H. S., Revankar, S. T., Ishii, M., Vierow, K., & Kelly, J. M. (2005). Steam-air mixture condensation in a subcooled water pool, Facility design and scoping tests. PU/NE-05-19.